UNIVERSITY OF OKLAHOMA

GRADUATE COLLEGE

STABLE ATMOSPHERIC BOUNDARY LAYER TURBULENCE: INSIGHTS
FROM UNCREWED AIRCRAFT SYSTEM OBSERVATIONS AND
LARGE-EDDY SIMULATIONS

A DISSERTATION

SUBMITTED TO THE GRADUATE FACULTY

in partial fulfillment of the requirements for the

Degree of

DOCTOR OF PHILOSOPHY

By

BRIAN ROBERT GREENE
Norman, Oklahoma
2022

STABLE ATMOSPHERIC BOUNDARY LAYER TURBULENCE: INSIGHTS
FROM UNCREWED AIRCRAFT SYSTEM OBSERVATIONS AND
LARGE-EDDY SIMULATIONS

A DISSERTATION APPROVED FOR THE
SCHOOL OF METEOROLOGY

BY THE COMMITTEE CONSISTING OF

Dr. Scott T. Salesky, Chair

Dr. Christopher Fiebrich

Dr. Petra Klein

Dr. S. Marcela Loría-Salazar

Dr. Lara Souza

Dedication

For my dearly departed ΦMA brothers, Dominick Jackson and Christian Arkin. Your time in this world was unfairly short, but your memories will live on in our hearts. May you rest in peace. OAS AAS LLS.

Acknowledgments

I cannot help but feel overwhelmed with emotions for those who have accompanied me to this point in my career. My journey as a scientist has been marked by high peaks and low valleys, with lessons often learned when I least expected. Of these lessons, I can think of none greater than my steadily improving ability to self-identify beyond the grades I earn, the code I write, and the papers I publish. Living through a global pandemic in isolation has also made it abundantly clear the importance of community for our overall well-being. I feel profoundly blessed to have such a strong support system of family, friends, mentors, colleagues, pets, and neighbors: my "village". Words will forever fall short in describing what these people mean to me, but nevertheless I will make a sincere attempt.

First and foremost, I am grateful for my best friend and wife, Dr. Elisa Murillo. Elisa and I met in our first year of grad school at OU in 2016 and got married in 2020 just weeks before the COVID-19 pandemic halted society in the US. Elisa, you are unwaveringly the most genuine, loving, brilliant, passionate, caring, intelligent, thoughtful, and beautiful soul I have ever had the pleasure of knowing, and every day I get to be reminded of how lucky I am to be married to you. You completing your Ph.D. as a young Latina woman is a profound accomplishment and will inspire generations of young scientists. I am so proud of all you have accomplished so far, and I cannot wait to see how you will continue to improve everyone's lives around you in our next chapter together. I love you beyond comprehension.

Living nearly a thousand miles away from my family has been difficult these past years, as they have always been my greatest supporters. I am especially grateful for my parents, Jim and Diane, who nurtured my sense of curiosity with the world from an early age. I largely attribute the foundation of my identities as a son, brother, scientist, musician, and upstanding member of society to their parenting. One day I hope I can do the same for children of my own. I am also enormously proud of the

remarkable adults my younger siblings Emily, Kevin, and Megan have become. It has been such a pleasure to witness their growing emotional intelligence that have led them to follow their passions and find happiness despite the challenges life brings. The days of playing with our Rescue Hero and Polly Pocket toys together may be long passed, but I will always love you as your oldest brother. I am also incredibly blessed to have such a large family full of loving grandparents, aunts, uncles, and cousins. One of my (many, many) favorite parts about marrying Elisa is the new family I have gained. Since the early days of our relationship, Evelyn, Gus, Tracey, Gus, and Kelsie have given me nothing but their unconditional love. Thank you for raising Elisa to be the strong and loving woman she is today and for accepting me as your own. Finally, no conversation about family is complete without also acknowledging our dogs, the late Cece and now Rose. Taking Rose for long walks through the park and cuddling on the couch as ways to decompress have been critical to my success in the final years of my Ph.D. To all my family, from the bottom of my heart, thank you. I love you all so much.

I am immensely grateful for my advisor, Dr. Scott Salesky, for taking over as my Ph.D. committee chair officially in 2021. Since I first met him during his faculty interview with the School of Meteorology, Scott has always made me feel more than a student, but rather his colleague. Between being his TA for three semesters, taking a course of his myself, and ultimately conducting research together, Scott has always made me a priority. I will always be thankful for our countless discussions on pedagogy, academia, career trajectories, work-life balance, life aspirations, and, of course, our dogs! Scott, thank you for being such a great role model and mentor these past few years, and I cannot wait to see how our collaborations grow to new heights as I begin as a postdoctoral research associate with you. I also look forward to continued collaborations within our research group, notably with Claire, Robby, and Leia. I am also extremely thankful for my committee members, Drs. Petra Klein, Chistopher Fiebrich, Marcela Loría-Salazar, and Lara Souza. The logistical side of getting a Ph.D. can be daunting at times, but having such responsive and compassionate committee members has made a world of difference through changing advisors and funding sources. It has been equal parts humbling and exciting to have so much collective expertise and wisdom contributing to my academic journey – thank you all so much.

realize it at the time, but this campaign was a pivotal moment in my educational journey and setting the stage for my dissertation focus on stable atmospheric boundary layer turbulence research. Jochen is largely the reason that Phil became interested in UAS studies years before I arrived at OU, and it is only fitting that he and Stephan would become my co-authors for the first paper of my dissertation. I am continually impressed at your ability to remain on the cutting-edge side of ABL research with UAS, and I look forward to our continued collaborations!

My academic journey leading up to successfully defending my Ph.D. dissertation has largely been influenced by the outstanding leadership and faculty in the School of Meteorology at the University of Oklahoma as well as the Department of Physics and the Department of Atmospheric Sciences at the University of Illinois Urbana-Champaign. I am privileged to have studied under some of the most brilliant minds in the fields of physics and atmospheric sciences at these institutions. I am especially grateful for the enormous impacts that Drs. Jeffrey Frame, Brian Jewett, and Steven Errede have had on my undergraduate studies. Attending graduate school was not even on my radar until crossing paths with these mentors, who were always huge supporters of mine in following my passions. Spending nearly seven years at OU since beginning my M.S. program in 2016, I have also grown a deep appreciation for the staff (front office and IT!) and faculty leadership within the SoM that quite literally keeps the school afloat. Your service to students and to the university can often go without acknowledgement, but please know how profoundly grateful we are for your dedication.

It is hard to overstate the impact the NOAA Ernest F. Hollings Undergraduate Scholarship program had on me. Being able to complete an entire research project from start to end for the first time was transformative in my academic studies and gave me confidence that I could succeed and enjoy pursuing graduate studies in atmospheric sciences. I especially would like to thank my mentors from the NWS Louisville, KY weather forecast office, Theodore Funk, Kevin Deitsch, and Zack Taylor. You guys instantly made me feel like part of the office, and I honestly enjoyed every moment of working together. I also owe thanks to the NOAA Office of Education for selecting and supporting me for this program. It is humbling to be part of the vast network of alumni from this prestigious program.

I would also briefly like to acknowledge the impact that my high school calculus and physics teachers had on my higher education. The AP Calculus and Physics classes

taught by Tim Will and Mark Welter at Prospect High School were some of the first where I was able to succeed while also being engaged with the material, and directly influenced my decision to major in physics at the University of Illinois. It is my hope to someday live in a society where access to such strong primary and secondary education is treated as a given, but for now I recognize my privilege in coming from a school district in the suburbs of Chicago.

Completing a Ph.D. during the global COVID-19 pandemic has been an extreme test of mental and emotional strength. I would like to extend my deepest gratitude for all the essential workers that did not have the luxury of working from home to reduce in-person contact, because these people are the true backbone of our society. I am additionally grateful for the scientists and researchers involved with the development of the COVID-19 vaccines that enabled safer in-person gatherings after a year of isolation. With all the time spent at home with societal dread increasing on all fronts, a lot of us took the chance to look inwards and reflect. I would like to acknowledge the role that mental health professionals have played in my journey, as I believe I am a better husband, son, brother, and scientist from my investment in mental health.

As I mentioned at the beginning of these acknowledgements, this is by no means a comprehensive list of the people who have made significant impacts on my time as a graduate student at OU. Please know that even if you are not explicitly listed by name here, you hold a special place in my heart. This is especially true for my chosen family of close friends that I could not imagine life without. Thank you for always being there with me to enjoy the highs of life, but also for supporting me at my lows. This has been the most exciting and fulfilling chapter of my life, and I certainly could not have gone it alone. Thank you all so much.

Table of Contents

List Of Tables

List Of Figures

Abstract

The physical processes governing stable atmospheric boundary layer (SBL) dynamics have significant societal impacts ranging from pollution dispersion and wind energy production to polar sea ice loss. For decades, SBL turbulence has proven challenging to measure, parameterize, simulate, and interpret for a variety of reasons. For example, turbulence intensity in the SBL is often orders of magnitude smaller than in the convective boundary layer as thermal stratification suppresses vertical motions. As atmospheric stability increases, turbulence can also become intermittent in space and time, resulting in poor convergence of temporally-averaged turbulence statistics. Characteristic turbulent motions within the SBL can also be considerably smaller than the grid spacings employed by operational numerical weather prediction (NWP) models. These NWP models therefore need to parameterize turbulent energy exchange within the SBL, which can result in significant errors in near-surface temperature and wind speed forecasts due to the imperfect nature of parameterization schemes. It has been shown that improvements in SBL forecasting skill have been hindered by a relative lack in knowledge of fundamental SBL processes, which in turn is partially due to a dearth in routine and spatially dense thermodynamic and kinematic observations within the SBL. To address this so-called data gap, uncrewed aircraft systems (UAS) are proving the ability to reliably sample the atmospheric boundary layer (ABL), offering a new perspective for understanding the SBL. Moreover, continual computational advances have enabled the use of large-eddy simulations (LES) to simulate the atmosphere at ever-smaller scales. This dissertation therefore seeks to synergize UAS observations and large-eddy simulations to explore the underlying processes governing SBL dynamics.

In the first component of this dissertation, we explore the potential of a new method for the estimation of profiles of turbulence statistics in the SBL. By applying gradient-based scaling to multicopter UAS profiles of temperature and wind, sampled

over sea ice during the 2018 Innovative Strategies for Observations in the Arctic Atmospheric Boundary Layer (ISOBAR18) field campaign, turbulence profiles can be derived. We first validate this method by scaling turbulence observations from three levels on a 10-m mast with the corresponding scaling parameters, and comparing the resulting non-dimensional parameters to the semi-empirical similarity functions proposed for this scaling framework. The scaled data of turbulent fluxes and variances from the three levels collapse to their corresponding similarity functions. After the successful validation, we estimate turbulence statistics from UAS profiles by computing profiles of the gradient Richardson number to which we then apply the similarity functions. These UAS profiles are processed from raw time series data by applying low-pass filters, time-response corrections, altitude corrections, and temporal averaging across successive flights. We present three case studies covering a broad range of SBL conditions to demonstrate the validity of this approach. Comparisons against turbulence statistics from the 10-m mast and a sodar indicate the broad agreement and physically meaningful results of this method. Successful implementation of this method thus offers a powerful diagnostic tool that requires only a multicopter UAS with a simple thermodynamic sensor payload. This ability to estimate vertical profiles of turbulent parameters that were otherwise unobtainable with traditional ground-based observations can be invaluable, e.g., for NWP verification studies within the SBL.

As UAS continue to be recognized as a robust observational platform, it is becoming increasingly important to establish a baseline framework towards understanding the extent to which vertical profiles from UAS can represent larger-scale SBL flows. This representativeness can be quantified by evaluating the magnitude of random errors for a given observation, which arise due to averaging a signal across an insufficient amount of independent samples for a statistical quantity to converge towards its true underlying ensemble value. Moreover, the LES technique can be a powerful tool for simulating SBL turbulence in space and time while varying thermal stratification to contextualize observations by UASs. The second component of this dissertation therefore seeks to quantify the representativeness of observations from UAS profiles and eddy-covariance observations within the SBL by performing a random error analysis using a suite of six large eddy simulations for a wide range of stabilities. For each experiment, we estimate relative random errors using the relaxed filtering method of Dias et al. (Boundary-Layer Meteorology, 2018, Vol. 168, 387–416) for first- and second-order

moments as functions of height and averaging time. We show that the random errors can be of the same order of magnitude as other errors due to e.g. instrument bias and dynamic response, especially close to the surface. For these reasons, we recommend coupling UAS observations with other ground based instruments as well as dynamically adjusting the UAS vertical ascent rate to account for how errors change with height and stability.

In the first component of this dissertation, we consider only observations by UAS in the Arctic SBL, and in the second component we further explore the representativeness of UAS observations within idealized SBLs with LES. To conclude this dissertation, in the third component we employ only a series of eight large-eddy simulations to investigate fundamental processes within stably-stratified wall-bounded turbulent flows from the perspective of coherent structures. To date, a growing body of literature has documented the existence and impacts of so-called large- and very-large-scale motions within wall-bounded turbulent flows under neutral and convective thermal stratification. Large- and very-large-scale motions have been attributed to modulating turbulence intensity near the wall, and properly characterizing their contributions to ABL turbulence may lead to improvements in NWP forecast skill. In the context of the SBL, however, the examination of such coherent structures has garnered relatively little attention. Stable stratification limits vertical transport and turbulent mixing within flows, which makes it unclear whether previous findings on coherent structures under unstable and neutral stratification are applicable to the SBL. Moreover, mesoscale processes can obscure the underlying physics of stably-stratified flows when collecting observations in the SBL. In this third component, we investigate the existence and characteristics of coherent structures within the SBL with a wide range of statistical and spectral analyses. A quadrant analysis of turbulent transport efficiencies (the ratio of net fluxes to their respective downgradient components) demonstrates dependencies on both stability and height above ground, which may be related to morphological differences in the coherent structures under increasing stability. Physical mechanisms responsible for these differences are explored through analyses of spectrograms, linear coherence spectra, amplitude modulation coefficients, and conditional sampling for a variety of first- and second-order turbulent moments. Results indicate the presence of coherent structures at near-neutral stability that diminish with increasing stable

stratification. Stable stratification was found to suppress large eddies, thereby limiting any inner-outer scale interactions.

Preface

The introduction of this dissertation along with two of the chapters are based on and reproduced from published peer-reviewed journal articles. Permission has been obtained from the publishers where necessary.

Chapter 2

Greene, B. R., S. T. Kral, P. B. Chilson, and J. Reuder, 2022: Gradient-Based Turbulence Estimates from Multicopter Profiles in the Arctic Stable Boundary Layer. *Boundary-Layer Meteorol*, **183 (3)**, 321–353, doi:10.1007/s10546-022-00693-x. Used with permission from Springer Nature.

Chapter 3

Greene, B. R., and S. T. Salesky, 2022: Random Errors in the Stable Boundary Layer: Implications for Modern Observational Techniques. *J. Atmos. Sci.*, doi:10.1175/JAS-D-22-0096.1. ©American Meteorological Society. Used with permission. This preliminary version has been accepted for publication in the Journal of the Atmospheric Sciences and may be fully cited. The final typeset copyedited article will replace the EOR when it is published.

Chapter 1

Introduction

1.1 The Atmospheric Boundary Layer

The atmospheric boundary layer (ABL) is the region of the Earth's atmosphere which directly interfaces with its surface. Yet for such a simple definition, the dynamics within are anything but simple. Understanding the constant exchange of momentum, heat, moisture, aerosols, and other chemical species from the surface and within the atmosphere via turbulent transport has challenged scientists for centuries. Weather systems, including thunderstorms, tornadoes, hurricanes, and winter storms, largely draw their energy and moisture from the ABL, and have been shown to transport mass vertically through the troposphere and into the stratosphere. It is also the region of the atmosphere where the entirety of humanity resides; the air we breathe, the pollution we emit, and the weather we experience all take place within the ABL.

The structure of the ABL is largely driven by the varying incoming solar radiation throughout the diurnal cycle (Stull, 1988). As depicted in Figure 1.1a, the ABL undergoes transitions around sunrise and sunset. In the afternoon, incoming solar radiation is at its greatest and causes the surface to heat rapidly. This heat is transferred into the overlying atmospheric surface layer that is characterized by vertical fluxes that are constant with height. The middle of the convective boundary layer (CBL, Figure 1.1b) is marked by a well-mixed layer in which potential temperature, water vapor mixing
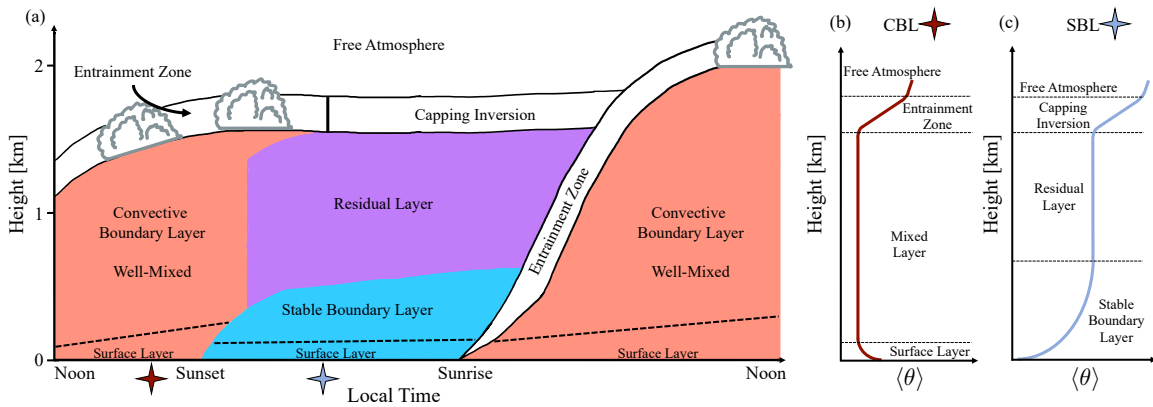
Figure 1.1: Conceptual model of the diurnal evolution of the ABL (after Stull, 1988; Markowski and Richardson, 2011). (a) Time-height cross-section over a full 24-hr period identifying the key layers, and vertical profiles of mean potential temperature $\langle\theta\rangle$ for (b) the convective boundary layer and (c) the stable boundary layer. Note that (b) and (c) are marked by red and blue stars in (a) for their corresponding times.

ratio, and wind speed remain roughly constant with height due to constant mixing by turbulent eddies. These eddies can range in size from the depth of the CBL (~ 1–3 km) down to where molecular viscosity becomes relevant and turbulent kinetic energy undergoes viscous dissipation (~ 1 mm).

Continuing with the diurnal cycle presented in Figure 1.1a, as the sun sets in the evening, the source of downwelling solar radiation is reduced to zero. Throughout the night, the surface continues to cool via longwave radiation, resulting in a negative net energy budget if no large-scale weather patterns are present. The relatively small specific heat capacity of the Earth's surface enables it to cool more rapidly than the air directly above, which results in a vertical profile where potential temperature increases with height (Figure 1.1c) topped by the residual CBL from the previous afternoon. In polar regions of the Earth that go without sunlight for months at a time, this surface-based inversion can extend for hundreds of meters in the vertical (e.g., Curry, 1983). A proper understanding of SBL dynamics has far-reaching implications from pollution dispersion and wind energy production to how the effects of climate change are

disproportionately strong at high latitudes, a phenomenon known as polar amplification (Taylor et al., 2013; Pithan and Mauritsen, 2014; Beer et al., 2020). Polar amplification is in part related to a nonlinear combination of feedback mechanisms including, for example, the surface albedo feedback which can be summarized as follows: decreasing sea ice extent reduces the surface albedo of the polar regions which enables greater quantities of solar radiation to be absorbed by the oceans, thereby increasing their temperature and accelerating the rate of sea ice melt (Taylor et al., 2013).

1.1.1   The Stable Atmospheric Boundary Layer

It has been shown that difficulties in the simulation of the stable boundary layer (SBL) by numerical weather prediction (NWP) models can be attributed to the lack of fundamental knowledge of how to represent turbulence in the SBL (e.g., Steeneveld et al., 2008; Sandu et al., 2013; Holtslag et al., 2013). Stably-stratified flows are subject to considerable variability both in time and space, with turbulent fluctuations that are often intermittent and small in magnitude (Coulter and Doran, 2002; van de Wiel et al., 2003; Klipp and Mahrt, 2004; Steeneveld, 2014), making it difficult to parameterize energy and momentum transfer across the relevant stability range. With such weak turbulent motions, SBL flows are sensitive to a wide variety of feedback mechanisms such as soil heat fluxes, cloud cover, radiative flux divergence, and the formation of a low-level jet (LLJ; see Figure 1.2). These processes can play significant roles in determining the predominant sources of turbulence generation within the SBL (Mahrt, 1999; Mahrt et al., 2012; Mahrt and Acevedo, 2022). A better understanding of the SBL is in particular hampered by the lack of available vertical profile observations of mean and turbulence variables at an appropriate vertical and temporal resolution.

Numerous weather models rely on turbulence parameterizations and boundary conditions predicted by Monin–Obukhov similarity theory (MOST, Monin and Obukhov,

1954), which non-dimensionalizes vertical gradients of wind, temperature, and humidity in the atmospheric surface layer (ASL) by scaling with estimates of their respective surface fluxes. The MOST scaling relationships and resulting profiles of momentum, heat, and moisture therefore have the advantage of considerably reducing the computational expense of forecasting these parameters. However, MOST is theoretically only valid for statistically stationary, horizontally homogeneous flow fields at high Reynolds number and with zero mean subsidence. Because the atmosphere rarely satisfies these conditions, there is substantial room for improvement in parameterizing atmospheric boundary-layer (ABL) processes, especially for the SBL. Moreover, empirical studies evaluating MOST commonly identify an inability to differentiate between near-neutral and strongly stable regimes (Foken, 2006; Sorbjan, 2010; Sorbjan and Grachev, 2010; Grachev et al., 2013). Studies using large datasets collected in the SBL have shown success with a turbulence scaling framework based on local vertical gradients of temperature and wind (Sorbjan, 2010; Sorbjan and Grachev, 2010; Sorbjan, 2017). This method is formally equivalent to MOST but utilizes scaling properties based upon well-defined vertical gradients. These gradient-based scales are advantageous over those in traditional MOST, which are second-order turbulent moments that are difficult to measure due to the weak and possibly intermittent nature of SBL turbulence, and they are also sensitive to conditions of stationarity and larger-scale forcings. Gradient-based scaling as a function of Richardson number, Ri, also has the advantage over MOST since it does not suffer from self-correlation (artificially inflated/deflated agreement between theory and observations of scaled turbulent quantities arising when the same scale appears on both sides of a statistical relationship Baas et al., 2006; Sorbjan, 2010), which mitigates considerable uncertainty in the shape of the similarity functions. This therefore leads to an application of gradient-based scaling as eluded to by Sorbjan

and Grachev (2010): when the similarity functions between local gradients and turbulent parameters are known, the problem can be reversed to estimate the turbulent parameters only by measuring the vertical gradients of wind speed and temperature.

Recent advances in computational power and NWP model efficiency have enabled considerable strides in operational forecasting abilities. While these models tend to perform well in neutrally and unstably stratified flows, they struggle to properly represent SBLs (Sandu et al., 2013; Holtslag et al., 2013; Vignon et al., 2018). These model deficiencies are typically related to an overestimation of turbulent mixing rates (albeit intentionally to gain forecast skill at large scales) and therefore increased ABL heights, which then manifest as errors in surface temperature and wind forecasts (Holtslag et al., 2013) and a general warm bias in the SBL (Lüpkes et al., 2010; Atlaskin and Vihma, 2012).
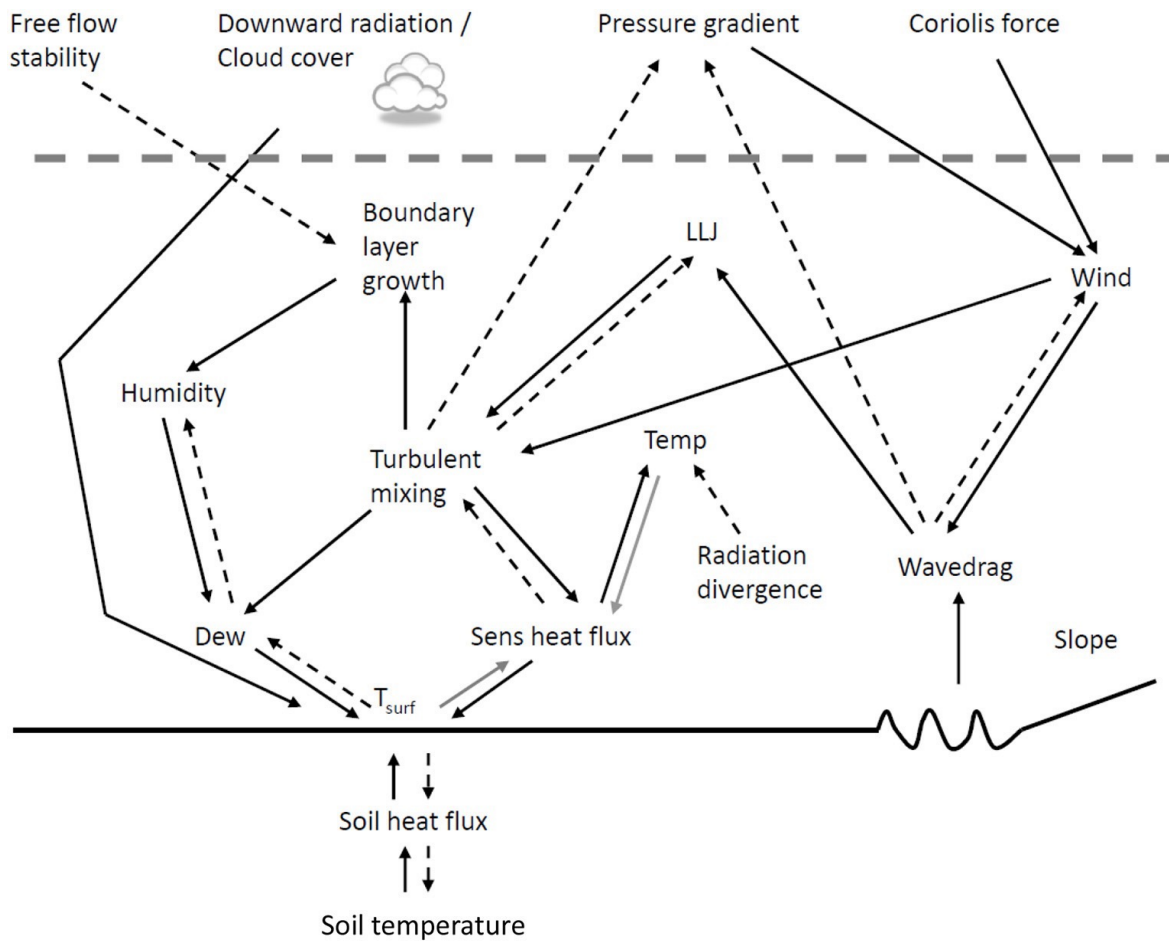
Figure 1.2: Overview of the physical processes governing the SBL from Steeneveld (2014), their Figure 2. Solid lines denote positive feedbacks, dashed are negative feedback mechanisms, and grey lines can be either depending on the state of the ABL.

1.2 Uncrewed Aircraft Systems

In response to the recent rapid technological advances in open source autopilot hardware and miniaturization of thermodynamic sensors, several groups around the world have embraced the utility of uncrewed aircraft system (UAS) technology (also known as unoccupied aircraft systems or remotely piloted aircraft; for a discussion on terminology, see Joyce et al., 2021) for atmospheric research (e.g., Reuder et al., 2009, 2012; Houston et al., 2012; Wildmann et al., 2014; de Boer et al., 2016; Wrenger and Cuxart, 2017; Lampert et al., 2020; Segales et al., 2020; Pinto et al., 2021; Al-Ghussain and Bailey, 2022). Numerous national reports have described the need for significantly more frequent and spatially dense observations within the ABL (National Academies of Sciences, Engineering, and Medicine, 2007, 2018a,b; National Research Council, 2009; Hoff and Hardesty, 2012), and measurements collected by UASs are showing promise in bridging this so-called data gap (e.g., Greene, 2018; Chilson et al., 2019; McFarquhar et al., 2020; Pinto et al., 2021; Houston et al., 2021; Bell, 2021). A common application of UAS technology in atmospheric sciences is to collect thermodynamic and kinematic observations as a function of altitude, similar to a traditional radiosonde and with comparable accuracy (Bell et al., 2020) while also offering significantly improved vertical resolution, mobility, and experimental control (Jiménez et al., 2016; Cuxart et al., 2019; Chilson et al., 2019; Bell et al., 2020).

Several recent field campaigns have incorporated UASs, such as the Innovative Strategies for Observations in the Arctic Atmospheric Boundary Layer campaign (ISO-BAR; Kral et al., 2018, 2021; Greene et al., 2022), the Lower Atmospheric Profiling Studies at Elevation–A Remotely Piloted Aircraft Team Experiment (LAPSE-RATE; de Boer et al., 2019, 2020), and the Tracking Aerosol Convection Interactions ExpeRiment (TRACER; Jensen, 2019). The UASs featured in these campaigns fall into one of

two main categories: fixed- and rotary-wing. Fixed-wing UASs are capable of carrying heavier payloads with longer flight endurances as compared to rotary-wing UASs, and are therefore better suited for carrying sensor packages containing turbulence-resolving instruments (e.g., Wildmann et al., 2014; Rautenberg et al., 2019; Alaoui-Sosse et al., 2022; de Boer et al., 2022) or bulky chemical species and aerosol instruments (e.g., Schuyler and Guzman, 2017; Krautwurst et al., 2021). Rotary-wing UASs include both commercial off-the-shelf aircraft outfitted with sensors (e.g., Islam et al., 2021) as well as custom-built multicopters such as the University of Oklahoma CopterSonde (Segales et al., 2020; Pillar-Little et al., 2021). Rotary-wing UASs offer advantages over fixed-wing UASs in that they are more easily controlled and operated, offer a quasi-Eulerian perspective of atmospheric sampling, can take off and land vertically, and are capable of hovering and slow vertical profiling. Rotary-wing UAS observations must also consider the effects of propeller downwash in a thermally stratified environment (Houston and Keeler, 2020). As such, these rotary-wing UASs are typically best suited for collecting observations in vertical profiles, where they offer high vertical and temporal resolution (e.g., one profile every 15 min at 3 m vertical resolution) for analysis of vertical gradients (e.g., Lappin et al., 2022; Greene et al., 2022). With an advanced level of automation, it may one day be possible to operate a spatially-distributed network of rotary-wing UASs for routine and unattended profiling of the ABL (Chilson et al., 2019; Jacobs et al., 2020).

However, it is still a challenge to collect the high-frequency (i.e., $\gg 1$ Hz) observations needed for turbulence estimates using UASs on a consistent basis. While recent research in autopilot control theory shows the potential for large-bandwidth environmental wind measurements (González-Rocha et al., 2019, 2020), which could potentially resolve turbulent stresses, many commercial off-the-shelf platforms do not

enable this level of precision. A handful of research groups have developed specialized fixed-wing UASs with sophisticated turbulence sensor packages including hot- and cold-wire thermometers and anemometers plus multi-hole pitot tube probes that can explicitly resolve turbulence (e.g., Wildmann et al., 2014; de Boer et al., 2016; Rautenberg et al., 2019; Al-Ghussain and Bailey, 2022). Such systems offer great potential for ABL research, in particular due to their horizontal sampling capabilities. However, these instruments and aircraft are expensive, delicate, and difficult to operate on a consistent basis. Stable boundary-layer conditions (e.g., very weak and intermittent turbulence, strong vertical gradients, and often cold conditions) are particularly challenging. Obtaining representative turbulence observations from these platforms also involves systemic challenges due to measured parameters (e.g., air speed, UAS speed, and attitude angles) being an order of magnitude larger than the turbulent fluctuations.

1.2.1 Field Campaigns at High Latitudes

The polar regions of the globe are an ideal location to study the SBL since they are characterized by prolonged periods of stability and are not limited to overnight diurnal patterns as in mid-latitudes. Additionally, the presence of sea ice at high latitudes produces horizontally homogeneous flow across large distances. These regions, however, pose logistical challenges for personnel and equipment due to their remote access and extreme conditions. There have been a handful of sea- and land-based efforts to study the SBL in the Arctic and Antarctic since the 1990s, including the Surface Heat Budget of the Arctic Ocean (SHEBA) program in the Beaufort Sea (1997–1998; Persson et al., 2002; Grachev et al., 2005); at the Summit Station in central Greenland (Miller et al., 2013); and most recently, the Multidisciplinary drifting Observatory for the Study of Arctic Climate (MOSAiC) expedition (Shupe et al., 2018; Wake, 2019). Field campaigns targeting the SBL commonly employ masts equipped with

eddy-covariance instruments, radiosondes, tethersondes, and remote sensing such as sodar, lidar, Fourier transform spectrometers, and microwave radiometers. Although these technologies are relatively mature, they are not without drawbacks that hinder the ability to continually observe the SBL. For example, it is difficult to employ flexible deployment strategies with fixed masts and heavy ground-based remote sensors. Spatial resolution and the lowest measurement height is also a limitation for sodar and lidar, which cannot observe flow close to the ground. Conversely, maximum vertical extent is limited by the height of a mast, which is typically confined to the ASL. Environmental conditions can prohibit the use of tethersondes altogether, limiting the ability to collect in situ turbulence observations above a micrometeorological mast.

One of the first major field campaigns to incorporate UASs for SBL research, the Innovative Strategies for Observations in the Arctic Atmospheric Boundary Layer (ISO-BAR) field campaign was conducted at 65°N latitude off the island of Hailuoto, Finland, in February 2017 and 2018 (Kral et al., 2018, 2021). Herein we refer to the 2018 portion of the campaign as "ISOBAR18". The ISOBAR18 campaign aimed to address many of the previously mentioned gaps in SBL understanding by combining conventional ABL observations (instrumented masts, sodars, and a lidar) with an innovative deployment of UASs. During intensive observational periods (IOPs), flights were continually conducted above the sea ice just off the west coast of the island. Airspace permissions allowed flights up to 1800 m, which enabled sampling by UASs to capture the entirety of the SBL vertical structure, even at night and in the presence of clouds and fog. Observations from this campaign have been used for verification of gradient-based similarity scaling of the SBL (Greene et al., 2022) as well as model evaluation of flow over simulated sea ice (Lorenz et al., 2022).

1.2.2 Characterizing Novel Observations in the SBL

Some potential avenues for understanding the ability of UAS observations to improve NWP models include case studies with novel data assimilation techniques (Flagg et al., 2018; Jensen et al., 2021, 2022) as well as observing system simulation experiments (OSSEs; Moore, 2018; Chilson et al., 2019; Shenoy, 2021). These techniques all require characterization of the uncertainties involved with the UAS observations, which for simplicity are typically assumed to be constant and related to general sensor biases. Considerable progress has been made in recent years to characterize uncertainties in UAS observations due to sensor placement (Greene et al., 2018, 2019; Barbieri et al., 2019), sensor response times (Houston and Keeler, 2018, 2020; Segales et al., 2021), and improved wind vector estimations (González-Rocha et al., 2019, 2020). Although these studies have been critical for establishing UAS technology as a legitimate observational technique, few studies have examined how well these novel platforms can characterize atmospheric flow at larger scales.

A relatively unexplored method of assessing the representativeness of observations within the SBL is through an analysis of random errors, which arise due to averaging a stochastic signal over an insufficient time period for the time mean to converge to the true ensemble mean by the ergodic hypothesis (Lumley and Panofsky, 1964; Sreenivasan et al., 1978; Mann and Lenschow, 1994; Lenschow et al., 1994). Random errors fundamentally differ from those due to instrument bias, imprecision, or dynamic response, as random errors are mitigated by increased averaging time whereas instrumental errors are relatively unaffected by this and instead require regular calibration. For context, random errors can still be of the same order of magnitude as instrumental errors for many parameters (Salesky et al., 2012; Salesky and Chamecki, 2012; Bell et al., 2020), and theoretically all these errors independently compound. Quantifying

the relative random errors for atmospheric parameters within the SBL typically observed by UAS and surface-based eddy-covariance systems is therefore an important framework to consider.

1.3 Coherent Structures in turbulent wall-bounded flows

In recent decades, researchers have come to recognize the importance of coherent, organized structures within neutrally-stratified wall-bounded turbulent flows, which can account for a majority of turbulent fluxes close to the wall (Corino and Brodkey, 1969; Wallace et al., 1972; Willmarth and Lu, 1972; Guala et al., 2006; Balakumar and Adrian, 2007; Wallace, 2016). The streamwise spatial extent of these structures can exceed the depth of the flow itself, z_i. The Reynolds number Re within the ABL effectively approaches infinity, implying that viscous forces are relevant only at small scales and near the wall. Turbulence in the ABL is typically dominated by shear in the inner layer (also known as the surface layer) for $0 \lesssim z/z_i \lesssim 0.1$ or by buoyancy and Coriolis forcings in the outer (or intertial) layer for $z/z_i \gtrsim 0.1$. Within the inner layer, turbulence can be generated by hairpin vorticies that eject low-momentum fluid vertically upwards (i.e. $u' < 0$ and $w' > 0$), which serves to generate additional hairpin vortices that continually bound regions of low-momentum fluid (Head and Bandyopadhyay, 1981; Meinhart and Adrian, 1995; Adrian, 2007). Conversely, structures within the outer layer can affect turbulence within the inner layer by sweeping high-momemtum fluid downwards towards the wall (i.e. $u' > 0$ and $w' < 0$). These collections of hairpin vortices, known as large-scale motions (LSMs), have been widely studied in the fluid mechanics community since the early 1970s (e.g., Kovasznay et al., 1970; Brown and Thomas, 1977; Nakagawa and Nezu, 1981; Murlis et al., 1982; Wark and Nagib,

1991; Adrian et al., 2000; Ganapathisubramani et al., 2003; Tomkins and Adrian, 2003; Del Álamo et al., 2004). LSMs are characterized by regions of high- and low-momentum fluid in the log-layer region of high Re flows (also known as the inertial sublayer, which can overlap between the inner and outer layers) that scale as $\mathcal{O}(z_i)$ in the streamwise direction and can comprise of several successive hairpin vortices propagating at similar speeds (Adrian, 2007).

It has also been found that LSMs can organize into superstructures known as very-large-scale motions (VLSMs) that can extend $\mathcal{O}(10z_i)$ in the streamwise direction (Cantwell, 1981; Kim and Adrian, 1999; Guala et al., 2006; Balakumar and Adrian, 2007; Hutchins and Marusic, 2007a; Marusic and Hutchins, 2008). Studies examining VLSMs have only been possible more recently due to limitations of Re accessible by laboratory setups and direct numerical simulations (DNSs), but since the early 2000s they have been identified in turbulent channel flows (Del Álamo et al., 2004; Chung and McKeon, 2010), pipe flows (Guala et al., 2006), and ABLs (Tomkins and Adrian, 2003; Hutchins and Marusic, 2007a,b; Lee and Sung, 2011).

One common area of focus when studying the morphology of LSMs and VLSMs involves quantifying the inclination angle, γ, of these structures. This angle is defined relative to the surface (Brown and Thomas, 1977; Rajagopalan and Antonia, 1979), and for neutrally-stratified flows is commonly found to be $\gamma = 15°$ and is invariant with respect to Re (Marusic and Heuer, 2007). Studies typically employ two-point correlations for streamwise velocity or cross-correlations between velocity and surface shear stress as functions in both height z and streamwise lag of maximum correlation Δ_x^* to determine the inclination angle as $\gamma = \arctan(z/\Delta x^*)$ (e.g., Kovasznay et al., 1970; Brown and Thomas, 1977; Rajagopalan and Antonia, 1979; Boppe et al., 1999; Ganapathisubramani et al., 2005; Marusic and Heuer, 2007; Hutchins et al., 2012).

1.3.1 Unstable Stratification

It is generally well understood that buoyancy can significantly affect the nature of turbulence under unstable stratification, for example in terms of integral lengthscales (Sullivan et al., 2003; Salesky et al., 2013), the turbulence kinetic energy (TKE) budget (Wyngaard and Coté, 1971; Salesky et al., 2017), and velocity and temperature spectra (Kaimal and Finnigan, 1994). The effects of buoyancy on inner-outer scale interactions, however, have only recently been explored in the literature. Salesky et al. (2017) explored the role of instability on the organization of motions within the CBL using a suite of large-eddy simulations (LESs; Stoll et al., 2020) at varying levels of instability, and demonstrated a transition between modes from quasi-two-dimensional horizontal convective rolls (HCRs) under weak surface heat fluxes relative to large mean wind shear towards open cellular convection reminsicent of Rayleigh-Bénard convection as instability increases. These HCRs are typically aligned within 10–20° of the geostrophic wind vector (Weckwerth et al., 1996, 1997, 1999) and can act to spatially partition the distributions of turbulent fluxes (Salesky et al., 2017). Under increasing instability, the inclination angles of LSMs in the CBL have been found to increase past 50° (Salesky and Anderson, 2018, and references therein), which is consistent with the topological transition towards vertical buoyant plumes at high instability. Using sonic anemometer data from the ABL, Li et al. (2022) also examined the relationship between stability, inclination angle, and aspect ratio of coherent structures in the context of self-similar wall-attached eddies after Townsend (1976) (also see Woodcock and Marusic, 2015; Marusic and Monty, 2019). They found that coherent structures have an aspect ratio close to unity under neutral stratification, and become progressively taller and wider under increasing unstable stratification. For unstable conditions, they also found structures to be inclined at greater angles at larger scales as compared with smaller scales.

The changes in LSM and VLSM structure under convective conditions also can be detected by examining how turbulent transport efficiencies (fraction of the net flux in the downgradient direction) change for momentum versus scalars such as heat and moisture. Using atmospheric surface data, Li and Bou-Zeid (2011) found that under near-neutral stratification, momentum and scalars are transported by the same updrafts with high correlations. With increasingly unstable conditions, they observed a reduction in the transport efficiency of momentum paired with an increase in scalar transport efficiency, indicating these processes are governed by differing mechanisms related to the structure of vertical plumes. Through quadrant analysis, (also referred to as conditional sampling; e.g., Wallace et al., 1972; Willmarth and Lu, 1972; Holland, 1973; Grossman, 1984; Finnigan, 2000; Wallace, 2016) they further identified that under higher instability, vertical motions preferentially organize into rapid, intense updrafts compensated by longer, weaker downdrafts. Salesky et al. (2017) later confirmed these findings, further noting that these differences are related to the spatial distribution of individual quadrant events which are in turn affected by global stability.

Following the procedure of Mathis et al. (2009a), Salesky and Anderson (2018) examined the effects of buoyancy on inner-outer interactions through the lens of amplitude modulation (AM). The AM analysis begins by decomposing a signal into large- and small-scale components via low and highpass filtering, followed by determining the small-scale envelope function via Hilbert transforms. After again filtering this envelope with a lowpass filter to extract the large-scale envelope of the small-scale signal, one can compute the correlation between this envelope and the large-scale component of the raw signal. By repeating this process with simulated eddy-covariance tower data at multiple heights within CBLs across varying stabilities, Salesky and Anderson (2018) found the strongest correlations for the least convective cases considered. They also noted that significant correlations existed for all cases as long as there existed sufficient

separation between inner and outer peaks in the premultiplied spectrograms. Their results indicated that small-scale fluctuating velocity, temperature, and instantaneous second-order moments can be modulated by the large-scale streamwise and vertical velocity components associated with LSMs. Salesky and Anderson (2018) conclude with a conceptual model illustrating the effects of buoyancy on LSM inclination angles and how LSMs at varying stabilities act to modulate surface-layer turbulence.

1.3.2 Stable Stratification

While a majority of research on LSMs focus on neutrally and unstably stratified flows, analogous investigations of stably stratified flows are not as prominent. As discussed previously in Section 1.1.1, turbulence within the SBL is difficult to observe or simulate due to the buoyant suppression of vertical motions which results in turbulence that is weak and highly localized in space and time (Lan et al., 2018). With increasing stability, turbulent eddies become decoupled from the surface and scale with local stability (Nieuwstadt, 1984; van de Wiel et al., 2008), and eventually z loses relevance as a characteristic lengthscale (the so-called z-less regime, e.g., Wyngaard and Coté, 1972; Dias et al., 1995; Grachev et al., 2013).

Due to the nature of scales involved, most of the studies examining coherent structures in stably stratified flows leverage DNSs of channel or free-shear flows (e.g., García-Villalba and del Álamo, 2011; Watanabe et al., 2018, 2019; Atoufi et al., 2021; Gibbs et al., 2022). Watanabe et al. (2019) confirmed the existence of hairpin vortices within stably stratified free shear layers, noting their strong similarity to those typically observed in wall-bounded turbulent flows. They observed that while these hairpin vortices could be found throughout the shear layer, so-called superstructures (collections of multiple individual hairpin vortices that can be up to 10 times larger than the depth of the shear layer) only exist in the center of the layer. The authors also noted strong

turbulent mixing in cospectra at the wavelengths associated with the horizontal extent of individual hairpin vortices, and that the composite superstructures are responsible for large peaks in density and velocity spectra at wavelengths associated with the streamwise length of these structures. In a DNS investigation of stratified channel flow, García-Villalba and del Álamo (2011) considered a wide range of stability and noted several key findings. Two-dimensional energy density analysis indicated that the primary effect of stratification is to damp the large-scale modulation of intensity of near-surface streaks caused by global stability modes. Close to the surface, vertical motions are largely unaffected by stability as the flow is dominated by wall effects and coherent structures within the outer layer of the flow are not tall enough to penetrate down to the surface due to the suppression of vertical motions by negative buoyancy. They argue that stratification prevents the formation of larger scale structures by damping turbulent vertical fluxes at those scales.

Observational studies in in the SBL largely agree with these findings, particarly when vertical wind shear is weak which enables the development of strong vertical temperature gradients due to the lack of vertical mixing (Lan et al., 2018). In these cases, turbulence becomes highly localized into thin layers that are completely decoupled from the surface. In weakly stable boundary layers with high levels of coupling, Lan et al. (2019) found that large eddies can contribute equally to both turbulent production and transport, resulting in fluxes that were nearly constant with height. However, for increasing stability, such large eddies do not contribute evenly thereby resulting in nonzero vertical gradients of fluxes. Lan et al. (2022) found that sudden events of wind profile distortion can trigger large eddies that penetrate downwards and initiate a transition towards lower stability as they induce enhanced regions of

turbulent transport, increased fluxes, and reduced TKE and flux gradients across layers. With such weak turbulent motions, these studies elucidate the imprtance of large eddies in the SBL when they are able to penetrate across scales in the vertical.

Extending the analysis of stability effects on inclination angle to stably stratified channel flow, Gibbs et al. (2022) recently found that structures become increasingly inclined with height above the lower boundary up to $z/h = 0.15$, where h is the boundary-layer depth. Above this height, the inclination angles level off, which they discuss is indicative of a region where local z-less scaling behavior may no longer exist (Grachev et al., 2013). Moreover, they found that the inclination angle decreases with increasing stability at all heights, and that angles inferred from buoyancy structures are larger than those from momentum.

Although these studies have provided foundational context on the existence of turbulent coherent structures in stably stratified flows, they are limited in Reynolds number Re by at least four orders of magnitude when compared with typical SBL flows. At these scales, the LES technique offers the ability to simulate high-Re flows with relative computational efficiency at the expense of not being able to explicitly resolve the fine-scale dynamics. This tradeoff results in a statistical dependence on grid resolution that becomes especially important for SBL studies (Khani and Waite, 2014; Sullivan et al., 2016; Khani, 2018; Dai et al., 2021; Maronga and Li, 2021; Greene and Salesky, 2022). One of the few studies on coherent structures in the SBL that employed LES, Sullivan et al. (2016) utilized a fine grid spacing of $\Delta = 0.39$ m to simulate the SBL with varying surface cooling rates to induce increasing levels of static stability. They focused on the nature of localized coherent boundaries in the temperature field, and how these so-called microfronts act upon the surrounding flow. Through conditional averaging, the authors identified ring and hairpin vortices along the frontal boundaries that also lie within the energy-containing range of the turbulent flow. These frontal boundaries

were also present in the DNS experiments of Gibbs et al. (2022), who similarly noted how their inclination angles flattened with height above the surface. Huang and Bou-Zeid (2013) additionally presented two-point correlation statistics on horizontal planes at varying heights within the SBL along with profiles of integral lengthscales. They concluded that turbulence becomes increasingly local with stability and that coherent structures are buoyantly suppressed in the vertical, leading to elongated features in the streamwise direction.

1.4   Research Questions

It is abundantly clear that although understanding turbulence within the SBL has far-reaching implications for society from public health to the declining polar sea ice extent, there remains considerable progress to be made. Recent advancements in observational strategies such as the use of uncrewed aircraft systems in field operations fortunately present a unique opportunity to observe the SBL at unprecedented scales. Furthermore, the large-eddy simulation technique offers a compromise between reduced computational expense and a reduction in the explicit representation of resolved scales within simulated flows. By building from the growing community knowledge of accurately simulating idealized SBLs, LES can be a powerful tool for examining both the context of UAS measurements as well as exploring some of the underlying processes governing SBL dynamics. This dissertation therefore seeks to answer the following research questions through a novel synthesis of UAS observations and LES of the SBL:

1. Do gradient-based similarity functions based on ISOBAR18 eddy-covariance data collapse to common functions of the Richardson number Ri?

2. What considerations are necessary to appropriately extend the application of these gradient-based similarity functions to UAS vertical profile data?

3. How do random errors depend on atmospheric stability and measurement height for various first- and second-order turbulence moments?

4. How well do emulated UAS and eddy-covariance measurements represent the ensemble mean?

5. What considerations are necessary to mitigate random errors for observations in the SBL?

6. How does stability impact the properties of large-scale motions within the SBL?

7. How does buoyancy affect transport efficiencies of momentum and temperature?

8. How do coherent structures with the SBL contribute to these differences?

This dissertation is structured as follows. In Chapter 2, UAS and tower-mounted eddy-covariance data from the ISOBAR18 campaign are utilized to examine questions 1–2. In Chapter 3 the representativeness of UAS and eddy-covariance observations within the SBL are explored through a random error analysis of large eddy simulations to address questions 3–5. The existence and characteristics of coherent structures within the SBL are investigated in Chapter 4 to address questions 6–8. Finally, all of these results are summarized in Chapter 5 along with an outlook on the future of SBL studies using UAS and LES.

Chapter 2

Gradient-based Turbulence Estimates from Multicopter Profiles in the Arctic Stable Boundary Layer

2.1 Research Objectives

In this chapter, we combine the gradient-based similarity framework from Sorbjan (2010) with new observations from the ISOBAR18 campaign to address the following key questions:

1. Do gradient-based similarity functions based on ISOBAR18 eddy-covariance data collapse to common functions of the Richardson number Ri?

2. What considerations are necessary to appropriately extend the application of these gradient-based similarity functions to UAS vertical profile data?

and their corresponding hypotheses:

1. The data utilized in previous studies to develop the gradient-based similarity relationships featured strong horizontal homogeneity. By filtering the ISOBAR18 eddy-covariance data to analyze only onshore flow, non-dimensionalized turbulent moments collapse to universal functions of Ri.

2. Uncrewed aircraft system observations are quasi-instantaneous in situ observations, whereas the turbulence scaling typically relies on temporally averaged quantities. By averaging multiple sequential profiles, it is possible to obtain physically meaningful profiles of estimated turbulent quantities with the gradient-based similarity theory.

This chapter is organized in the following manner: Section 2.2 outlines the background and theory of traditional surface layer turbulence scaling and reviews the gradient-based scaling framework. An overview of the ISOBAR18 campaign and observational systems are presented in Section 2.3. Section 2.4 addresses research question 1 by detailing results from similarity scaling ISOBAR18 eddy-covariance data, and Section 2.5 builds off those results by extending the gradient-based scaling to three different case studies of UAS profiles from the ISOBAR18 campaign to address research question 2. Overall discussion and caveats are provided in Section 2.6 followed by concluding remarks in Section 5.1.1.

2.2   Background

Since the mid-twentieth century, MOST has provided a framework to describe turbulence in thermally stratified ASL flows based on the concept of similarity scales with three independent physical units. The MOST framework formally applies only to the ASL where the vertical flux divergence is weak (i.e., fluxes vary by less than 10% compared to their surface values), and is based on the hypothesis that scaled statistics of turbulence collapse to universal functions of the stability parameter $\zeta = z/L$. Here, z represents the height above ground level and L is the Obukhov length scale (Obukhov, 1946) defined as

$$L = -\frac{u_*^3 \theta_0}{\kappa g \overline{w'\theta'}}\bigg|_0,$$

(2.1)

with the friction velocity, $u_* = \left(\overline{u'w'}^2 + \overline{v'w'}^2 \right)^{1/4}$; the surface potential temperature, θ_0; the von Kármán constant, κ (see Högström, 1988); the acceleration due to gravity, g; and the vertical kinematic heat flux, $\overline{w'\theta'}$. Here, u, v, and w are the streamwise, lateral, and vertical velocity components, respectively. In this notation, quantities with a prime denote fluctuating components about the mean values and an overbar denotes the Reynolds averaging operator, whereas the subscript 0 indicates surface values. The MOST scaling results in non-dimensional vertical gradients of the mean wind speed and potential temperature, respectively, as

$$\frac{\kappa z}{u_*}\frac{\partial U}{\partial z} = \varphi_m(\zeta), \tag{2.2a}$$

and

$$\frac{\kappa z}{\theta_*}\frac{\partial \overline{\theta}}{\partial z} = \varphi_h(\zeta), \tag{2.2b}$$

where U is the wind speed, $\theta_* = -\overline{w'\theta'_v}/u_*$ is the temperature scale based on the surface kinematic heat flux and friction velocity, and φ_m and φ_h are dimensionless universal functions of the stability parameter ζ. Note that these functions are not prescribed by MOST and must be determined empirically. In this chapter, we consider both the Businger–Dyer (Businger et al., 1971) and the SHEBA profile functions (Grachev et al., 2007). In their re-evaluated form (Högström, 1988), with an adjusted von Kármán constant of $\kappa = 0.40$, the Businger–Dyer formulations for stable conditions ($\zeta > 0$) are

$$\varphi_m^{\mathrm{H}} = 1 + 6\zeta, \tag{2.3a}$$

$$\varphi_h^{\mathrm{H}} = 0.95 + 7.8\zeta, \tag{2.3b}$$

where the superscript H represents Högstrom. We note that it is also commonly accepted to use $\varphi_m = \varphi_h = 1 + 5\zeta$ for $\kappa = 0.4$ in the SBL (e.g., Kaimal and Finnigan, 1994), which has the advantage of simplicity over other empirical formulations. Perhaps more applicable to the ISOBAR18 campaign data, Grachev et al. (2007) determined empirical forms of the MOST formulations based on data from the SHEBA campaign to take the form (with superscript S representing SHEBA)

$$\varphi_m^{\mathrm{S}} = 1 + \frac{6.5\zeta(1+\zeta)^{1/3}}{1.3+\zeta} \tag{2.4a}$$

$$\varphi_h^{\mathrm{S}} = 1 + \frac{5\zeta + 5\zeta^2}{1 + 3\zeta + \zeta^2}. \tag{2.4b}$$

Several studies (e.g., Nieuwstadt, 1984; Sorbjan, 1986, 1988) have shown that MOST can be applied to the entire SBL depth (where the ASL may be shallow and not well-defined) by utilizing local instead of surface scales when defining the MOST functions in Equation 2.2. In this framework, it is possible to define the gradient Richardson number Ri as

$$Ri = \frac{z}{\Lambda} \frac{\varphi_h(z/\Lambda)}{\varphi_m^2(z/\Lambda)}, \tag{2.5}$$

where Λ is the local Obukhov length and defined as in Equation 2.1 except using local vertical stresses and kinematic heat fluxes. Substituting the Högström and SHEBA formulas under stable conditions (Eqs. 2.3, 2.4) yields

$$Ri^{\mathrm{H}} = \frac{z}{\Lambda} \frac{0.95 + 7.8z/\Lambda}{(1 + 6z/\Lambda)^2}, \tag{2.6a}$$

$$Ri^{\mathrm{S}} = \frac{z}{\Lambda} \left[1 + \frac{5\frac{z}{\Lambda} + 5(\frac{z}{\Lambda})^2}{1 + 3\frac{z}{\Lambda} + (\frac{z}{\Lambda})^2} \right] \left[1 + \frac{6.5\frac{z}{\Lambda}(1 + \frac{z}{\Lambda})^{1/3}}{1.3 + \frac{z}{\Lambda}} \right]^{-2}. \tag{2.6b}$$

Turbulent motions in the SBL are commonly weak (and intermittent for increasing stability), which leads to poor definitions of the MOST scales $u_*, \theta_*,$ and L. As a

consequence, the form of the universal functions in Equation 2.2 yields ambiguous results as $z/L \to 0/0$ for increasing thermal stratification. Yano and Wacławczyk (2021) attempt to circumvent this limiting case through a generalized nondimensionalization of the governing equations that alternatively defines characteristic length scales in the ABL, although further work is needed to better define boundary conditions for different applications. Moreover, the MOST universal functions become susceptible to self-correlation as u_* and θ_* appear on both sides of Equation 2.2, which leads to artificially strong agreement between theory and observations for φ_m and poor agreement for φ_h (Baas et al., 2006).

To overcome these issues in the SBL, Sorbjan (2010) proposed a "master" scaling scheme based upon vertical gradients, defining similarity scales for length, velocity, and temperature in the SBL as, respectively,

$$L_s = \ell, \tag{2.7a}$$

$$U_s = \ell\ N, \tag{2.7b}$$

$$T_s = \ell\ \Gamma, \tag{2.7c}$$

where ℓ is a mixing length after Prandtl (1925), the Brunt–Väisälä frequency $N = \sqrt{\beta\Gamma}$, $\Gamma = \partial\theta/\partial z$ is the local vertical potential temperature gradient, and $\beta = g/T_0$ is the buoyancy parameter with T_0 being a reference surface temperature. Originally, Sorbjan (2010) approximated $\ell = \kappa z$ based upon surface-layer scaling in the neutral limit. To extend the applicability of these similarity scales beyond the surface layer where ℓ is expected to increase nonlinearly with height, Sorbjan (2017) showed that the mixing lengths for momentum and heat in any stably stratified fluid are equal and can be approximated as

$$\ell = \frac{\kappa z}{1 + \frac{\kappa z}{\lambda_0} + \frac{\kappa z}{\lambda_1}}, \tag{2.8}$$

25

where $\lambda_0 = 19.22$ m, $\lambda_1 = c/Ri^{3/2}$, $c = 1$ m, and $Ri = N^2/S^2$ is the Richardson number where

$$S = \sqrt{(\partial\overline{u}/\partial z)^2 + (\partial\overline{v}/\partial z)^2} \qquad (2.9)$$

is the local vertical gradient of the horizontal wind vector. Herein, we utilize the blended mixing length ℓ defined in Equation 2.8 when defining and calculating the gradient-based similarity scales in Equation 2.7.

In this scaling framework, Sorbjan (2010) defined four universal dimensionless functions of the Richardson number as

$$\frac{u_*^2}{U_s^2} = G_m(Ri), \qquad (2.10a)$$

$$-\frac{\overline{w'\theta'}}{U_s T_s} = G_h(Ri), \qquad (2.10b)$$

$$\frac{\sigma_w}{U_s} = G_w(Ri), \qquad (2.10c)$$

$$\frac{\sigma_\theta}{T_s} = G_\theta(Ri), \qquad (2.10d)$$

with the standard deviations of the vertical velocity component and potential temperature, σ_w and σ_θ; and the universal similarity functions of the Richardson number, $G_m, G_h, G_w,$ and G_θ. Note that the notation from Sorbjan (2010) for this paper's Equation 2.10a has been changed to maintain consistency with the MOST function in Equation 2.2a. This is similar to how Monin and Obukhov (1954) defined universal functions of the stability parameter $\zeta = z/L$, except for that the use of Ri virtually eliminates the issue of self-correlation.

Using 1-h observations from the SHEBA campaign, Sorbjan (2010) and Sorbjan and Grachev (2010) introduced the following analytical empirical expressions for Equation 2.10 (including the modified version of G_θ from Sorbjan (2017)):

$$G_m = \frac{1}{Ri(1+300Ri^2)^{3/2}}, \qquad\qquad (2.11a)$$

$$G_h = \frac{1}{0.9Ri^{1/2}(1+250Ri^2)^{3/2}}, \qquad\qquad (2.11b)$$

$$G_w = \frac{1}{0.85Ri^{1/2}(1+450Ri^2)^{1/2}}, \qquad\qquad (2.11c)$$

$$G_\theta = \frac{3}{(1+1000Ri^2)^{1/2}}. \qquad\qquad (2.11d)$$

Sorbjan (2010) originally applied this framework to the range $0.001 < Ri < 0.7$ with observations from the SHEBA campaign and found strong agreement between all four scaled parameters in this range. He also noted that for $Ri > 0.7$, the turbulence kinetic energy budget dictates that turbulence no longer be stationary, and does not consider observations in this range. Sorbjan (2017) further demonstrated the validity of this framework using large-eddy-simulation output in the range $0.02 < Ri < 0.2$, also noting strong agreement. As will be shown, a majority of the ISOBAR18 observations fall within the range $0.005 < Ri < 0.3$, which is consistent with Sorbjan (2010).

The utility of the gradient-based similarity framework (Eqs. 2.7, 2.10) also extends beyond micrometeorological mast observations. If one were to obtain vertical profiles of potential temperature and wind speed within the SBL, they could then construct vertical profiles of Ri as well as the gradient-based similarity scales (Equation 2.7). With Ri they could then evaluate the magnitude of the similarity functions using the empirical expressions in Equation 2.11. Finally, by rearranging Equation 2.10 and multiplying the similarity functions by their corresponding gradient-based scales, they

can produce an estimate of the desired turbulent parameters. For example, in the case of estimating u_*^2, the calculation would be

$$u_*^2 = G_m(Ri)U_sU_s = \frac{(\ell N)^2}{Ri(1 + 300Ri^2)^{3/2}},$$ (2.12)

with ℓ, N, and Ri calculated directly from observations.

We aim to evaluate the performance of the gradient-based similarity framework with a multifaceted approach. In Section 2.4, we will validate the formulation of the empirical similarity functions (Equation 2.11) using eddy-covariance observations from the ISOBAR18 campaign. After the empirical functions are deemed appropriate for the conditions observed during the campaign, in Section 2.5 we turn our attention to vertical profile observations collected by UASs. There we assess the conditions necessary to adequately estimate profiles of turbulent moments with the approach summarized in Equation 2.12.

2.3 ISOBAR18 Campaign Overview

The 2018 portion of the Innovative Strategies for Observations in the Arctic Atmospheric Boundary Layer campaign (ISOBAR18) took place over the sea ice of the Bothnian Bay off the western coast of the Finnish island Hailuoto at 65°N (Kral et al., 2021). During this month-long campaign, numerous observation systems, including micrometeorological masts, boundary-layer remote-sensing systems, and various UASs, were utilized over the sea ice or on the coast during February 2018, resulting in eight IOPs. In this chapter, we make use of data from the 10-m micrometeorological tower,

Figure 2.1: Panoramic photo taken on the sea ice west of Hailuoto, Finland, on 18 February 2018. In the center of the image (facing south) are the GFI1 and GFI2 meteorological towers. On the right side (facing west) is the orange takeoff and landing pad, which acted as the primary launch point for the CopterSonde during ISOBAR18. The island of Hailuoto is visible on the left side of the image (facing east). It is apparent from this image that atmospheric flows from the south and west have relatively unobstructed fetches across sea ice and snow.

the ground-based Doppler wind lidar, the vertically sampling ground-based Doppler sodar, and the rotary-wing UAS. A summary of these instruments and their specifications are outlined in Table 2.1.

An integral component of the observational systems during the ISOBAR18 campaign was the inclusion of two micrometeorological masts on the sea ice just off the coast of Hailuoto (Figure 2.1; for a map, see Figure 1 in Kral et al., 2021). The primary mast utilized in this chapter (Figure 2.2d; herein GFI2, denoting the second University of Bergen Geophysical Institute mast and consistent with Kral et al., 2021) was 10.3-m tall with multiple levels of instruments. Of note, these included three levels of eddy-covariance systems (CSAT-3, Campbell Scientific, Logan, Utah, USA) located at 1.97, 4.55, and 10.31 m, and three levels of thermocouple temperature measurements located at 0.6, 1.9, and 6.9 m. The thermocouple measurements are available at 1-s resolution, but 10-min averages were utilized in this chapter.

For a near-continuous monitoring of vertical profiles of the three-dimensional wind vector, a Leosphere WindCube v1 Doppler wind lidar (Figure 2.2b; Kumer et al., 2014, 2016) was deployed on the shoreline halfway through the ISOBAR18 campaign. This

Figure 2.2: Pictures of the instruments in this chapter taken in Hailuoto, Finland, during the ISOBAR18 campaign: (a) the CopterSonde with sensors mounted inside an aspirated right-angle duct on the front of the aircraft (credit: Bill Doyle, Universty of Oklahoma), (b) the WindCube v1 Doppler lidar (credit: Joachim Reuder, University of Bergen), (c) the LATAN-3M vertically pointing sodar (credit: Joachim Reuder, University of Bergen), and (d) the 10-m GFI2 instrumented tower (credit: Andrew Seidl, University of Bergen).

lidar sampled at 1 Hz (0.25 Hz for independent observations) at ranges of 45, 65, 85, 105, 125, 145, 165, 185, 205, and 255 m above mean sea level (a.m.s.l.). Standard deviations of the vertical velocity component σ_w are estimated based on averages of the 1 s Doppler spectral broadening, and thus correspond to a spatial average over the 20-m range gate.

We additionally make use of observations from the vertically-sampling sodar (Figure 2.2c, LATAN-3M; Kouznetsov, 2009). The sodar sampled the ABL vertically every 3 s to produce time–height depictions of the attenuated backscatter signal, which is used primarily to classify the vertical structure of the SBL and diagnose its height in the case studies presented in Section 2.5.2.

Complementing these ground-based observing systems, the ISOBAR18 campaign also made extensive use of UAS technology to collect valuable in situ thermodynamic and kinematic observations of the lower atmosphere. For the lowest levels (from the surface to 300 m above ground level, a.g.l.), a series of different rotary-wing UASs flew vertical profiles once roughly every 20 min throughout the eight IOPs (Kral et al., 2021). Intensive operational periods were primarily conducted for periods with forecasted strong surface cooling and weak synoptic background flow. As will be discussed, the actual conditions during the IOPs varied from clear skies to intermittent fog and cloudiness. To achieve the highest level of data consistency, this chapter only focuses on observations from the CopterSonde UAS (Figure 2.2a; Greene et al., 2018, 2019; Segales et al., 2020) operated by the University of Oklahoma (U.S.).

Table 2.1: General specifications of the UAS, tower-mounted instruments, and ground-based remote sensors from ISOBAR18 specifically utilized in this chapter. The following variable conventions are used: T, temperature; RH, relative humidity with respect to liquid water; p, pressure; U, wd, wind speed and direction, respectively; $\sigma_u, \sigma_v, \sigma_w$, the three wind velocity standard deviations; and bsc, the attenuated backscatter signal. The processed heights and Δt refer to the value-added post-processed data as described in Section 2.3. Adapted from Kral et al. (2021).

Observing System	Parameter	Sensor	Acquired Frequency	Processed Heights	Processed Δt
GFI2 10-m mast	T	Campbell ASPTC (aspirated)	1 Hz	0.6, 2.0, 6.8 m	600 s
	u, v, w	Campbell CSAT-3	20 Hz	2.0, 4.6, 10.3 m	600 s
WindCube v1	u, v, w		0.25 Hz	45–255 m a.m.s.l.	600 s
Doppler lidar	$\sigma_u, \sigma_v, \sigma_w$		0.25 Hz	$\Delta z = 20$ m	
LATAN-3M	w, bsc		0.33 Hz	10–340 m a.m.s.l.	3 s
Doppler sodar (1D)				$\Delta z = 10$ m	
CopterSonde	T	iMet-XF PT 100	10 Hz	5–300 m	$\sim$ 5–8 s
Rotary-Wing UAS	T, RH	HYT 271	10 Hz	(maximum)	
	p	Pixracer barometer	10 Hz	$\Delta z = 5$ m	
	U, wd	Aircraft dynamics	10 Hz		

2.4 Evaluation of Similarity Relationships for Mast Data

As outlined at the end of Section 2.2, in this section we assess the performance of the empirical gradient-based similarity function (Equation 2.11) based on eddy-covariance observations during the ISOBAR18 campaign. To provide additional context and to highlight the differences between the two frameworks, we also present the same data scaled with the traditional MOST (Equation 2.2).

2.4.1 Mast Data Processing

Extracting turbulence statistics from the raw 20-Hz eddy-covariance observations requires considerable attention to detail (e.g., Lee et al., 2004; Foken, 2008). To streamline this process, we utilized the TK3.11 software package (Mauder and Foken, 2015), which tested for a physical range of observations, spikes, stationarity, and integration of developed turbulence. These quality checks resulted in various quality flags in the post-processed data. Based on an Ogive-analysis and a flux-convergence classification (following Foken et al., 2006), we utilized an averaging period of 10 min for data in this chapter. We further use an additional flag denoting statistical convergence within the spectral integration period of each 10-min eddy-covariance-data interval. After accounting for convergence to each eddy-covariance level separately, about 74.3% of the data are retained in total. The TK3 software also performed planar-fit coordinate transformations as well as the corrections outlined by Webb et al. (1980), Schotanus et al. (1983), and Moore (1986).

Like MOST, the gradient-based scaling framework outlined by Sorbjan (2010) relies on the underlying assumptions of horizontal homogeneity. Because of the GFI2 mast's proximity to the coast of Hailuoto, it is also necessary to filter measurements by the

prevailing wind direction to ensure a fetch across sea ice (Barskov et al., 2019). For this chapter, we impose a requirement that the flow must be from a sector between 150° (south-easterly) and 300° (north-westerly) based upon the geometry of the coastline (see Figure 1 in Kral et al., 2021, for a top-down view of the observational site). When accounting for wind direction in addition to the statistical flags mentioned previously, about 15.9% (1358 out of 8553) of the total 10-min data points from each of the three eddy-covariance levels remain for further analysis.

Vertical gradients of temperature and wind speed are calculated by first fitting second-order polynomials of the form

$$y = a \ln(z)^2 + b \ln(z) + c, \tag{2.13}$$

where y represents any atmospheric parameter and a, b, and c are empirical constants. In this form, it is convenient to calculate the vertical derivatives analytically as

$$\frac{dy}{dz} = \frac{1}{z}(2a \ln(z) + b). \tag{2.14}$$

Note here that vertical derivatives of wind speed are calculated using the vector wind components u and v thus taking the contribution of directional shear into account (Equation 2.9). With this method, we also specify a lower boundary condition $U(z = z_0) = 0$, where z_0 is the aerodynamic roughness length set to 0.001 m for sea ice, to constrain physically representative estimates of velocity gradients. Furthermore, we approximate $\partial\theta/\partial z \approx \partial T/\partial z + 0.01$ K m^{-1}. This analytical method is advantageous over finite differencing techniques because it enables the estimation of gradients at any height z within the bounds of the defined function as opposed to only one level arbitrarily between two observation points. Because the three levels of eddy-covariance

observations do not align with the three levels of slow-response temperature measurements, this enables us to bypass the interpolation required to directly calculate Ri at a specific height.

Resulting profiles of the scaled turbulence statistics rely considerably on the numerical methods employed to calculate vertical gradients using multiple observational levels. In this chapter we chose the second-order fit in Equation 2.13, as it performed markedly better than finite differencing (first and second order) and various other fitting functions (not shown). Other studies have demonstrated the efficacy of this technique for calculating vertical gradients in the SBL (e.g., Grachev et al., 2005, 2007), but we do acknowledge that there is no perfect method for every application.

After calculating the vertical gradients, we calculate Ri using the GFI2 0.6 m temperatures for T_0 in the buoyancy parameter. Following the method in Sorbjan (2010), Grachev et al. (2012), and Sorbjan (2017) to filter for outliers, we employ a prerequisite on Ri for an individual observation to be considered. After calculating Ri directly, an observation is omitted from further analysis if it does not fall within the range $0.5Ri^S < Ri < 2Ri^S$ (where Ri^S is defined in Equation 2.6b). After applying this final condition, about 12.1% (1031 out of the original 8553) of the total 10-min data points were considered in this investigation. We also construct the scaling parameters U_s, T_s, and L_s as defined in Equation 2.7 to estimate values of the dimensionless functions outlined in Equation 2.10. All of these are valid at the same heights as the three eddy-covariance systems. For clarity, bin-medians of the dimensionless turbulent statistics are computed based on Ri with each bin containing 25 individual observations at each eddy-covariance measurement level.

2.4.2 Results

The eddy-covariance results for the GFI2 tower are organized based on the similarity scaling frameworks, beginning first with the traditional MOST scaling as a baseline reference in Section 2.4.2.1. After highlighting the strengths and shortcomings of this method, results from the gradient-based scaling are presented in Section 2.4.2.2.

2.4.2.1 Local Monin–Obukhov Similarity Theory Scaling

Of the 1031 individual observations considered, 290 (about 28%) are in the "nearly-neutral" regime as defined by Sorbjan and Grachev (2010) with $0 < z/\Lambda < 0.02$, 681 (about 66%) are "weakly-stable" with $0.02 < z/\Lambda < 0.6$, and the remaining 60 (about 6%) are "very-stable" with $0.6 < z/\Lambda < 50$. In general, there appears to be good agreement between the observed dimensionless momentum fluxes φ_m as a function of the stability parameter z/Λ compared to the empirical Businger–Dyer and SHEBA formulations at all three eddy-covariance levels (Figure 2.3a). The spread in observed φ_m is largest in the "weakly-stable" regime. For $z/\Lambda > 0.1$, observed φ_m appears to closely follow the trend predicted by the SHEBA formulation (Equation 2.4), which has a smaller slope in log-log coordinates than the Businger–Dyer form (Equation 2.3). Otherwise, even at higher measures of stability, scaled bin-median observations of φ_m collapse to a common universal function in agreement with previous studies (e.g., Grachev et al., 2005, 2007, 2008; Sorbjan and Grachev, 2010).

Conversely, the observed dimensionless heat fluxes φ_h (Figure 2.3b) exhibit considerable spread at all stabilities and all eddy-covariance levels, differing by up to one order of magnitude in near-neutral and weakly-stable conditions. This large spread in φ_h and general lack thereof in φ_m is likely a result of self-correlation, as errors in heat flux observations (which appear in both θ_* and z/Λ) mathematically induce scatter
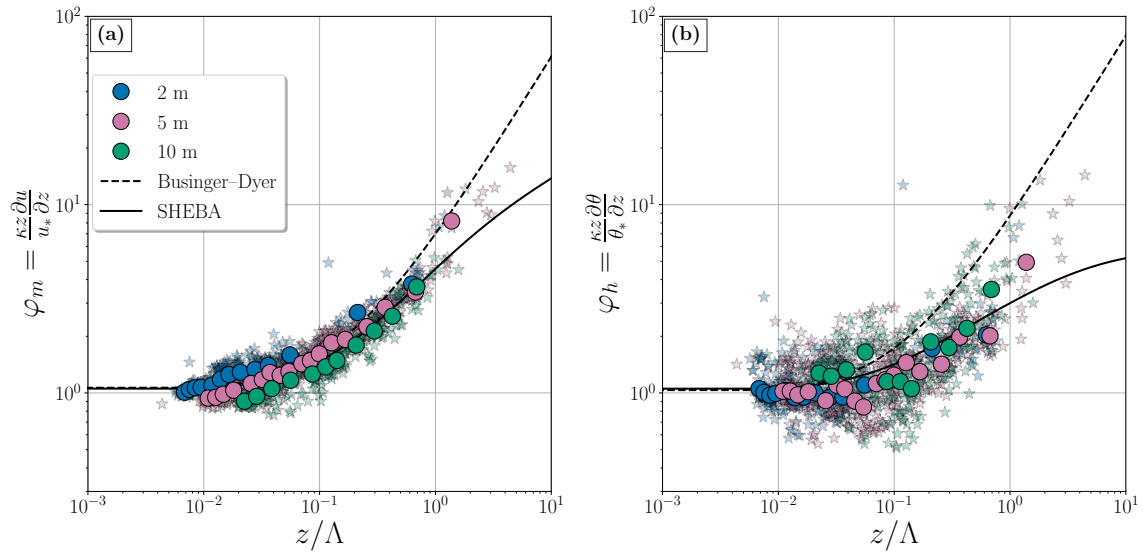
Figure 2.3: Dimensionless (a) momentum flux and (b) heat flux versus the local stability parameter $\zeta = z/\Lambda$ from each of the three sonic anemometer levels on GFI2 (color-coded by height) in log-log coordinates. In both figures, faded stars are individual observations, and shaded circles are bin-median values based on ζ for clarity. For reference, the solid and dashed black lines respectively represent the SHEBA and Businger–Dyer formulation of the MOST functions for stable conditions (Equation 2.3).
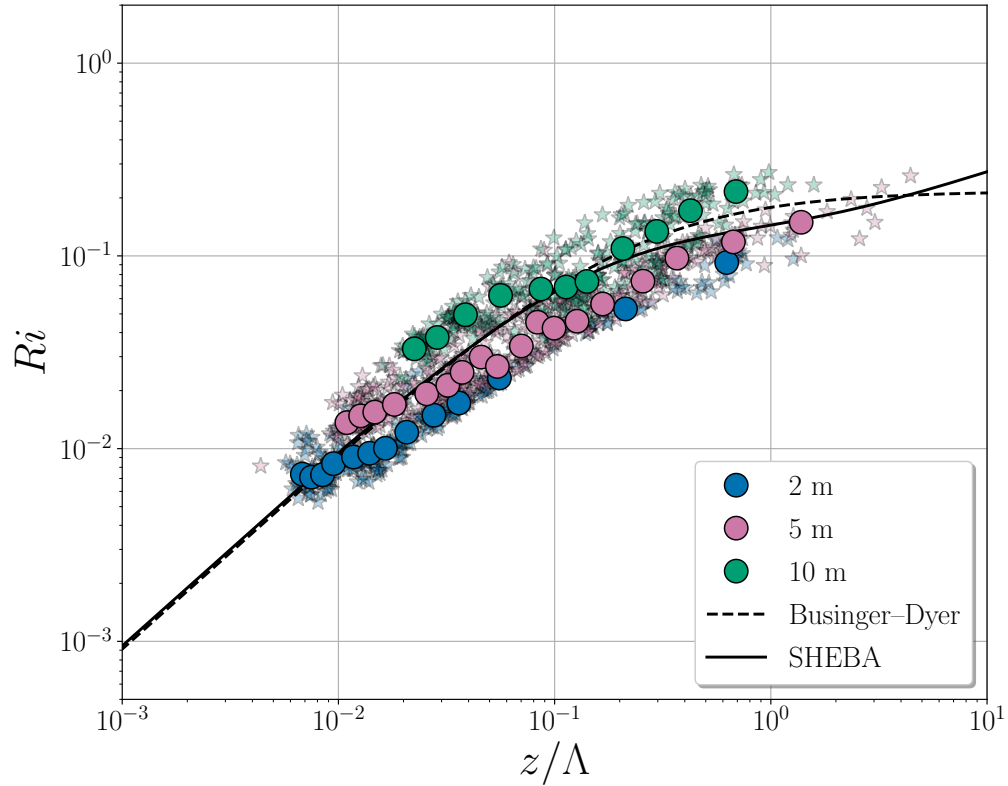
Figure 2.4: Direct calculation of the Richardson number Ri from each of the three GFI2 heights versus the stability parameter z/Λ in log-log coordinates during ISOBAR18. For reference, the theoretical relationship, based on the SHEBA (Businger–Dyer) formulation (Equation 2.6), is also drawn as the solid (dashed) black line. Individual observations appear as faded stars, and bin-median values appear as solid circles (as in Figure 2.3).

normal to the empirical function for φ_m in stable conditions (Baas et al., 2006). By this same principal, errors in momentum flux generally induce scatter along the empirical functions, which acts to artificially improve the correlation for φ_m (Baas et al., 2006). Moreover, uncertainties in evaluating the potential temperature gradient at the 10-m eddy-covariance level with data extrapolated from below this observational level likely contribute to the overall scatter in φ_h. This is also a relevant factor in the gradient-based similarity scales as discussed in the following subsection.

When examining the relationship between Ri and z/Λ (Figure 2.4), the effect of excluding outliers based on Ri and Ri^S is apparent as an envelope around the empirical Ri^S curve. In general, both the SHEBA and Businger–Dyer formulations appear to fit the trend in observations at all levels for $z/\Lambda < 0.1$. For increasing stability, individual observations and bin-medians at 2 and 5 m follow more closely with the SHEBA curve, whereas the 10-m data maintain larger values of Ri than predicted as z/Λ approaches 1. Without the Ri^S constraint described earlier, the overall spread in Ri is much larger about the empirical curve (not shown). This is undoubtedly related to the propagation of error from φ_h via Equation 2.5, and in itself provides justification for excluding outliers when evaluating the gradient-based similarity relationships in the following subsection. From Figure 2.4 it is also apparent that a majority of observations during the ISOBAR18 campaign fall in the ranges $0.02 < Ri < 0.12$, which is defined by Sorbjan (2010) as "weakly stable". Although this campaign took place in the Arctic during winter, we believe the presence of low-level clouds influenced by the marine boundary layer and heterogeneous ice covering in the mesoscale strongly influenced the net radiation balance at Hailuoto. Downwelling longwave radiation from these clouds dampens the ability of the surface to radiatively cool, thereby reducing the near-surface stability. As seen in the following subsection, these observations are still

well within the range to be appropriately characterized by the gradient-based scaling framework.

2.4.2.2 Gradient-Based Similarity Scaling

The dimensionless momentum and heat fluxes, G_m and G_h, and the dimensionless standard deviations of the vertical velocity component and temperature, G_w and G_θ, all show a strong dependence on the Richardson number, Ri (Figure 2.5). In general, all four of these scaled observations follow the SHEBA empirical formulations in Equation 2.11 for $0.005 < Ri < 0.3$. Specifically, we expect the following trends for near-neutral conditions:

$$G_m \sim Ri^{-1}, \tag{2.15a}$$

$$G_h \sim Ri^{-1/2}, \tag{2.15b}$$

$$G_w \sim Ri^{-1/2}, \tag{2.15c}$$

$$G_\theta \sim Ri^0. \tag{2.15d}$$

Sorbjan (2010) found the valid range of these near-neutral scaling laws to be for $Ri < 0.01$, which is also supported empirically by the ISOBAR18 data (Figure 2.5). Observations in this regime are effectively entirely from the 2-m level, which neatly collapse to the empirical functions in Equation 2.15 for all scaled moments except the potential temperature standard deviations.

A majority of the GFI2 mast observations occurred in the "weakly stable" regime, i.e. $0.02 < Ri < 0.12$ (Sorbjan, 2010). In this regime, scaled observations from all three eddy-covariance measurement levels appear to collapse to their empirical curves
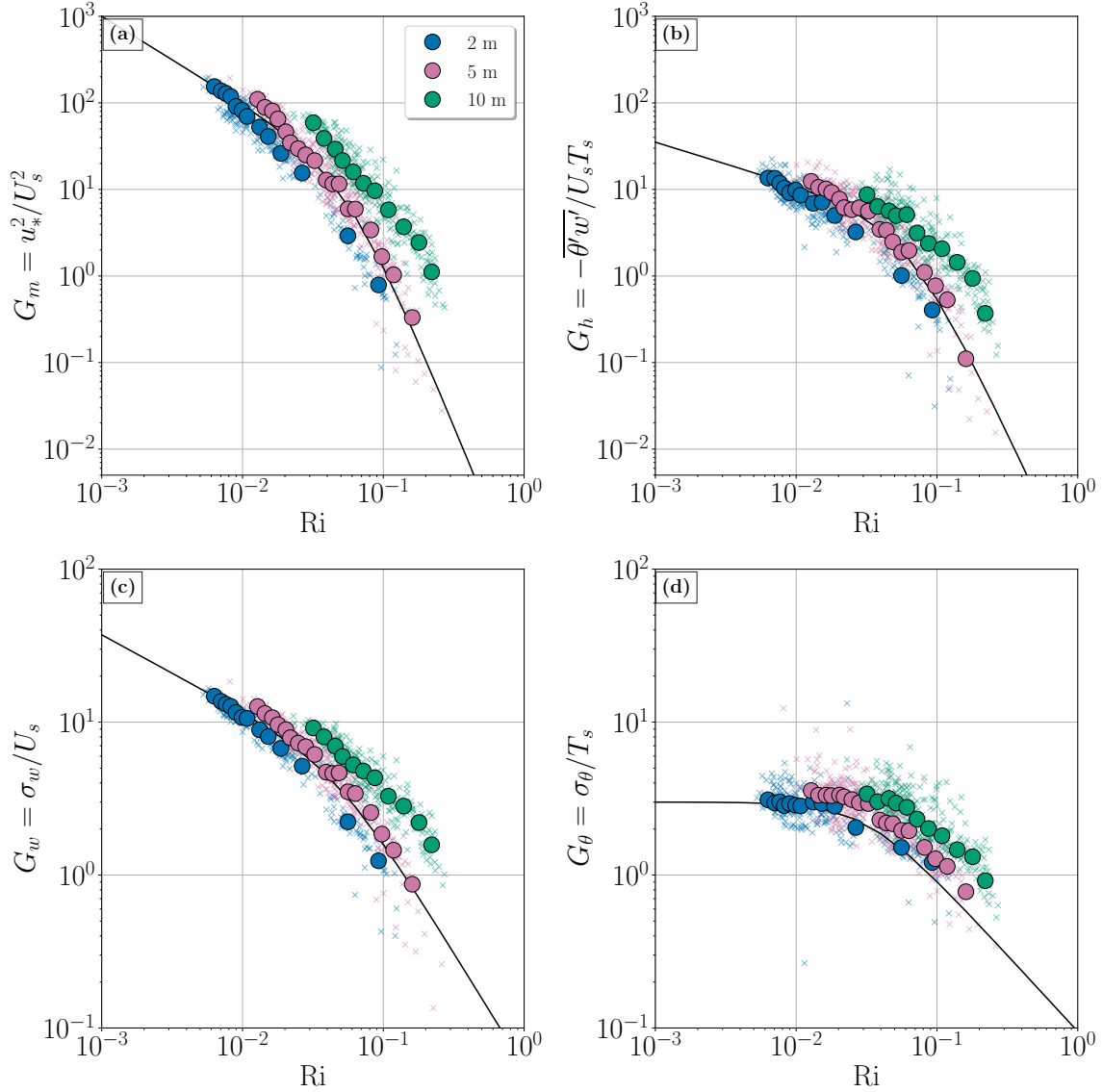
Figure 2.5: Relationship between dimensionless (a) momentum flux $G_m = u_*^2/U_s^2$, (b) heat flux $G_h = -\overline{w'\theta'}/U_s T_s$, (c) vertical velocity standard deviation $G_w = \sigma_w/U_s$, and (d) potential temperature $G_\theta = \sigma_\theta/T_s$ and Richardson number Ri. Individual points are plotted as faint Xs with bin-median values denoted by larger circles. All points are color-coded based on height. The solid black lines denote the empirical functions defined in Equation 2.11.

41

(Equation 2.11). As indicated by their bin-median values and individual observations (Figure 2.5), the 2-m and 5-m observations strongly agree with their predicted values. The 10-m observations in this range differ by a factor of 2–3, resulting in values larger than the empirical curves across all statistics. This is most likely related to the inability to constrain the temperature profile above 7 m (above the topmost thermocouple) and requiring extrapolation of the temperature gradient to the 10-m eddy-covariance level.

In the weakly stable regime, scatter in G_θ appears to be fairly large. Moreover, in this regime observations from 2-m appear to match the empirical curve of Equation 2.11d the closest whereas the 5 and 10-m observations are 30–40% larger on average, which is closer to the original formulation in Sorbjan (2010). This is a similar observation as that made by Sorbjan (2017), who reasoned that the dimensionless temperature standard deviation is not well defined because as $Ri \to 0$, $\sigma_\theta/T_s \to 0/0$.

Sorbjan (2010) also identified that the similarity functions begin falling off more drastically for stronger stability, namely for $0.1 < Ri < 0.7$, where they follow these scaling laws:

$$G_m \sim Ri^{-4}, \tag{2.16a}$$

$$G_h \sim Ri^{-7/2}, \tag{2.16b}$$

$$G_w \sim Ri^{-3/2}, \tag{2.16c}$$

$$G_\theta \sim Ri^{-1}. \tag{2.16d}$$

In general, the data appear to transition between the near-neutral scaling regime (Equation 2.15) to one of stronger stability (Equation 2.16) around $Ri \approx 0.1$. Similar to the weakly stable regime, the scaled observations from all three levels indeed fall off as expected even for Ri as high as 0.4. This is perhaps a surprising result, as time series

42

analysis at the 10-m level (Kral et al., 2021) showed that the surface layer routinely decoupled from the 10-m observations. These results indicate that the function fitting and analytical gradient calculations perform well, even if the magnitudes of the 10-m scaled turbulence are routinely larger than predicted. Further sensitivity studies on the method of calculating vertical gradients in the SBL are therefore warranted.

It is apparent from the eddy-covariance data that this gradient-based similarity framework is consistent with the results from Sorbjan (2010, 2017), including a general validation of the empirical relationships in Equation 2.11. In particular, the scaled 5-m eddy-covariance observations collapse nearly perfectly to these relationships. As discussed further in Section 2.6, this is likely related to having observational constraints above and below, whereas these constraints do not necessarily exist for the 2-m and 10-m eddy-covariance levels. With this in mind, the following section outlines the potential for extending these relationships into the new realm of in situ observations from UASs.

2.5   Applications to Uncrewed Aircraft Systems

The validation of the empirical gradient-based similarity equations in Section 2.4.2.2 now presents a unique opportunity to apply the algorithm in Equation 2.12 to calculate vertical profiles of turbulent parameters by measuring only temperature and wind speeds. These parameters are readily available by leveraging the vertical profiles from rotary-wing UAS flights conducted during the ISOBAR18 campaign. We first outline the necessary data-processing steps to appropriately perform these calculations before presenting three case studies from the campaign to highlight the utility of this method.

2.5.1 Uncrewed Aircraft System Data Processing

To ensure the highest data quality, post-processing UAS data requires considerations on how the aircraft behaves in its environment (Barbieri et al., 2019). The CopterSonde data used in this chapter are therefore processed in the following manner: After initial quality checking (i.e., range tests and spike removal), temperature, relative humidity, pressure, and attitude data are low-pass filtered applying the settings summarized in Table 2.2. These parameters were subjectively chosen to mitigate the effects of high-frequency aircraft oscillations when estimating the horizontal winds without affecting the phase of the signals and still maintaining information from time scales the temperature sensors can resolve. This filtering is essential towards improving the convergence of vertical gradient and especially Ri calculations, as high frequency noise and bias can severely reduce the physical representativeness of these calculations. Filtering the raw CopterSonde data should also improve the ability of singular profiles to represent the surrounding SBL flow in space and time. By oversampling at 10 Hz (Table 2.1, compared to the $1/\tau \approx 0.4$ Hz temperature response frequency as explained below), we implicitly are able to reduce errors due to aliasing, and do not apply any further anti-aliasing corrections.

Table 2.2: Quantitative description of the digital zero-phase finite impulse response low-pass filter utilized on the raw CopterSonde data. Calculations were performed using the Remez exchange algorithm (McClellan and Parks, 1973) available in the open-source SciPy Python library (Virtanen et al., 2020).

Parameter	Value
Sample frequency	10 Hz
Passband edge frequency	0.01 Hz
Stopband edge frequency	0.1 Hz
Number of taps	501

After low-pass filtering, the measurements from the temperature and humidity sensors are time-response corrected as outlined in Kral (2020), who was originally inspired by the work of Jonassen (2008) utilizing the fixed-wing Small Unmanned Meteorological Observer. This is a crucial step in processing, as errors in vertical profiles due to sensor lags can substantially impact the magnitude of observed temperature inversions and resulting profile shapes (Houston and Keeler, 2018). This method essentially involves a convolution of the time series data,

$$\psi_i^{rc} = \frac{\psi_i^{raw} - \left(\psi_{i-1}^{raw} e^{-\delta t/\tau}\right)}{1 - e^{-\delta t/\tau}}, \tag{2.17}$$

where ψ is an arbitrary discrete-time variable, the subscript i denotes an index of the digital signal, the superscripts rc and raw denote the response-corrected and raw time series data (respectively), $\delta t = t_i - t_{i-1}$ is the timestep between subsequent samples, and τ is the time constant of a first-order system (i.e., the sensor output can be modelled as a first-order differential equation of the input). We estimated τ of the iMet-XF thermistor, while integrated into the CopterSonde, through a series of step-function inputs between a sauna and the below-freezing environment on Hailuoto during the ISOBAR18 campaign. For reference, this value ranges from 2.5–2.7 s (the manufacturer did not supply a reference value, although this range is similar to those from other bead thermistors). Other methods of time constant estimation include: 1) rapidly ascending and descending through an inversion layer to simulate a step change (Kral, 2020); and 2) comparing pairs of ascent and descent profiles and iteratively testing values of τ until the root-mean-squared difference between the corrected pair of time series is minimized (Mahesh et al., 1997; Jonassen, 2008). It should also be noted that applying the low-pass filter described previously has an impact on the response times of the thermodynamic sensors. In testing, we found this difference to be less than

10%, which should be small enough to be offset by the slow (1 m s^{-1}) ascent rates and vertical altitude bin averaging when further processing the profiles. A successful reconstruction of the response-corrected signal (Equation 2.17) also depends on a relatively smooth input signal ψ^{raw}, as abrupt changes onset by sensor noise can result in non-physical enhancements of these changes (Jonassen, 2008). Although we do not present a validation of this method during ISOBAR18, Jonassen (2008) demonstrated substantial intra-flight sensor accuracy improvements (8–62.5% for temperature), and this correction method across multiple aircraft datasets in Kral et al. (2021) enabled considerable improvements in their comparisons. Herein, all calculations and analyses are performed using the low-pass-filtered and response-corrected measurements.

Since vertical gradients of atmospheric parameters are exceptionally large in this experiment, it is also crucial to assure accuracy in altitude estimations from the CopterSonde's autopilot. Autopilots typically use a standard atmospheric lapse rate of 6.5 K km^{-1} with a 15°C surface temperature at sea level to estimate altitude from pressure and global navigation satellite systems (GNSS), which is far from accurate in the Arctic SBL. Instead of relying on these estimates, hydrostatic balance is assumed so that altitude can be iteratively calculated using ambient air density as calculated from pressure and temperature observations (Barbieri et al., 2019):

$$z_i = z_{i-1} - \frac{\Delta p}{g\overline{\rho}}, \tag{2.18}$$

where z is the altitude, the subscript i denotes an index of the altitude array, $\overline{\rho}$ is the average density for a layer (i.e., $\overline{\rho} = \frac{1}{N}\sum_{j=0}^{N}\rho_j$ for all samples N between z_{i-1} and z_i), Δp is the change in pressure for a layer, and g is the acceleration due to gravity. From UAS data, we can estimate $\overline{\rho}$ from the ideal gas law: $\overline{\rho} = \overline{p}/(R_d\overline{T})$, where $\overline{p}$ is the geometric mean since p changes exponentially with height: $\overline{p} = (\prod_{j=0}^{N}p_j)^{1/N}$,

$R_d = 287.058$ J kg^{-1} K^{-1} is the specific heat capacity of dry air, and $\overline{T}$ the mean temperature of each layer. For the present chapter, we prescribe a constant Δp of 0.04 hPa to discriminate between subsequent layers as a trade-off between temperature sensor response time, barometer accuracy, and the CopterSonde's vertical ascent rate. Once the new array of altitudes is calculated, all remaining parameters are bin-averaged to match the same vertical spatial resolution (which correspondingly has an average time resolution of ~ 3 s).

After altitude post-processing, we then interpolate all parameters to a consistent time vector with a 0.25 s resolution to maintain a convenient gridded format for later analysis. At this stage, we compare the CopterSonde temperature and relative humidity measurements to the "slow-response" temperature sensors on the GFI2 mast to calculate and apply relative offsets for the duration of the campaign (Kral, 2020). Finally, horizontal winds are estimated using aircraft flight dynamics (see Segales et al., 2020) calibrated against the Doppler lidar present during the campaign (Kral et al., 2021).

At this stage, the differing characteristics of quasi-instantaneous UAS profiles and continuous time-averaged mast observations need some special attention. To address this issue, we choose to average data from multiple CopterSonde vertical profiles within 1-h windows, which typically correspond to three separate flights. We only consider CopterSonde data during the ascent portion of individual flights, because CopterSonde flight operations consisted of slower ascent and rapid descent to optimize battery usage and sensor response time versus averaging intervals. Moreover, the underlying assumptions for the kinematic model used to estimate horizontal winds are not valid when the aircraft is descending (for additional discussion on this decision, see Segales et al., 2020).

To facilitate this time averaging, and to ensure numerical stability in calculating vertical gradients, each processed profile is regridded in the vertical with a constant $dz = 5$ m before averaging across each altitude bin. These regridded profiles also have the advantage of reduced frequency response errors that may have resulted from the original observations, post-processing, and/or interpolating to a common time vector. From these time-averaged profiles, we calculate Ri and the gradient-based similarity scales from Equation 2.7 using first-order central finite differencing of potential temperature and horizontal wind components. When calculating Ri, we also follow Sorbjan and Balsley (2008) and sort potential temperature such that it is monotonically increasing throughout the profile. This method better represents the background state of the atmosphere if turbulence was allowed to relax adiabatically (Sorbjan and Balsley, 2008), and has the added benefit of returning positive values of Ri. Although Sorbjan and Balsley (2008) utilized this technique in the analysis of singular profiles of high-frequency measurements from a tethered lifting system in the SBL, we find it a worthwhile technique for our purposes as it further improves our ability to accurately compute vertical gradients from CopterSonde observations. As outlined in Section 2.2, turbulence parameters are then readily calculated by solving Equation 2.10 for the statistical moments and utilizing the gradient-based scales calculated from Equation 2.7 and the empirical dimensionless equations as a function of Ri in Equation 2.11.

2.5.2 Uncrewed Aircraft System Results

To examine the potential strengths and limitations of the gradient-based similarity framework applied to UAS data, we examine three case studies, each spanning 1 h and consisting of composites from 2–3 CopterSonde vertical profiles. These three cases cover a broad stability range including varying characteristics of near-surface temperature

inversion, differing characteristics of low-level jets (LLJs), and the presence of low-level internal gravity waves.

To evaluate the vertical limit for this scaling approach in the SBL we provide several estimates of the SBL height based on (1) vertical profiles of CopterSonde-observed temperature, wind speed, and wind direction; (2) Ri profiles as derived from the CopterSonde observations; and (3) sodar attenuated backscatter profiles. We estimate turbulence for the entire range of vertical observations since the SBL height is poorly defined in general and the applied metrics are not mutually consistent. Moreover, Sorbjan (2017) also emphasizes that incorporating the blended mixing length (Equation 2.8) into the gradient-based similarity framework theoretically extends its validity to any stably-stratified fluid.

For the cases presented, we also quantify ranges of uncertainties in Ri and turbulence estimations by calculating these parameters from each individual profile within the 1-h period. By overlaying these ranges with the estimates based on the mean profiles, we demonstrate how natural flow variability captured by a single vertical profile can occasionally result in non-physical ranges of turbulence estimates. To validate the in situ CopterSonde observations and resulting turbulence estimates, we also present comparisons of profiles from the mast, lidar, and sodar where appropriate. Note that we do not validate the vertical velocity standard deviation against the lidar due to high uncertainties related to observations based on a four-beam velocity azimuth display scanning technique and to the spatial averaging over varying measurement volumes with scanning altitude (Mann et al., 2010; Sathe et al., 2011; Sathe and Mann, 2013; Sathe et al., 2015). We instead present a comparison to the vertically oriented sodar based on time-domain averaging the 3 s noise-filtered w observations at each altitude. Although these resulting estimates of σ_w may be biased due to spectral losses, they

are more reliable than those from the lidar and provide one of our only CopterSonde validations above 10 m.

2.5.2.1   Case 1: 16 February 2018, 2100–2200 UTC

On the night of 16 February 2018, the atmosphere exhibited a three-layer thermal stratification within the lowest 300 m a.g.l. as observed by the CopterSonde (Figure 2.6a). A cloud layer around 400 m a.g.l. (more than 100 m above the maximum CopterSonde flight altitude) and continuous snow counteracted the surface-based longwave radiative cooling, resulting in a shallow neutrally stratified layer up to about 20 m a.g.l. The second layer ($\approx 20 - 100$ m a.g.l.) contained a ≈ 4 K temperature increase centered on an LLJ with a core velocity of 6 m s^{-1} at 70 m a.g.l. (Figure 2.6b). Above 300 m a.g.l., layer three appeared to be decoupled from the surface, as both temperature and wind speed decreased with height. In general, there is strong agreement between the CopterSonde, mast, and lidar observations of temperature, wind speed, and wind direction at all heights in both magnitude and profile shape. Moreover, both the mean profiles and ranges encountered in the 1-h timeframe also agree markedly well.

The CopterSonde-estimated Ri was $\mathcal{O}(10^{-1})$ near the surface and generally increased with height throughout layers 1 and 2 as thermal stratification became increasingly dominant with height until a local maxima in Ri around 70–90 m a.g.l. at and directly above the LLJ core (Figure 2.6c). In the topmost layer, Ri occasionally became > 1 as wind shear became small compared to the modest lapse rates. The presence of clouds and precipitation is also noted by the variability in individual Ri profiles, which span a decade or two at each altitude. Except for a few outlier points above 150 m a.g.l., the range from individual Ri profiles encompasses the mean Ri profile, which implies that the mean SBL flow is better represented by the time-averaged

50
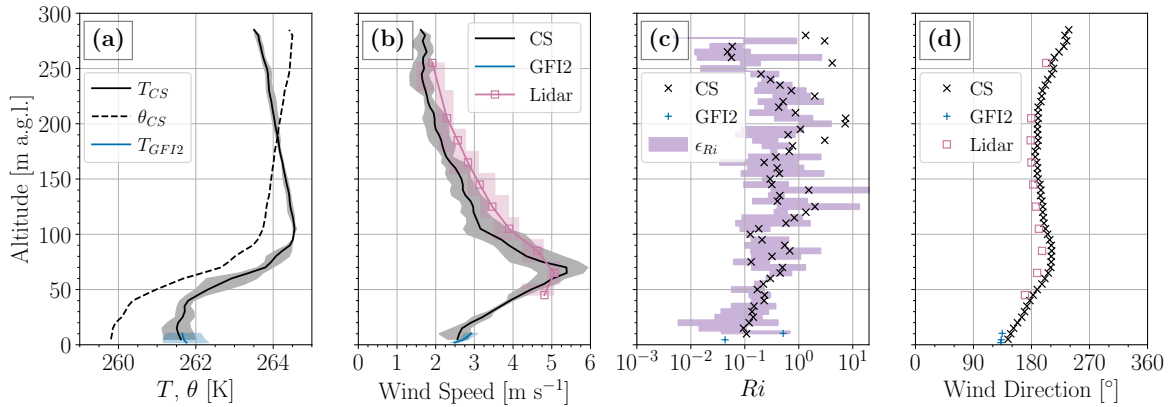
Figure 2.6: Composite profiles of (a) temperature (solid) and potential temperature (dashed), (b) wind speed, (c) gradient Richardson number in logarithmic coordinates, and (d) wind direction from 16 February 2018 between 21–22 UTC. For (a) and (b), the black solid lines represent the mean CopterSonde values at each height, and the grey shading in (a) and (b) envelopes the maximum and minimum values. The same convention is used for data from the GFI2 mast (blue lines) and the lidar (magenta lines). In (c), the black Xs denote Ri calculated using only the mean values of potential temperature and wind speed, with indigo shading denoting ϵ_{Ri}, the range of Ri as determined by the individual profiles. For clarity, only the mean wind directions are shown in (d).

Figure 2.7: Profile time series of attenuated backscatter, observed by the sodar for the period 2100–2200 UTC on 16 February 2018.

51
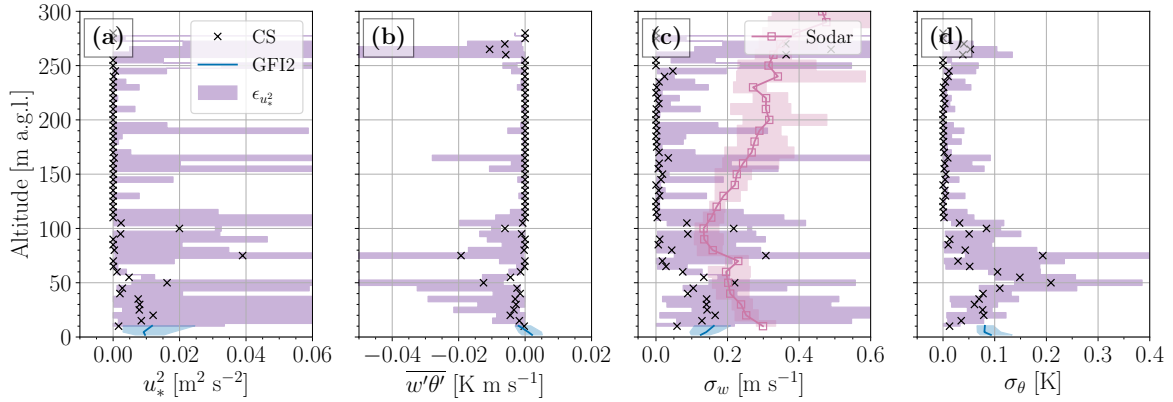
Figure 2.8: Vertical profiles of (a) kinematic momentum flux, (b) kinematic heat flux, (c) vertical velocity standard deviation σ_w, and (d) potential temperature standard deviation σ_θ calculated using the gradient-based similarity functions based on Copter-Sonde data (black Xs), and the range of observations from the GFI2 mast (blue lines and shading) and the sodar [magenta line and shading in (c)]. As in Figure 2.6c, the indigo shading in each represents the range of turbulence estimates ϵ when calculated from the individual profiles.

CopterSonde profiles. Also of note, most levels of the profile exhibited wind directions between 150–300° as specified for the eddy-covariance analysis in the previous section (Figure 2.6d), which ensures a high degree of horizontal homogeneity in the flow across sea ice.

The sodar echogram of this 1-h period (Figure 2.7) indicates a strong signal in a surface-bound layer, descending from about 70 m a.g.l. to 40 m a.g.l. over this time frame. Apart from this, the echogram does not reveal any other significant temporal changes (non-stationarities). Hence, the mean SBL height based on the sodar observations is estimated to 55 m, whereas the temperature, wind speed, and direction profiles indicate a slightly deeper SBL extending to an altitude of about 75 m. The first major peak in the Ri profile is detected at 125 m a.g.l., although there is also a minor peak indicating stronger stability at 85 m a.g.l. Note that it is not uncommon that different methods for estimating the SBL height are subject to discrepancies. One important aspect here is also the differences in temporal sampling and averaging, i.e., ensemble

averages of few quasi-instantaneous UAS observations and time averages of continuous sodar measurements.

By leveraging the empirical dimensionless similarity functions (Equation 2.11) in combination with the in situ CopterSonde observed gradient-based scales, the estimated turbulence profiles display several encouraging patterns (Figure 2.8). The lowest levels of CopterSonde-estimated momentum and heat fluxes (Figure 2.8a and b, respectively) match well with the GFI2 observations of the same parameters, both in magnitudes and profile shapes. The momentum (heat) flux generally increases (decreases) until reaching a maximum (minimum) around 40 m a.g.l., which aligns with the bases of the elevated temperature inversion and LLJ (Figure 2.6a and b, respectively). Between 45–55 m a.g.l., there is a peak in both momentum and heat flux, possibly corresponding to the elevated inversion interacting with turbulence in the neutral layer below. Aside from additional peaks at the core of the LLJ around 75 m a.g.l. and at the top of the elevated inversion around 100 m a.g.l., both momentum and heat flux is estimated to be near zero throughout the remainder of the profile.

Vertical velocity standard deviations σ_w display a similar qualitative structure (Figure 2.8c) as the momentum flux profile, with a maximum around 75 m a.g.l. and additional peaks around 50 and 100 m a.g.l. The magnitudes of the estimated σ_w values also agrees within an order of magnitude with the sodar-observed values below 100 m a.g.l. Although the CopterSonde σ_w estimates above 100 m a.g.l. are near-zero, the uncertainties from individual profiles are within the observed sodar ranges.

Potential temperature standard deviation σ_θ also demonstrates a similar pattern (Figure 2.8d), with near-surface values of σ_θ close to zero (as would be expected in neutral stratification), giving way to a broad peak of 0.2 K centered between 30–70 m a.g.l. This peak may be associated with the temporally evolving temperature inversion in this layer acting as a source for potential temperature variance (e.g., Wyngaard and

Coté, 1971). This pattern of σ_θ, along with the other turbulent parameters, outlines the importance of vertical wind shear associated with the LLJ in mixing the SBL, especially when located within the lowest 100 m a.g.l. and in the presence of strong temperature gradients.

2.5.2.2   Case 2: 18 February 2018, 1700–1800 UTC

Between 1700 and 1800 UTC on the evening of 18 February 2018, the CopterSonde observed a persistent considerable temperature inversion atop a surface-based weakly stable layer (Figure 2.9a), with a lapse rate of 21 K km^{-1} between 5 m and 85 m. In the 85–100 m layer, the average lapse rate increased to 147 K km^{-1}. Between 100 and 200 m, the atmosphere was nearly isothermal, and temperature decreased gradually above 200 m with an approximately dry adiabatic lapse rate. The presence of low-level clouds (around 300–400 m a.g.l.) during this period reduced the net radiation balance close to zero (not shown), thereby limiting the surface longwave cooling and resulting in a relatively weak surface-based inversion.

The wind speed profile (Figure 2.9b) increased from below 0.5 m s^{-1} near the surface to about 5 m s^{-1} at 200 m as measured by both the CopterSonde and lidar with a wide (± 1 m s^{-1}) variability between flights. This variability seems to be related to the elevated oscillations in sodar backscatter signal between 50–150 m a.g.l. and a period of 3–5 min (Figure 2.10; outlined below). While neither the CopterSonde or lidar perform exceptionally well at detecting wind speed at such low ambient flow velocities (for further discussion, see Bell et al., 2020), the general agreement between the two systems is consistent below 200 m. Above 200 m, the CopterSonde detected decreasing wind speeds with height, indicative of an LLJ core centered around 200 m, whereas the lidar showed further increase in wind speed at 255 m. This may also be related to
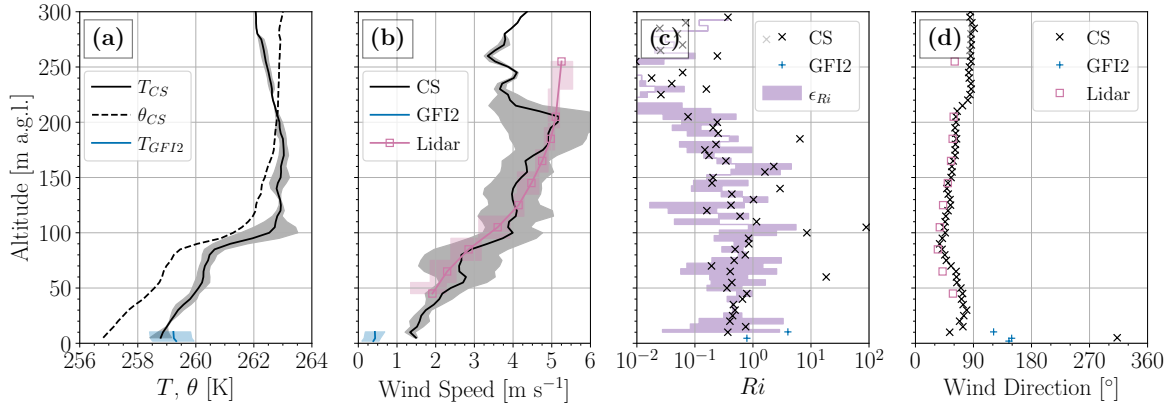
Figure 2.9: Same layout and conventions as Figure 2.6, but for 1700–1800 UTC on 18 February 2018.
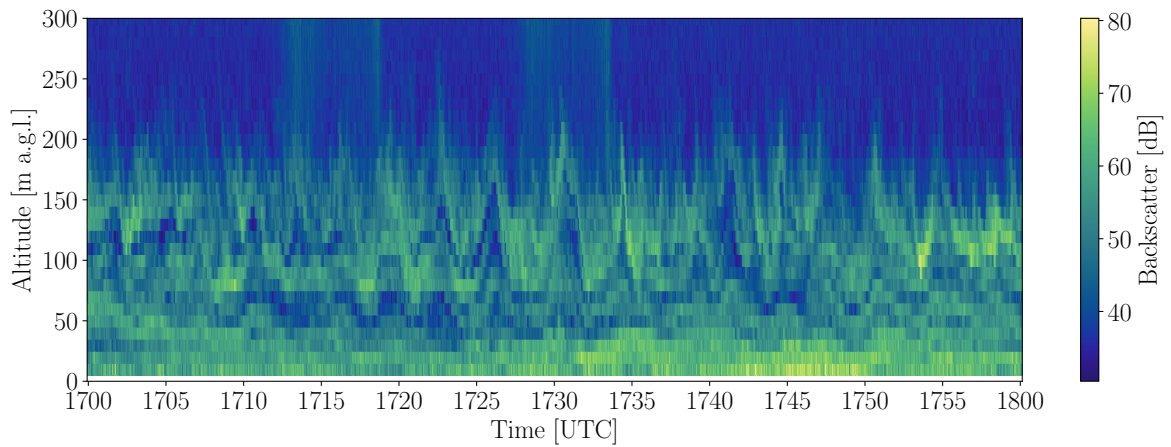
Figure 2.10: Profile time series of attenuated backscatter, observed by the sodar for the period 1700–1800 UTC on 18 February 2018.
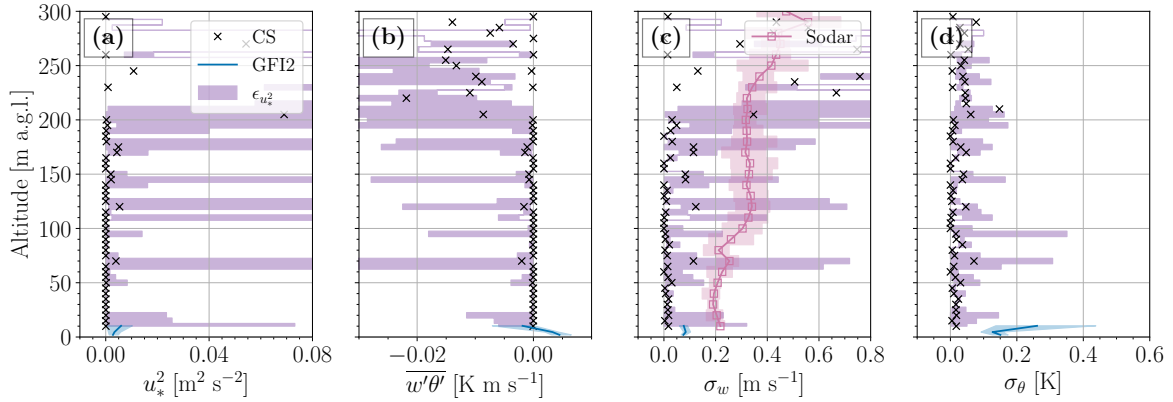
Figure 2.11: Same layout and conventions as Figure 2.8, but for 1700–1800 UTC on 18 February 2018.

only one CopterSonde flight reaching above 250 m a.g.l., as well as the elevated wave activity influencing the quasi-instantaneous lidar sample thereby creating an artificial LLJ signal.

Near-surface wind directions (Figure 2.9d) are subject to uncertainty both from the CopterSonde and GFI2 observations due to the low wind speeds, with a majority of samples indicating a south-easterly direction. Above 50 m, both the CopterSonde and lidar agreed that winds were primarily north-easterly. Although this direction implies an offshore flow, the forest and vegetation near the coast of the island were confined to below 50 m. This offshore flow likely also contributed to the weak inversion in the surface-based layer by advecting relatively warm air above the sea ice only an hour after local sunset.

The resulting average Ri profile during this time frame (Figure 2.9c) identifies a very stable ($0.12 < Ri < 0.7$) regime throughout the lowest 300 m of the atmosphere. Maxima of $Ri > 5$ are estimated to be centered around 60, 105, and 140 m, mostly coinciding with inflection points in the CopterSonde wind speed profiles.

The structure of the SBL during this 1-h period, as seen from the sodar echogram (Figure 2.10), appears more complex than during the previous case. A strong backscatter signal is detected in a layer below 50 m a.g.l. with an estimated average height of 35 m a.g.l. Above this layer we identify oscillating patterns between approximately 75 and 200 m a.g.l. with a period in the order of 2 min. This pattern is most likely associated with internal gravity waves ducted by the elevated inversion centered at 100 m a.g.l. The source of these waves is difficult to determine, but is possibly related to flow across the approximately 40 km diameter island of Hailuoto upstream of the observational site. For most of the time this layer appears to be clearly detached from the surface-based turbulent layer below. Based on this interpretation of two separate layers, we estimate the SBL height from the sodar to be 35 m. The vertical profiles of temperature, wind speed and direction suggest an SBL height of 80 m, which is in particular based on the wind direction profile, whereas considering the lowest peak in the Ri profile as the SBL height results in 60 m a.g.l.

As expected for considerable dynamic stability, CopterSonde momentum and heat flux estimates below 50 m a.g.l. are close to zero, which are in strong agreement with the GFI2 obervations (Figure 2.11a and b). Estimated fluxes imply enhanced vertical mixing around 70 m a.g.l., likely associated with a slight decrease in mean wind speed with height in the 60–70 m a.g.l. layer. Otherwise, turbulent fluxes were largely suppressed below 200 m a.g.l., possibly an artifact of temporally averaging profiles through mesoscale wave activity. Above 200 m a.g.l., the turbulence estimates are an order of magnitude larger, with considerably more scatter, and without validation it is not known whether these values are physical considering they are above the internal gravity wave signal.

Throughout the lowest 200 m a.g.l., σ_w was relatively small (< 0.2 m s^{-1}) but displayed several peaks coinciding with the momentum and heat flux profiles (Figure 2.11c). Only these peaks compare well in order of magnitude to the sodar observations, although the uncertainty bounds from individual profiles compare more closely. Also of note when comparing with the sodar is that the 10 m a.g.l. σ_w observations from the sodar are more than double that from the top GFI2 eddy-covariance level. Because of the non-stationarity of this case, it is plausible that the individual CopterSonde profiles may more realistically represent the SBL dynamics. There is also considerable variability in the σ_w estimates above 200 m a.g.l., likely due to the same reasons as described for the fluxes.

The σ_θ profile (Figure 2.11d) exhibits similar characteristics as the σ_w one, i.e., weak values of σ_θ (< 0.1 K) throughout the lowest 200 m a.g.l. with peaks located at inflection points of the temperature and wind speed profiles. Above 200 m a.g.l., there is also enhanced scatter in σ_θ, but rarely exceeding 0.1 K.

Although the meteorological set-up for this case was not necessarily horizontally homogeneous and statistically stationarity as required by the gradient-based scaling framework, the resulting turbulence estimates agreed reasonably well with observations being within 1–2 orders of magnitude.

2.5.2.3 Case 3: 18 February 2018, 2100–2200 UTC

This case took place 3 h after case 2 during the same IOP. The dissolution of low clouds around between these two cases (around 1900 UTC) enabled continuous longwave cooling, thereby strengthening the low-level stability. The near-surface temperature had cooled to about 254.5 K and increased to about 260.5 K at 50 m resulting in a mean lapse rate of 120 K km^{-1} in this layer (Figure 2.12a). This increased stability acted to suppress the wind speed within the SBL, resulting in weak (≈ 1 m s^{-1}) values

throughout the lowest 50 m a.g.l. (Figure 2.12b). There was considerable wind veer with height exceeding 180° in this layer (Figure 2.12d). Analysis of raw lidar data and individual CopterSonde profiles (not shown) indicates that the relative disagreement between instruments within this shear layer is likely related to temporal variability within the averaging period. This combination of strong lapse rates and constant wind speed with height yielded very stable to extremely stable conditions, as evidenced by $Ri > 0.7$ in the lowest 50 m (Figure 2.12c; Sorbjan and Grachev, 2010).

In the 50–100 m layer, the temperature increased by another 2.5 K on average whereas the wind speed increased by 3 m s^{-1} and the wind direction continued to veer (according to the CopterSonde) until reaching 60°, leading to a nearly constant $Ri \approx 0.5$ in this layer (Figure 2.12c). Above 100 m, the atmosphere was quasi-neutral with only a weak increase in potential temperature up to the top of the CopterSonde profile at 270 m. There was a maximum in wind speed between 120–160 m a.g.l., above which the wind speed decreased slowly with height, whereas the wind direction remained nearly constant around 60°. The Ri profile above 100 m a.g.l. also fluctuates between strongly stable and near-neutral, as both wind shear and lapse rates are relatively small.

The sodar echogram (Figure 2.13) for case 3 indicates a very shallow surface-based turbulent layer of roughly 20 m a.g.l. almost for the entire period. Only between 2145 and 2150 UTC is there some sign for turbulence in a slightly deeper layer. Clearly separated from this is an elevated layer with strong scattering properties, below 120 m a.g.l. with its lower limit decreasing from 80 m a.g.l. to 40 m a.g.l. This layer coincides with an elevated inversion and a strong wind speed gradient as seen from the CopterSonde profiles (Figure 2.12a and b). The signal is therefore likely to result from shear driven turbulence in a layer with relatively strong density gradients. The observed wind veer below 80 m a.g.l. (Figure 2.12d) suggests an SBL height in the range of 80 m a.g.l.,
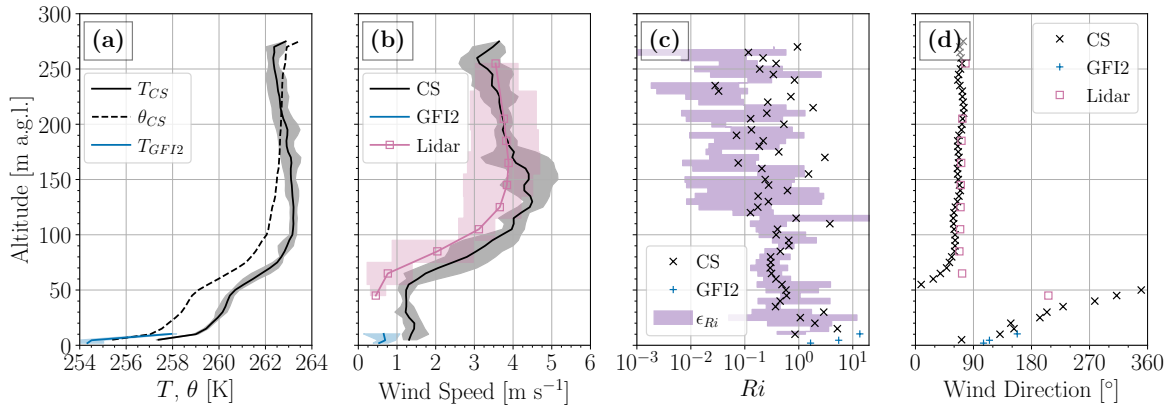
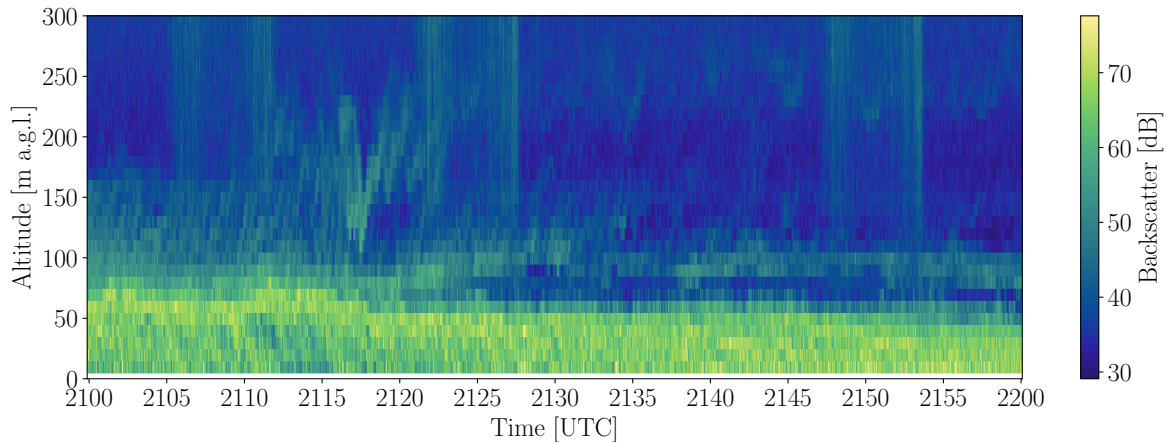Figure 2.12: Same layout and conventions as Figure 2.6, but for 2100–2200 UTC on 18 February 2018.
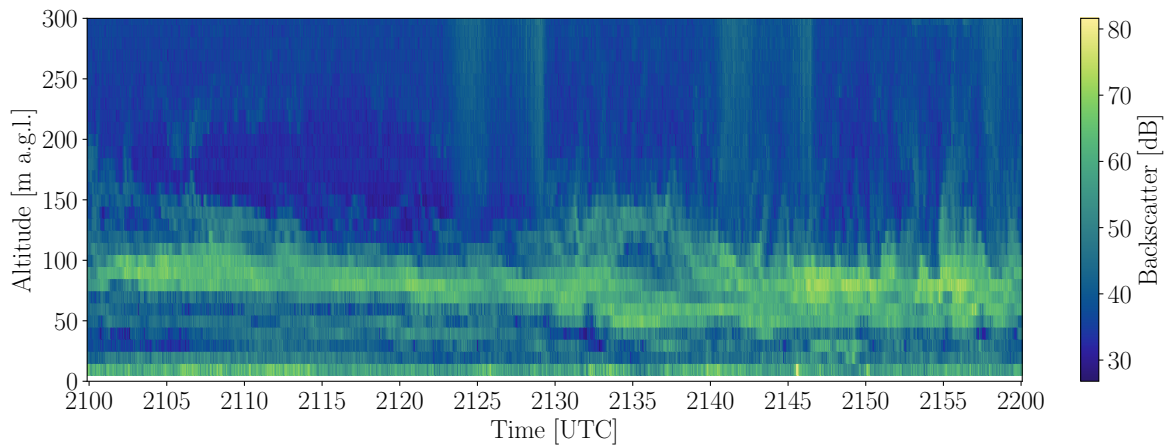
Figure 2.13: Profile time series of attenuated backscatter, observed by the sodar for the period 2100–2200 UTC on 18 February 2018.
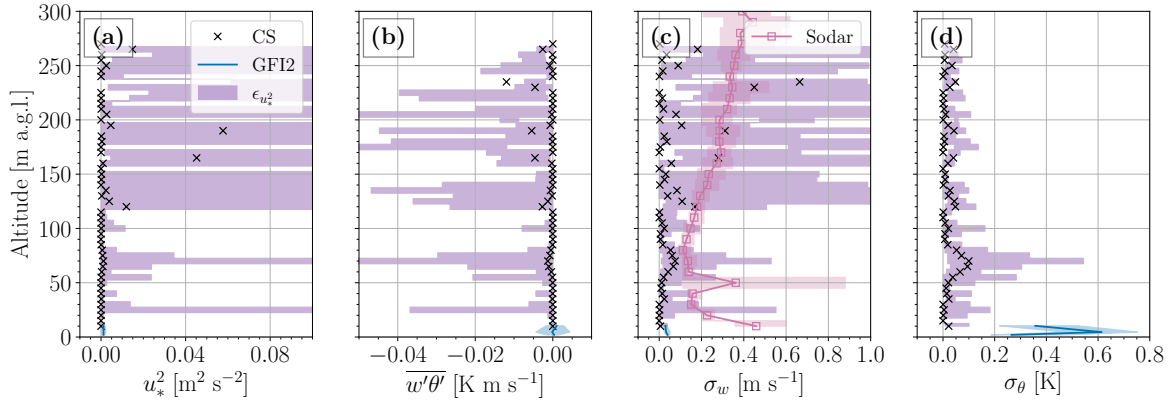
Figure 2.14: Same layout and conventions as Figure 2.8, but for 2100–2200 UTC on 18 February 2018.

which is also consistent with the vertical gradients of temperature and wind speed (Figure 2.12a and b). The Ri profile suggests an SBL height similar to the sodar estimate, with a first major peak at about 20 m a.g.l.

As with the case earlier on the night of 18 February 2018, exceptional near-surface stability suppressed most turbulent motions below 50 m a.g.l., as indicated by the GFI2 observations and CopterSonde estimates (Figure 2.14a and b). Coinciding with the relatively strong wind shear in the 50–100 m a.g.l. layer, the CopterSonde estimates of momentum and heat flux denoted peaks around 70 m related to the local minimum in Ri. Between 100–150 m a.g.l., there were also peaks in turbulence centered on the local maximum in wind speed.

The profiles of σ_w and σ_θ (Figure 2.14c and d, respectively) exhibit similar behaviors as the turbulent fluxes in the lowest 100 m a.g.l.. Of note, the near-surface standard deviation of vertical velocity, σ_w, is minimal, with reasonable agreement between the CopterSonde estimates and GFI2 observations in both magnitude and profile shape. The near-surface peaks in σ_θ observed by the GFI2 mast are likely related to mesoscale motions (see Figure 7a in Kral et al., 2021), however the CopterSonde estimates are still within an order of magnitude. Peaks in σ_w and σ_θ values were observed around

70 m a.g.l., around the base of the increase of wind speed with height but roughly 20 m higher than the peak in σ_w observed by the sodar. Above 100 m a.g.l., the σ_w and σ_θ profiles generally displayed more spread than the flux profiles, with fewer distinguishable patterns related to the potential temperature and wind speed profiles. The magnitudes of σ_w and σ_θ were, however, still in a physically reasonable range.

2.6   Discussion

In Section 2.4, we evaluated the empirical Businger–Dyer MOST formulations with eddy-covariance data during SBL flow across sea ice as a baseline to contextualize the performance of gradient-based SBL scales. Results from the application of MOST in Section 2.4.2.1 maintain the notion that self-correlation and poorly defined flux-based scales in strong stability limit the applicability of MOST. Moreover, considerable spread in the dimensionless sensible heat flux φ_h as a function of stability parameter $\zeta = z/\Lambda$ (Figure 2.3) highlights the overall inability of MOST to effectively portray the nature of weak and intermittent turbulence, thereby making the generalization of the MOST functions to other vertical profile data dubious.

The application of gradient-based scaling to the micro-meteorological mast data (Section 2.4.2.2, Figure 2.5) reveals several intricacies relating to the computation of vertical gradients. Scaled eddy-covariance observations from the middle level (5 m) generally performed better than from the top (10 m) and bottom (2 m) eddy-covariance levels. This is most likely a boundary condition problem: the 5-m eddy-covariance polynomial fit can be constrained by the 2-m and 10-m observations, with no need for extrapolation. Although we imposed a surface boundary condition of $U(z = z_0) = 0$ to better constrain the velocity profile at 2 m, the exact value of z_0 is not known and had to be estimated. The uncertainty in this estimate, however, can be assumed to be

insignificant compared to uncertainties in the other observation heights. Additionally, we do not make use of a corresponding surface skin temperature to constrain the near-surface temperature profile, since the determination of its value from, e.g., longwave radiation or ground heat flux data, has a high uncertainty (e.g., Simó et al., 2019). As for the 10-m level, there is no upper constraint for temperature or wind speed; moreover, the highest temperature observational level from the more precise thermocouples is located at 6.8 m (Table 2.1), meaning this temperature profile is extrapolated by more than 3 m to the 10-m eddy-covariance level. With these caveats in mind, all three eddy-covariance levels of scaled observations collapse to their expected empirical functions within an acceptable degree. We therefore consider this experiment a successful demonstration of the gradient-based similarity framework.

After demonstrating the efficacy of the gradient-based scaling framework outlined by Sorbjan (2010, 2017) with ISOBAR18 eddy-covariance data, we proceeded to examine their utility throughout the SBL. On the surface, it may appear that limiting rotary-wing UAS observations to mean thermodynamic and kinematic quantities may not be a viable way to directly study SBL turbulence. On the contrary, we show that accurate observations of potential temperature and wind speed by the UAS are enough to determine the gradient-based similarity scales. Therefore, it is possible to estimate vertical profiles of turbulent parameters without needing to collect high-frequency observations for long ($>$ 10 min) time periods at each level. In Section 2.5, three case studies highlighted the viability of this method in examining the complex structure of the Arctic SBL. The interpretation of the UAS profiles of mean, stability, and turbulence statistics is aided by making use of high-resolution eddy-covariance, Doppler lidar, and sodar backscatter data, which provide detailed additional information on the vertical structure of the lower atmosphere and the nature of relevant layers. Solid estimates of the SBL height are essential to set an upper limit for the applicability of

the gradient-based similarity approach, as it relies on the height above the surface, z, as a scaling parameter. The SBL length scale ℓ as defined in Equation 2.8 attempts to blend both the neutral limit with the z-less scaling regime via an inverse sum such that $1/\ell = 1/\kappa z + 1/\lambda_0 + Ri^{3/2}/c$. The validity of this approach has been the subject of numerous investigations (e.g., van de Wiel et al., 2008; Huang et al., 2013; Sorbjan, 2017, and references therein), although it remains unclear how the present definition may impact the estimated turbulent moments near the top of the SBL far away from the surface or under strong stratification. In this chapter, we estimated SBL height from a combination of sodar echograms, the UAS mean temperature and wind profiles, and the derived UAS Ri profiles. Sorbjan (2017) argues that this definition of ℓ is valid for any stably-stratified flow, so an SBL depth based on the potential temperature lapse rate may suffice for these purposes. In the presence of an LLJ or internal gravity waves that locally produce turbulence regardless of height above the surface, the use of z as a scaling parameter deserves further investigation to improve the generality of this similarity framework.

One disadvantage of this gradient-based scaling framework is the inability to extract information on the sign of momentum fluxes, especially in the presence of decreasing wind speed with height above a LLJ core. The way we calculate vertical wind shear in Equation 2.9 results in positive-definite values, and the master scaling functions are only valid for $Ri > 0$ to produce positive values of u_*^2. This is an important consideration for the application of this flux estimation method, and further efforts to objectively recover the signs of, e.g., the fluxes $\overline{u'w'}, \overline{v'w'}$ should be pursued.

While this gradient-based similarity approach also depends on the assumption of horizontal homogeneity, results from these case studies indicate reasonable validity of the turbulence profiles when compared to the tower and lidar observations regardless of ambient flow direction. Although the ISOBAR18 campaign took place over sea ice,

the surface snow cover and ice conditions, along with variable amounts of cloud cover and precipitation throughout the campaign, undoubtedly impacted these results. Flow heterogeneity manifested in the GFI2 eddy-covariance scaling as scatter in the nondimensional turbulent moments even after accounting for flow direction but ultimately these results were in good agreement with the empirical predictions. This is encouraging especially given that 1) to perfectly control for homogeneity would require a multi-year long campaign and 2) these conditions more closely match other real-world applications in typical SBL flows. The sodar echogram from the UAS case 2 indicated modulation of the atmosphere by an internal gravity wave, the fine-scale details of which were likely lost through temporal averaging of the CopterSonde profiles. In this particular case, the individual profiles may potentially be more representative of the turbulent structure of the atmosphere, although without proper validation this is difficult to determine. Further studies with additional profiles for a given time period and eddy-covariance systems mounted higher than in the ISOBAR18 campaign (e.g., > 50 m a.g.l.) will be necessary to determine a framework for appropriate averaging to converge on physically representative statistics. Coupling observations with high-resolution simulations could additionally be used to examine the impact of internal gravity waves, heterogeneous surface covers, and canopy characteristics on modifying the turbulent structure of the SBL.

Chapter 3

Random Errors in the Stable Boundary Layer: Implications for Modern Observational Techniques

3.1 Research Objectives

In this chapter, we leverage a suite of large eddy simulations to estimate the random errors for various first- and second-order turbulence moments at typical averaging periods along with emulated observations by UAS and eddy-covariance systems within the SBL to answer the following key questions:

3. How do random errors depend on atmospheric stability and measurement height for various first- and second-order turbulence moments?

4. How well do emulated UAS and eddy-covariance measurements represent the ensemble mean?

5. What considerations are necessary to mitigate random errors for observations in the SBL?

This chapter is organized as follows: we provide the background theory for and methods to estimate random errors in stochastic signals in Section 3.2. In Section 3.3 we describe our LES code as well as the parameter space of simulations conducted. We then provide an overview for how we adapted existing methods for random error estimation for use with volumetric LES output in Section 3.4 and present results in

Section 3.5. A discussion on the significance of these results is presented in Section 3.6 before a summary and concluding remarks in Section 5.1.2.

3.2 Estimating Random Errors with the Relaxed Filtering Method

As discussed previously, random errors emerge when a timeseries is not averaged long enough for the time mean to converge sufficiently to the true ensemble mean via the ergodic hypothesis (Lumley and Panofsky, 1964; Sreenivasan et al., 1978; Mann and Lenschow, 1994; Lenschow et al., 1994). For a given random variable f, we are therefore interested in the ability of its temporal mean $\overline{f}$ to approximate the ensemble mean $\langle f \rangle$. Herein we define temporal averaging with an overbar $\overline{(\cdot)}$ and ensemble averaging with brackets $\langle \cdot \rangle$. Lumley and Panofsky (1964) describe the random error of f in terms of its error variance $\sigma_{\overline{f}}^2$ over an averaging period T

$$\sigma_{\overline{f}}^2(T) = \left\langle \left[\frac{1}{T} \int_{t_0-T/2}^{t_0+T/2} f(t)\mathrm{d}t - \langle f \rangle \right]^2 \right\rangle = \left\langle \left[\overline{f} - \langle f \rangle \right]^2 \right\rangle. \tag{3.1}$$

They further show that by assuming statistical stationarity, the error variance of f can be related to its integral time scale $\mathcal{T}_f$ as

$$\sigma_{\overline{f}}^2(T) = \frac{\langle f'^2 \rangle}{N} = \frac{2\mathcal{T}_f \langle f'^2 \rangle}{T}, \tag{3.2}$$

where $\langle f'^2 \rangle = \left\langle [f - \langle f \rangle]^2 \right\rangle$ is the ensemble variance of f and $N = T/(2\mathcal{T}_f)$ is the number of independent samples. It is then possible to define a relative error by normalizing the error standard deviation by the ensemble mean, $\epsilon_f = \sigma_{\overline{f}}/|\langle f \rangle|$, which yields

$$\epsilon_f = \left[\frac{2\mathcal{T}_f \langle f'^2 \rangle}{\langle f \rangle^2 T} \right]^{1/2}. \tag{3.3}$$

67

A major drawback of using Equation 3.3 to calculate relative random errors stems from the difficulty in computing the integral timescale $\mathcal{T}_f$ (if it exists at all; see discussion in Dias et al., 2004). In general, the integral timescale of f can be defined as

$$\mathcal{T}_f = \int_0^\infty \rho(\tau) \mathrm{d}\tau, \tag{3.4}$$

where $\rho(\tau)$ is the autocorrelation function of f as a function of lag τ, which is defined as

$$\rho(\tau) = \frac{\langle [f(t) - \langle f \rangle][f(t+\tau) - \langle f \rangle] \rangle}{\langle f'^2 \rangle}. \tag{3.5}$$

To use Equation 3.4 for computing the integral timescale for any real signal, one must impose an upper bound of integration. This upper bound may be arbitrarily large, but common choices include the first zero crossing of $\rho(\tau)$ (e.g., Sreenivasan et al., 1978; Lenschow et al., 1994; Salesky et al., 2012), when $\rho(\tau) = e^{-1}$, or at the minimum point of the autocorrelation (Tritton, 1988; Theunissen et al., 2008). Moreover, it is possible to assume an exponential form of the autocorrelation function (Lenschow et al., 1994; Kaimal and Finnigan, 1994; Sullivan et al., 2003) or fit a lag-window function (Dias et al., 2004) in order to compute the integral. Ultimately, the computed value of $\mathcal{T}_f$ is highly sensitive to the choice of integration method, which may not necessarily converge implying the nonexistence of the integral timescale. In addition to these computational difficulties, a physical constraint on accurately calculating an integral timescale depends heavily on the assumption of stationarity in the timeseries itself. A nonstationary process may possess an autocorrelation function that does not converge towards zero, which would result in an unbounded integral scale. Statistical preprocessing techniques

such as linear detrending may mitigate the effects of nonstationarity in windows of ≈ 1 hr, but is not always guaranteed.

It is therefore apparent that one's ability to determine relative random errors is impeded by the difficulty in accurately calculating integral time- and lengthscales. To circumvent these difficulties, Finkelstein and Sims (2001) introduced a statistical method for calculating the variance of a covariance that is based on a sample's auto and cross covariance functions. While shown to be effective for observational timeseries data across a wide range of environments, this method is only suited for estimating the relative random errors in second-order turbulence moments. Additionally, Salesky et al. (2012) proposed the so-called filtering method, which uses a spatially-local flux decomposition to recover a power-law fit for the error variance of any parameter as a function of averaging time (or averaging length in the case of spatial filters). The premise is based on the commutative nature of linear filters, which requires that the vertical flux $\overline{w'c'}$ of some quantity c averaged over length L is equivalent to an average of separately filtered fluxes $\widetilde{w'c'}$ (Sagaut, 2006; Salesky et al., 2012). Using this commutative property, the standard deviation of the local flux $\widetilde{w'c'}$, $\sigma_{\widetilde{w'c'}}$, can be related to the filter width Δ via a power law of the form

$$\sigma_{\widetilde{w'c'}}(\Delta) = C_{wc}\Delta^{-1/2}, \tag{3.6}$$

where the coefficient C_{wc} is determined via least-squares. The relative random error of the flux for any given averaging length L can therefore be determined without *a priori* knowledge of the integral lengthscale by evaluating Equation 3.6 at $\Delta = L$ and normalizing by the mean flux as

$$\epsilon_{wc} = \frac{\sigma_{\widetilde{w'c'}}(L)}{\langle w'c' \rangle}. \tag{3.7}$$

If desired, it is then possible to recover the integral scale *a posteriori* through a combination of Eqs. 3.6 and 3.2.

Dias et al. (2018) later expanded upon the work by Salesky et al. (2012) by acknowledging that fixing the $-1/2$ exponent in Equation 3.6 still implies the existence of an integral lengthscale. They argued that for a wide variety of real-world applications, Hurst's phenomenon of long-term persistence (Hurst, 1951; O'Connell et al., 2016) will cause this exponent to deviate from $-1/2$ and that a more general approach may be more appropriate. By letting this exponent vary freely, Dias et al. (2018) proposed a relaxed filtering method (RFM) that is capable of determining error statistics even when an integral scale does not exist. The RFM thus relies on a generalized form of Equation 3.6, which takes the form

$$\sigma_{\widetilde{w'c'}}(\Delta) = C_{wc}\Delta^{-p/2}, \tag{3.8}$$

where the exponent p is allowed to vary freely and can be determined through least-squares regression. In this framework, Dias et al. (2018) showed analytically that $0 < p < 1$ are evidence for Hurst's phenomenon in a stochastic process. Dias et al. (2018) also noted that the errors estimated by the RFM generally are higher than those from the method of Lumley and Panofsky (1964) in Equation 3.3 due to accounting for the presence of Hurst's phenomenon. Moreover, as Equation 3.3 directly requires that the exponent $p = 1$ in Equation 3.8, error estimates from the RFM may not necessarily enable one to calculate an integral lengthscale *a posteriori* as in Salesky et al. (2012). Readers are directed to the works of Salesky et al. (2012) and Dias et al. (2018) for the mathematical justification for this technique. Although we present the general premise for the RFM in terms of second-order turbulent moments in Eqs. 3.6–3.8, this technique is valid in estimating relative random errors in turbulence moments

of any order including, for example, the mean velocity or potential temperature. We further expand upon the implementation of the RFM using LES volumetric output in Section 3.4.

3.3 Large-Eddy Simulations

3.3.1 Code Description

We utilize LES code based on Albertson and Parlange (1999) and Kumar et al. (2006), which solves the filtered rotational form of the incompressible Navier-Stokes equations for momentum and potential temperature, respectively:

$$\frac{\partial \widetilde{u}_i}{\partial t} + \widetilde{u}_j \left(\frac{\partial \widetilde{u}_i}{\partial x_j} - \frac{\partial \widetilde{u}_j}{\partial x_i} \right) = -\frac{1}{\rho} \frac{\partial \widetilde{p}^*}{\partial x_i} + g \left(\frac{\widetilde{\theta} - \langle \widetilde{\theta} \rangle_{xy}}{\langle \widetilde{\theta} \rangle_{xy}} \right) \delta_{i3} - \frac{\partial \tau_{ij}}{\partial x_j}$$
$$+ f(\widetilde{u}_2 - V_g)\delta_{i1} - f(\widetilde{u}_1 - U_g)\delta_{i2}, \tag{3.9}$$

$$\frac{\partial \widetilde{\theta}}{\partial t} + \widetilde{u}_j \frac{\partial \widetilde{\theta}}{\partial x_j} = -\frac{\partial \pi_j^\theta}{\partial x_j}. \tag{3.10}$$

In this context, the tilde denotes a filtered quantity, $\widetilde{u}_i$ denotes the filtered velocity vector with $i = 1, 2, 3$ representing streamwise, spanwise, and wall-normal components (respectively), $\widetilde{p}^* = \widetilde{p} + \frac{1}{2}\rho\widetilde{u}_i^2$ is the modified pressure, θ is potential temperature, δ_{ij} is the Kronecker delta, $\tau_{ij} = \widetilde{u_i u_j} - \widetilde{u}_i \widetilde{u}_j$ is the SGS stress tensor, $\pi_j^\theta = \widetilde{\theta u_j} - \widetilde{\theta}\widetilde{u}_j$ is the SGS potential temperature flux, (U_g, V_g) are the geostrophic wind components, and $g = 9.81$ m s^{-1} is the acceleration due to gravity. Brackets with the subscript xy denote horizontal planar averaging. Spatial derivatives are calculated pseudospectrally in the horizontal plane and via second-order centered finite differencing in the vertical, and the second-order Adams-Bashforth method is utilized for time integration. The subgrid-scale (SGS) model is based on the Lagrangian-averaged scale dependent model

described by Bou-Zeid et al. (2005), and the wall model is based on Monin-Obukhov similarity theory (MOST; Monin and Obukhov, 1954) applied locally with test filtering at a scale twice the grid spacing to improve average stress profiles (Bou-Zeid et al., 2005). For simulating the SBL, we prescribe a surface temperature with a constant cooling rate as the lower boundary condition. The upper boundary condition is stress-free and impenetrable, and a sponge layer is applied in the upper 25% of the domain after Nieuwstadt et al. (1993). The LES code is parallelized in horizontal (xy) slabs using message passing interface (MPI; Aoyama and Nakano, 1999).

3.3.2 Cases

To simulate the SBL with LES, we impose a lower boundary condition as a prescribed constant cooling rate $C_r = -\partial\langle\theta_0\rangle/\partial t$ at the surface coupled with a wall model to determine surface heat fluxes (e.g., Basu et al., 2008; Gibbs et al., 2015). Here we simulate a series of six idealized SBL cases A–F after those by Huang and Bou-Zeid (2013), which were in turn based on those by Kosović and Curry (2000) (Table 3.1). Kosović and Curry (2000) originally utilized constant surface cooling rates based on observations from the Beaufort Sea Arctic Stratus Experiment and has been the inspiration for numerous other SBL studies using LES (e.g., Beare et al., 2006; Sullivan et al., 2016; Maronga et al., 2020; Stoll et al., 2020, and references therein). The six cases presented by Huang and Bou-Zeid (2013) vary only in their prescribed values of C_r, and as such were easily adapted for our purposes.

Our simulated domain was fixed at $(L_x, L_y, L_z) = (800, 800, 400)$ m with a horizontally homogeneous land surface of aerodynamic roughness length $z_0 = 0.1$ m. The domain size is sufficiently large relative to the integral lengthscales ($L_x \approx 10\mathcal{L}$) so that our results are not expected to be influenced significantly by the periodic boundary

Table 3.1: Mean simulation properties for cases A–F averaged over the last physical hour of the simulation, including: the surface cooling rate C_r, SBL height h, surface friction velocity u_{*0}, surface potential temperature scale θ_{*0}, Obukhov length L, global stability h/L, ratio of LLJ to SBL depth z_j/h, bulk SBL inversion strength $\Delta\langle\theta\rangle/\Delta z$, eddy turnover period T_L, and number of large-eddy turnover times nT_L.

Case	C_r	h	u_{*0}	θ_{*0}	L	h/L	z_j/h	$\Delta\langle\theta\rangle/\Delta z$	$T_L = h/u_{*0}$	nT_L
	(K h⁻¹)	(m)	(m s⁻¹)	(K)	(m)	-	-	(K km⁻¹)	(s)	-
A	0.25	160	0.231	0.0383	93.5	1.71	0.976	10.2	692	5.2
B	0.5	135	0.211	0.0658	45.1	3.00	0.935	24.1	642	5.6
C	1.0	107	0.190	0.112	21.1	5.07	0.911	59.7	563	6.4
D	1.5	93.7	0.180	0.157	13.3	7.05	0.928	101	521	6.9
E	2.0	87.1	0.172	0.198	9,51	9.16	0.926	147	506	7.1
F	2.5	80.5	0.166	0.236	7.28	11.1	0.924	198	485	7.4

conditions employed in the horizontal directions. In our code, the roughness lengths for momentum and heat, z_{0m} and z_{0h}, are chosen to be equal for consistency with previous studies. We imposed a constant geostrophic wind of $U_g = 8$ m s^{-1} along with a Coriolis parameter of $f = 1.318 \times 10^{-4}$ s^{-1} corresponding to a latitude of 65°N. The initial temperature profile (including the surface) was set to a constant 265 K up to a height of $z = 100$ m, above which the temperature increased with a constant inversion strength $\partial\theta/\partial z = 0.01$ K m^{-1}.

Due to computational expense, we initialize and run each simulated case on a domain with $n = n_x \times n_y \times n_z = 96^3$ total grid points for six hours of physical time before interpolating to a grid with $n = 192^3$ grid points and simulating for four more hours. At the higher resolution, this equates to a grid spacing of $\Delta_f = (\Delta_x \Delta_y \Delta_z)^{1/3} = 3.31$ m. This resolution was selected after performing grid convergence tests with $n \in \{96^3, 128^3, 160^3, 192^3\}$ (see Appendix 1). Our timestep Δ_t was set to a constant 0.04 s during the spinup simulations, which was then decreased to a value of 0.02 s in each of the interpolated cases for numerical stability. Ensemble means are calculated by averaging in horizontal planes and in time over the last hour of simulation (i.e., $\langle\rangle = \langle\rangle_{xyt}$), which corresponds to 5.4–7.7 large-eddy turnover times ($T_L = h/u_{*0}$, Table 3.1) and is consistent with other idealized investigations of the SBL (e.g., Huang and Bou-Zeid, 2013; Sullivan et al., 2016; van der Linden et al., 2019; Maronga and Li, 2021). Additional analysis of timeseries output of numerous simulated parameters as well as SBL depth and Obukhov length indicate this final hour is quasi-stationary (not shown). To further improve statistical convergence when calculating second-order turbulent parameters, all first-order fields are linearly detrended in time.

Bulk properties from the six simulations are summarized in Table 3.1. We determine the SBL height h after the mean stress profile technique by Beare et al. (2006): h is the height where the mean stress u_*^2 first falls to less than 5% of its surface value of u_{*0}^2

and divided by 0.95. With this definition we ensure the majority of turbulent motions are contained within the SBL. In this framework,

$$u_*^2 = \left(\langle u'w'\rangle^2 + \langle v'w'\rangle^2\right)^{1/2} \tag{3.11}$$

represents the magnitude of the vertical kinematic momentum flux, and the subscript 0 denotes the value of a quantity at the lowest grid level. The Obukhov length $L = u_{*0}^2\langle\theta_0\rangle/\kappa g\theta_{*0}$ depends on the von Kármán constant $\kappa = 0.4$, and the potential temperature scale $\theta_* = -\langle\theta'w'\rangle/u_*$. The height of the low-level jet (LLJ) is denoted as z_j, and we estimate a bulk SBL inversion strength using the top and bottom grid points within the SBL: $\Delta\langle\theta\rangle/\Delta z = \left(\langle\theta(z = h)\rangle - \langle\theta(z = \Delta_z/2)\rangle\right)/(h - \Delta_z/2)$.

For each of these cases, we consider both mean profiles as well as emulated observations from UAS and eddy-covariance vertical profiles. The emulated UAS and eddy-covariance profiles are derived from a virtual tower similar to that described by Salesky and Anderson (2018): it is located at $(x, y) = (L_x/2, L_y/2)$ and outputs a timeseries of each of the simulated parameters at every gridpoint in the vertical and at every simulated timestep (recall that $\Delta_t = 0.02$ s), yielding data with dimensions of height and time (Figure 3.1a). By assuming a constant UAS ascent rate, we can determine a timeseries of its corresponding vertical coordinates, which we then match and subsample from interpolated virtual tower data (Figure 3.1b). We then average the resulting one-dimensional timeseries in the same way as is customary for true UAS data (e.g., Pillar-Little et al., 2021; Greene et al., 2022) to obtain an emulated UAS profile with a constant vertical resolution (Figure 3.1c).

In this analysis we utilize averaging times of 3 s and 30 min for first- and second-order moments, respectively. These times were chosen with regard to typical averaging timescales when operating a UAS (3 s) or eddy-covariance system (30 min). Within
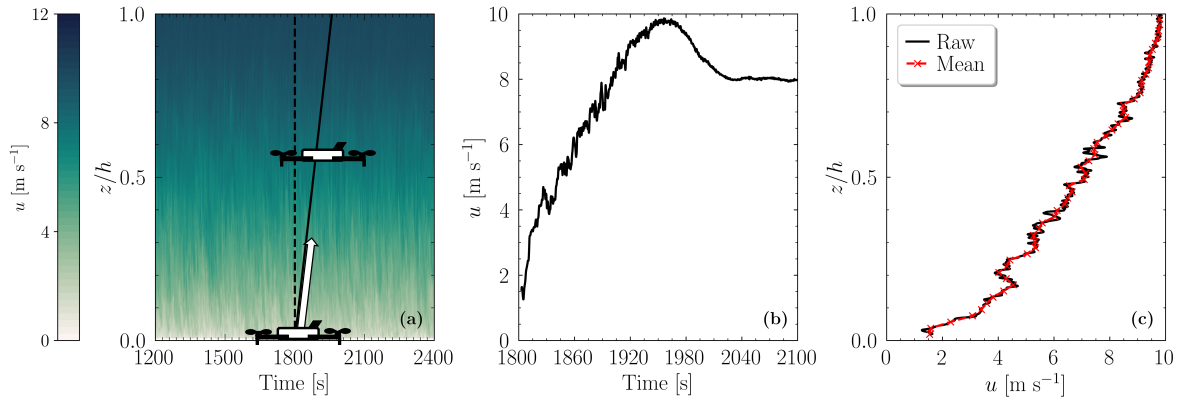
Figure 3.1: (a) Emulated trajectory of a rotary-wing UAS ascending at a constant rate of 1 m s^{-1} (solid line) and an instantaneous trajectory (dashed line) overlaid upon a time-height cross-section of u from a virtual tower in the center of the LES domain (b) timeseries of u velocity sampled by the virtual UAS (c) resulting vertical profile of wind speed in its raw state (black) and averaged into 3 m vertical bins (red).

the SBL it is common for a rotary-wing UAS to ascend at approximately 1 m s^{-1} and to post-process the data into altitude bins 3 m high, which corresponds to an averaging time of about 3 s (e.g., Greene et al., 2022). In general, UAS data is processed with emphasis on the resulting vertical resolution instead of the averaging time for each vertical bin. Vertical ascent rates from UAS are also typically chosen to optimize the aircraft's ability to reach a targeted maximum height with regards for sensor response times. It is also common practice to average over blocks varying from 10–60 min when calculating turbulence moments from mast-mounted eddy-covariance systems within the SBL. Thus, we chose the 30-min averaging time as representative of a typical application.
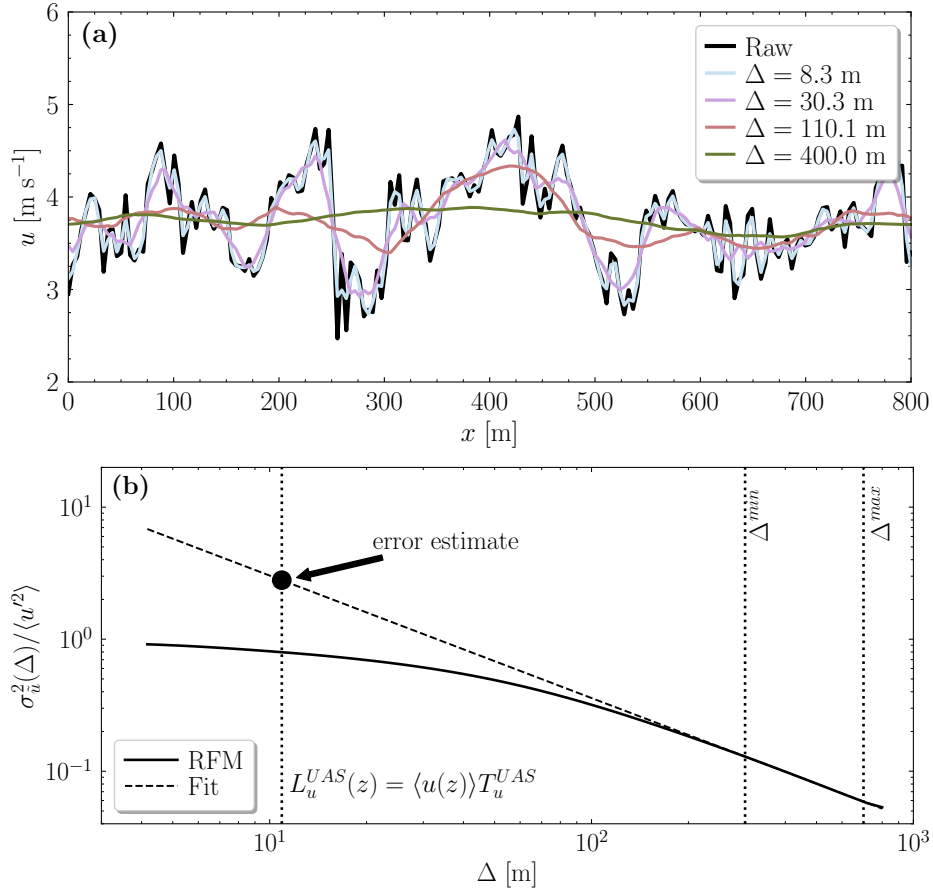
Figure 3.2: Graphic demonstration of the relaxed filtering method applied to volumetric LES data. (a) Raw u versus streamwise distance x from case A centered spanwise in the domain and at a height of $z/h = 0.14$ (black) overlaid with iterations of the signal filtered at varying scales Δ. (b) y- and time-averaged variances of u as a function of filter scale Δ (RFM, solid curve) to which Equation 3.8 is fit between Δ^{min} and Δ^{max} (Fit, dashed line); adapted from Figure 2 in Salesky et al. (2012). An error estimate for a UAS sampling timescale T_u^{UAS} can then be extracted from the power law.

3.4 Relaxed Filtering Method Applied to Large-Eddy Simulation Output

In this section we describe how we adapted the relaxed filtering method algorithm from timeseries output analyzed in Salesky et al. (2012) and Dias et al. (2018) for use with volumetric data generated by LES. We implement the RFM for a given variable $f = f(x, y, z, t)$ by first calculating its error variance through the following steps:

1. Isolate a "pencil" slice of f along the streamwise (x) dimension at a constant value of y, z, t (Figure 3.2a, black curve).

2. Apply an idealized tophat filter spatially with filter width Δ (Figure 3.2a, colored curves).

3. Calculate the variance of the filtered signal, $\sigma_{\tilde{f}}^2$.

4. Repeat steps 2 and 3 using 50 different filter widths spaced logarithmically such that $\Delta \in [\Delta_x, L_x]$ to attain $\sigma_{\tilde{f}}^2(\Delta)$.

5. Repeat steps 1–4 for all y, z, and t in the final physical hour of simulation.

6. Average the variances in y and t to finally obtain a two-dimensional error variance that is a function of both filter width and height: $\sigma_{\tilde{f}}^2 = \sigma_{\tilde{f}}^2(\Delta, z)$.

An example of steps 1–6 is presented in Figure 3.2a for $f = u$, which includes the resulting spatial distributions after 4 levels of filtering. Calculating error variance along x followed by averaging in y and t method can be interpreted as averaging a row of instrumented towers spanning the y-direction individually measuring the streamwise flow. Variations on this technique (e.g., filtering in both x and y and averaging only in t) are beyond the scope of this chapter, but the horizontal homogeneity of the simulations would likely lead to similar conclusions as this chapter.

78

After calculating the error variance for a given parameter, the remaining procedure to estimate its corresponding relative random error for a desired sampling time closely resembles that from Salesky et al. (2012):

7. For a given z, normalize the error variance by its corresponding ensemble variance $\langle f'^2 \rangle$ (Figure 3.2b, solid curve).

8. Select a range of filter widths to isolate the normalized error variance (Figure 3.2b, Δ^{min} and Δ^{max}).

9. Fit a function of the form $\sigma_{\tilde{f}}^2/\langle f'^2 \rangle = C_f \Delta^{-p}$ (similar to Equation 3.8 except utilizing the error variance instead of standard deviation) within the window selected in step 8 (Figure 3.2b, dashed line).

10. Estimate the relative random error of f for a desired sampling time T by converting to a length L through Taylor's hypothesis and substituting into the empirical power law for normalized error variance obtained in the previous step (Figure 3.2b, black dot).

11. Repeat steps 7–10 for all heights to obtain $\sigma_{\tilde{f}}^2(L, z)/\langle f'^2(z) \rangle$.

12. Finally, compute the relative random error $\epsilon_f(L, z) = \sigma_{\tilde{f}}(L, z)/\langle f(z) \rangle$ using the corresponding ensemble mean.

Note that in step 8 we choose the window of 300–700 m to fit the power law, which corresponds closely to the $\mathcal{O}(10\text{–}100 \text{ s})$ denoted by Salesky et al. (2012) when invoking Taylor's hypothesis. This power law is theoretically valid for extrapolation to any scale Δ, as seen in Figure 3.2b for a UAS sampling scale L_u^{UAS} that happens to be within the range $[\Delta_x, L_x]$ where the error variance has also explicitly been calculated. In this particular case, it is still advantageous in an applied sense to utilize the extrapolated

power law over what would effectively be a lookup table with the understanding that random error estimates by the RFM are larger than those by other direct methods (Dias et al., 2018).

The decision to perform the RFM in spatial coordinates instead of in the time dimension also warrants a brief discussion. With considerations for hard disk drive storage space, it is not computationally feasible to save every single volumetric output for the total of 1.26×10^6 timesteps. At our prescribed output frequency, the resulting temporal resolution would equate to an order of magnitude worse spatial resolution when invoking Taylor's hypothesis, so to retain as much information as possible we iterate over individual streamwise segments as described previously. In the case that we did perform the RFM in temporal coordinates, then step 10 would no longer be necessary as one could simply input the desired sampling time directly into the derived power law.

To determine errors in wind speed $u_h = (\langle u \rangle^2 + \langle v \rangle^2)^{1/2}$, wind direction $\alpha = \arctan(\langle u \rangle / \langle v \rangle)$, and momentum flux u_*^2, we implement error propagation based on these parameters' functional dependence on the direct LES output of $u, v, \langle u'w' \rangle$, and $\langle v'w' \rangle$. In general, for a given variable c with functional dependence on the variables a, b (i.e. $c = f(a, b)$), it is possible to relate all of their error variances based on a Taylor expansion (e.g., Bevington and Robinson, 1969; Salesky and Chamecki, 2012) as

$$\sigma_c^2 \approx \sigma_a^2 \left(\frac{\partial c}{\partial a} \right)^2 + \sigma_b^2 \left(\frac{\partial c}{\partial b} \right)^2 + 2\mathrm{Cov}(a, b) \frac{\partial c}{\partial a} \frac{\partial c}{\partial b}, \tag{3.12}$$

where $\mathrm{Cov}(a, b)$ is the covariance between the errors in a and b. In practice, this third error covariance term on the right-hand side of Equation 3.12 is difficult to calculate or interpret even with full volumetric output from LES. We assume that all errors

are uncorrelated, thereby neglecting this term in further calculations. Applying Equation 3.12 to estimate relative random errors in u_h, α, and u_*^2 gives us the following expressions:

$$\epsilon_{u_h} = \frac{\sigma_{u_h}}{|\langle u_h \rangle|} \approx \frac{1}{\langle u_h \rangle} \left(\frac{\sigma_{u^\dagger}^2 \langle u^\dagger \rangle^2 + \sigma_{v^\dagger}^2 \langle v^\dagger \rangle^2}{\langle u^\dagger \rangle^2 + \langle v^\dagger \rangle^2} \right)^{1/2}, \tag{3.13a}$$

$$\epsilon_\alpha = \frac{\sigma_\alpha}{|\langle \alpha \rangle|} \approx \frac{1}{\langle \alpha \rangle} \left(\frac{\sigma_{u^\dagger}^2 \langle v^\dagger \rangle^2 + \sigma_{v^\dagger}^2 \langle u^\dagger \rangle^2}{(\langle u^\dagger \rangle^2 + \langle v^\dagger \rangle^2)^2} \right)^{1/2}, \tag{3.13b}$$

and

$$\epsilon_{u_*^2} = \frac{\sigma_{u_*^2}}{|u_*^2|} \approx \frac{1}{u_*^2} \left(\frac{\sigma_{u'w'}^2 \langle u'w' \rangle^2 + \sigma_{v'w'}^2 \langle v'w' \rangle^2}{u_*^4} \right)^{1/2}. \tag{3.13c}$$

Note that when performing the error propagation calculations using Equation 3.13, we use the unrotated forms of u and v, denoted $u^\dagger$ and $v^\dagger$, along with their associated errors from the RFM.

3.5 Results

In this section we provide a general overview with the simulated mean profiles for each of cases A–F in Section 3.5.1, consider the stability- and height-dependence of random errors in Section 3.5.3, and consider implications of random errors to observations collected by UAS and eddy-covariance in Sections 3.5.4 and 3.5.5, respectively.
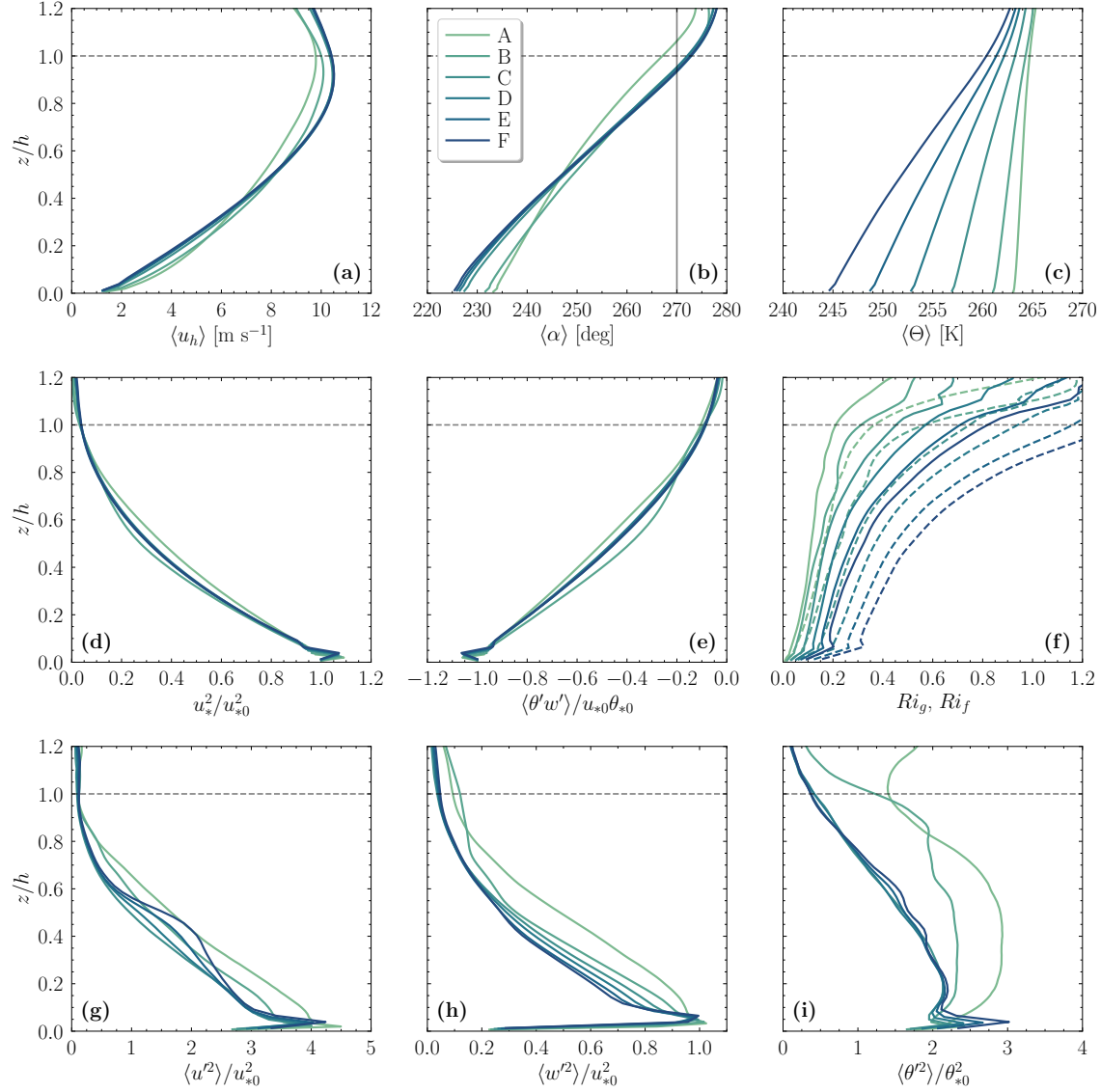
Figure 3.3: Mean profiles of (a) wind speed, (b) wind direction, (c) potential temperature, (d) total (resolved plus SGS) momentum flux, (e) total heat flux, (f) bulk Richardson number (solid) and flux Richardson number (dashed), (g) streamwise velocity variance, (h) vertical velocity variance, and (i) potential temperature variance for all cases A–F as a function of z/h. For (d)–(i), quantities are scaled by surface values of u_* and θ_* where appropriate.

3.5.1 Mean Profiles and Instantaneous Fields

In general the wind speed profiles (Figure 3.3a) do not change drastically with stability, although there are subtle differences in curvature for $z/h < 0.4$. The low-level jet height z_j relative to the SBL height h is also largely unaffected by stability (see Table 3.1). The wind direction profiles (Figure 3.3b) are also relatively insensitive to stability, and one can see a general veering with height consistent with the canonical idealized SBL (e.g., Zilitinkevich, 1989). The potential temperature profiles (Figure 3.3c) demonstrate mean lapse rates that increase strongly with surface cooling rates, as expected (Table 3.1).

The profiles of nondimensional momentum and heat fluxes (Figures 3.3d,e) collapse to common curves, with irregularities in the lowest few grid points likely induced by the wall model. These profiles compare well with the results from Huang and Bou-Zeid (2013) for their cases A–F. We acknowledge the collapse of these profiles in particular is sensitive to the choice in defining the SBL height h. For example, Sullivan et al. (2016) define their SBL height based on the mean potential temperature gradient. Regardless, this general collapse indicates the quasi-stationarity for these second-order moments as required for an appropriate random error analysis.

Both the gradient and flux Richardson numbers (Ri_g, Ri_f, respectively) increase strongly with height and stability (Figure 3.3f). Here we define Ri_g and Ri_f as

$$Ri_g = \frac{g}{\langle\theta\rangle_0}\frac{\partial\langle\theta\rangle}{\partial z}\left[\left(\frac{\partial\langle u^\dagger\rangle}{\partial z}\right)^2 + \left(\frac{\partial\langle v^\dagger\rangle}{\partial z}\right)^2\right]^{-1}, \qquad (3.14a)$$

$$Ri_f = \frac{g\langle\theta'w'\rangle}{\langle\theta\rangle_0}\left[\langle u'w'\rangle\frac{\partial\langle u^\dagger\rangle}{\partial z} + \langle v'w'\rangle\frac{\partial\langle v^\dagger\rangle}{\partial z}\right]^{-1}. \qquad (3.14b)$$

The resulting profile of the turbulent Prandtl number, $Pr_t \equiv K_m/K_h = Ri_g/Ri_f$, is relatively constant with height with values between 0.6–0.7 (not shown). Since Pr_t is defined based on the ratio between the momentum and heat transfer eddy diffusivities (K_m and K_h, respectively), this implies a dissimilarity between the turbulent transports of momentum and heat for the flows considered. This topic will be discussed in further detail in Chapter 4.

The nondimensional streamwise and vertical velocity variances (Figures 3.3g,h) display similar trends where the variances generally decrease with stability in the middle of the SBL. Enhanced levels of $\langle u'^2 \rangle$ between $0.2 < z/h < 0.6$ for cases E and F could be signatures of intermittent turbulence or related to inertial oscillations within the SBL. Finally, the nondimensional potential temperature variance (Figure 3.3i) follows two general trends dependant on stability. In cases A and B the variance general increases from the surface up to $z/h \approx 0.2$, remains constant up to $z/h \approx 0.6$, and then decreases with height. Variances in cases C–F peak close to the surface and generally decrease with height monotonically for $z/h > 0.2$. Common across all cases, however, is that for $z/h < 0.1$, variance generally increases with stability. The implications for this pattern will be discussed further in Section 3.5.3.

For a qualitative comparison between cases A and F, Figure 3.4 portrays instantaneous $x - z$ cross-sections in the center of the domain for scaled streamwise velocity and potential temperature. In case A (Figure 3.4a,b) there is evidence of turbulent motions with pockets of high and low momentum throughout as well as quasi-organized structures within the temperature fields (e.g., between $1.0 < x/h < 1.8$ and $0.3 < z/h < 0.75$) reminiscent of the microfronts observed by Sullivan et al. (2016). Case F (Figure 3.4c,d) appears far more quiescent, as one may expect for strongly stable conditions. Both the velocity and temperature fields are highly stratified, and the
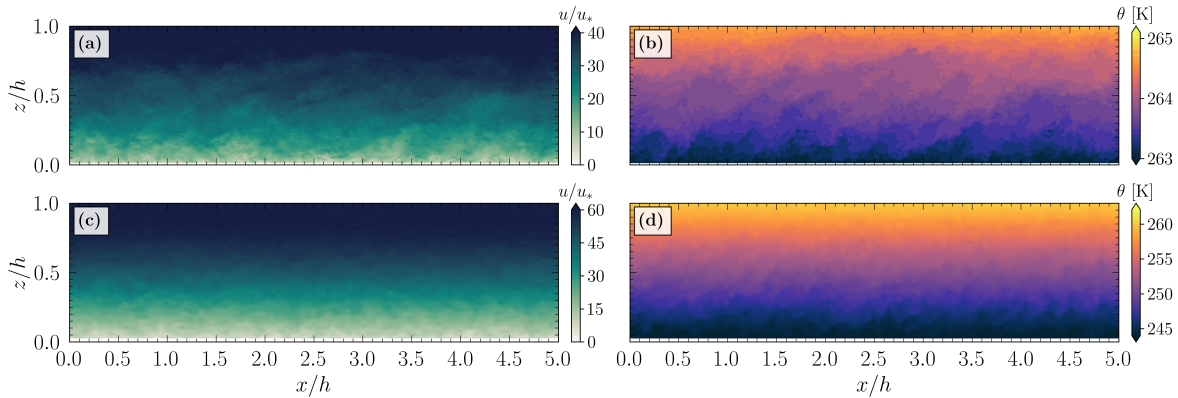
Figure 3.4: Instantaneous x–z cross-sections at $y = L_y/2$ of scaled streamwise velocity (left column) and potential temperature (right column) for simulations A and F (top and bottom rows, respectively).

vertical extent of eddies are considerably smaller than those in case A. This perspective supports the expectation that in general, we would expect integral lengthscales in the SBL to decrease with increasing stability.

3.5.2 Integral Lengthscales

To provide context for the random error profiles in the following section, in Figure 3.5 we include the integral lengthscales of first-order parameters determined from the volumetric LES output. These lengthscales were calculated along individual streamwise samples of the full volumetric field by integrating the sample's spatial autocorrelation function until the first zero crossing. This process was repeated and averaged over all y and timesteps as in the RFM described in Section 3.4, resulting in vertical profiles of integral lengthscales, $\mathcal{L}(z)$.

For all parameters it is readily apparent that the integral scales decrease at all heights with stability. For weak stability, there is a peak in $\mathcal{L}_u$ around $0.5 < z/h < 0.7$, just below the level of the LLJ (Figure 3.3a), whereas with increasing stability these scales remain generally constant with height for $0.2 < z/h < 0.8$ (Figure 3.5a).
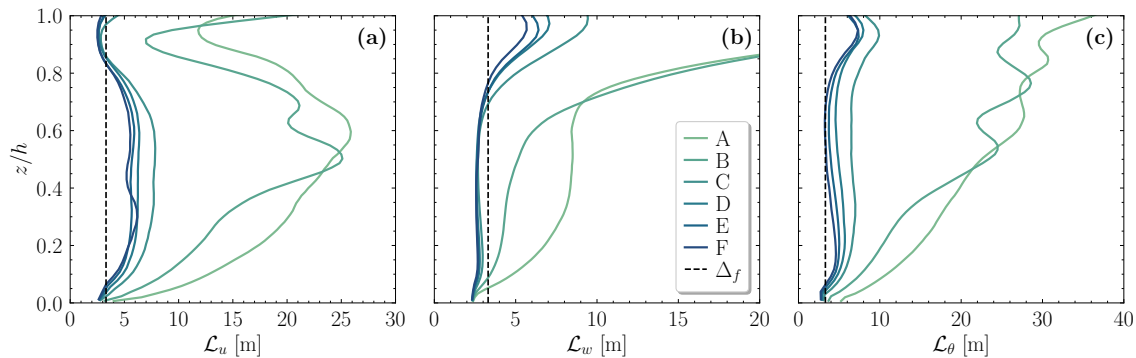
Figure 3.5: Profiles of integral lengthscales for (a) streamwise velocity, (b) vertical velocity, and (c) potential temperature for all six cases A–F. The LES filter width Δ_f is plotted as a vertical dashed black line for reference.

In general, $\mathcal{L}_u$ is larger than $\mathcal{L}_w$ for all stabilities and heights (Figure 3.5b), and is comparable in magnitude to $\mathcal{L}_\theta$ (Figure 3.5c). For cases C–F, $\mathcal{L}_w$ is of similar length to the LES filter scale Δ_f below the LLJ, indicating that buoyancy strongly acts to suppress vertical turbulent mixing through the characteristic size of eddies.

The integral scale profiles for cases A–C are generally on par with those presented by Huang and Bou-Zeid (2013) (note that they did not include an estimate for the potential temperature lengthscale), most notably in the shape of the peaks in $\mathcal{L}_u$ and the strong increase in $\mathcal{L}_w$ with height for $z/h > 0.6$. Interestingly, for cases D–F, our results do not indicate the strong peak in $\mathcal{L}_u$ around $z/h \approx 0.4$ that they reported being related to buoyantly-flattened coherent structures. Although our simulations are based on those by Huang and Bou-Zeid (2013) and other mean profiles compare strongly (Figure 3.3) to theirs, determining the reasoning behind these discrepancies in integral scales is outside the scope of this chapter.
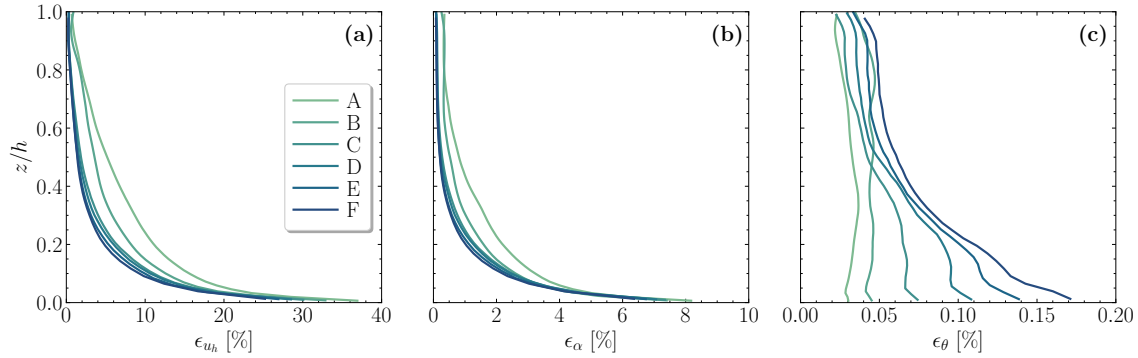
Figure 3.6: Profiles of relative random errors for (a) wind speed, (b) wind direction, and (c) potential temperature for all six cases A–F. Errors are calculated based on 3 s averaging times consistent with typical UAS observation processing.

3.5.3 Random Error Profiles

Utilizing the RFM outlined in Sections 3.2 and 3.4, in Figure 3.6 we show relative random errors for the first-order thermodynamic and kinematic parameters typically observed with UASs as a function of stability and z/h. It is apparent that errors generally decrease with height and stability for wind speed and direction (Figure 3.6a,b), which can logically follow from the premise that integral lengthscales for velocity components decrease with stability (Figure 3.5a,b), and larger errors are associated with longer integral lengthscales via Equation 3.2. This is additionally supported by the fact that the dimensional values of streamwise velocity variance also decreases with stability (Figure 3.3g, recall from Table 3.1 that u_{*0} decreases with stability) which would necessitate longer averaging times at weak stability to constrain the natural variability in the flow. To the contrary, relative random errors in potential temperature actually increase with stability (Figure 3.6c), and do not decrease as strongly with height. While possibly counterintuitive at first, this potential temperature error pattern can be justified physically as follows. As surface cooling increases with global stability, the near-surface lapse rates increase in magnitude more rapidly. From Lumley and

87

Panofsky (1964) and Wyngaard and Coté (1971), this temporally-evolving temperature gradient is a source term in potential temperature variance (given a stationary heat flux, which is generally valid in this case), which would correspondingly increase the amount of averaging time necessary for a timeseries mean to converge towards the ensemble mean potential temperature. This is also consistent with the mean profiles of potential temperature variance (Figure 3.3i) wherein the dimensional value of $\langle \theta'^2 \rangle$ generally increases with stability (again recall from Table 3.1 that θ_{*0} increases by an order of magnitude between cases A and F and therefore so do the dimensional variances). Therefore, stronger stability begets larger ϵ_θ, as seen in Figure 3.6c.

For all profiles, and especially at lower stabilities, the near-surface wind speed errors are substantial (i.e. $> 25\%$). For context, a relative random error of 25% implies that a wind speed of 2 m s^{-1} near the surface could result in an error standard deviation of at least 0.5 m s^{-1} due just to the limited averaging time. Additionally, a 0.1% error from an observed $\theta = 250$ K results in an absolute error of only 0.25 K. These errors are of the same order of magnitude as those due to calibration and instrument uncertainty, which are independent of each other and therefore are compounded. For example, the CopterSonde rotary-wing UAS is accurate to within 0.6 m s^{-1} and 0.5°C compared against radiosondes (Segales et al., 2020; Bell et al., 2020). The most direct solution to offset these errors is to increase the averaging times in the lower SBL, which is then a tradeoff between UAS vertical ascent rates and the vertical resolution desired (discussed further in Section 3.5.4).

The relative random errors for second-order moments based on 30-min averaging times (Figure 3.7) also generally decrease with stability. Recall that we utilize 30-min averaging times for these parameters, which is consistent with typical values used with the eddy-covariance method. The errors in Reynolds stresses are relatively constant
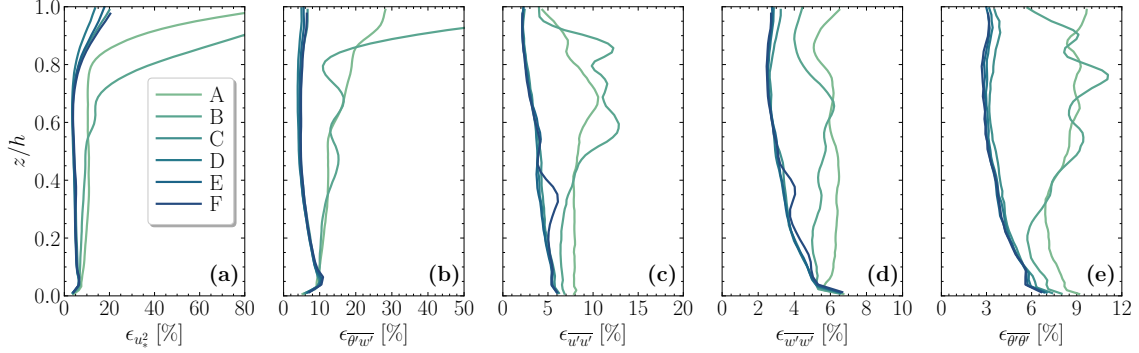
Figure 3.7: Profiles of relative random errors for (a) momentum flux, (b) potential temperature flux, (c) streamwise velocity variance, (d) vertical velocity variance, and (e) potential temperature variance for all six cases A–F. Errors are calculated based on 30 min averaging times consistent with typical eddy-covariance measurements.

between 5–15% from the surface up to $z/h \approx 0.7$ (Figure 3.7a). Due to the way we define h as a linear extrapolation to where $u_*^2 \to 0$, and since u_*^2 appears in the denominator when calculating $\epsilon_{u_*^2}$ via Equation 3.13c, the errors near the top of the SBL grow to be considerably larger than near the surface. To a lesser extent this pattern also occur near the top of the SBL for $\epsilon_{\overline{\theta'w'}}$ for cases A–C, likely for similar reasons (Figure 3.7b).

The errors for heat flux across all cases (Figure 3.7b) nearly double from the surface to $z/h \approx 0.07$ for all cases. This may be indicative of surface layer processes, although it could also be an artifact of the LES wall model. For $0.15 < z/h < 0.7$, $\epsilon_{\overline{\theta'w'}}$ appears to organize into two categories: increasing slowly with height (cases A and B) and decreasing slowly with height (cases C–F). These two groups likely correspond to differing regimes of fully turbulent flow in weakly stable stratification versus generally weak vertical mixing at higher stability.

The error profiles of velocity and potential temperature variances (Figure 3.7c,d,e) also exhibit this clustering into two primary groups of 1) cases A and B, and 2) cases C–F. The $\epsilon_{\overline{u'u'}}$ and $\epsilon_{\overline{\theta'\theta'}}$ profiles peak around $z/h \approx 0.7$ for group 1, and group 2 does

not necessarily peak but rather decreases continuously throughout the SBL. For all cases, however, the magnitudes of the relative errors are consistently in the 5–20% range for streamwise velocity variance and even narrower ranges of 2–8% for vertical velocity variance and 3–12% for potential temperature variance. These results are consistent with the notion that turbulence intensity within increasingly stable regimes should become weaker, resulting in increasingly localized motions with smaller integral scales (as also hinted to by Figure 3.5). The general decrease in height for the second-order errors combined with decreasing variability for higher stabilities is also consistent with the "z-less" scaling regime. This is because the distance from the ground loses relevance as a characteristic length for higher stratification as turbulence becomes more localized and mixing lengths depend more on parameters such as wind shear and buoyancy frequency (e.g., van de Wiel et al., 2008; Huang et al., 2013; Sorbjan, 2017; Greene et al., 2022). Since these parameters do not change dramatically with height in the quasi-stationary cases presented, it is reasonable to conclude that the corresponding second-order integral lengthscales would similarly remain relatively constant with height, thereby resulting in the observed profiles of relative random errors in the second-order moments.

The exponent p determined by least-squares fitting of Equation 3.8 lies within the range $0.8 < p < 1.2$ for all parameters shown at all heights and stabilities (not shown). This corresponds to a similar range in the Hurst exponent H as found Dias et al. (2018) using sonic anemometer data, indicating that Hurst's phenomenon is indeed influencing the flow dynamics. Therefore, error estimates by the RFM will generally exceed those by the Lumley and Panofsky method of Equation 3.1 and the existence of an integral scale is dubious (Dias et al., 2004, 2018). Regardless, we include these integral scales (Figure 3.5) for improved physical understanding of the random error results.

3.5.4 Implications for Measurements from Uncrewed Aircraft Systems

A UAS takes a finite amount of time to fly a vertical profile, and the atmosphere is continually evolving while it does so. Figure 3.1 conceptualizes this for a UAS ascending at 1 m s^{-1} through the depth of the SBL, which in this case would take about three minutes to reach a height of $z = h$. In this section we emulate a rotary-wing UAS ascending through the simulated domain at a fixed rate as described in Section 3.3.2. Note that these emulated profiles assume idealized thermodynamic and kinematic sensors free from bias, imprecision, or dynamic response errors, as we are strictly interested in the impact of random errors on observed profiles. Finally, we calculate random error bounds for these emulated profiles based on the results from the previous section for comparison with the ensemble mean profiles (i.e., Figure 3.3). These error bounds physically represent the error standard deviation σ_f for a given parameter f due to inadequate sampling time (recall Eqs. 3.1 and 3.8), which we refer to succinctly as the random error. They are determined by combining an observed parameter $f_{obs}(z)$ with its corresponding relative random error $\epsilon_f(z)$ as $\sigma_f(z) = f_{obs}(z)\epsilon_f(z)$ to yield a dimensional value. In Figure 3.8 (and later in Figure 3.11), these dimensional values of random error are shaded around the emulated observation values at each height corresponding to the 1 and 3σ levels, which should virtually capture the full range of random errors in an ensemble of realizations.

In Figure 3.8 we demonstrate the ability of emulated UAS profiles to represent the ensemble mean for wind speed, wind direction, and potential temperature in cases A and F. In general it is apparent that the UAS profiles are more variable with height in case A (Figure 3.8a–c) as compared to case F (Figure 3.8d–f). This is likely related to the integral length scales being smaller at high stability (Figure 3.5) resulting in smaller

91
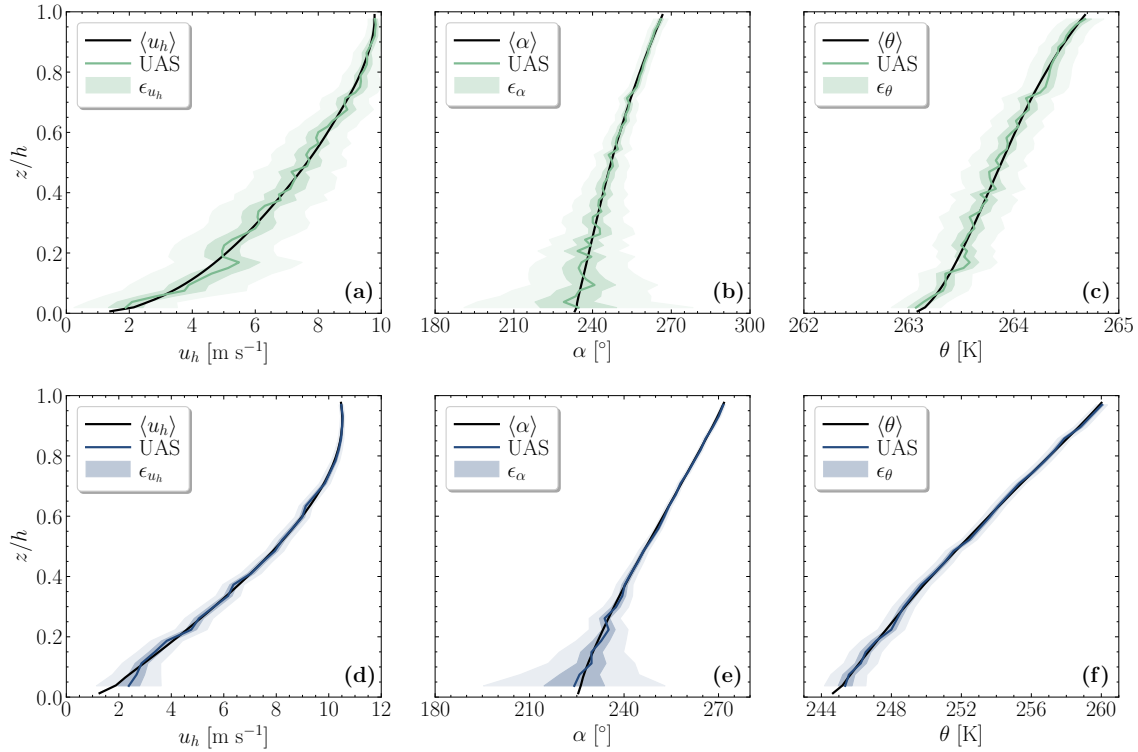
Figure 3.8: Profiles of (left) wind speed, (center) wind direction, and (right) potential temperature from cases A (top) and F (bottom). The solid black line in each is the horizontally and temporally averaged ensemble mean reproduced from Figure 3.3. Each colored solid line represents observations from an emulated UAS profile ascending at 1 m s^{-1} and averaged in 3 s bins. Dark (light) shading denotes 1 (3) error standard deviations.

random errors for case F. Each of these UAS profiles exhibit differences relative to their respective ensemble means, and these differences are also smaller for higher stability. For both cases A and F, the random errors in wind direction (Figure 3.8b,e) near the surface are substantial at these averaging times, with 3σ ranges of around 90°. This is related to the relatively low wind speeds close to the surface, which some observational systems have difficulty measuring to begin with. We also note that the uncertainty range in wind speed for case A (Figure 3.8a) spans between 0–4 m s^{-1} at the 3σ level, which may further add to operational difficulties in determining representative wind directions at weak stability. Although the emulated profiles of wind speed for case F (Figure 3.8d) generally converge to the ensemble means on their own due to shorter integral lengthscales at high stabilities, it is still apparent that errors for $z/h < 0.2$ are of similar order of magnitude to the observations themselves.

With these results, it is therefore apparent that maintaining constant ascent rates (and corresponding constant averaging times) for UAS within the SBL may result in disproportionately large random errors close to the ground. To address this issue, Figure 3.9 portrays the parameter space of relative errors contoured as functions of both z/h and averaging times for cases A and F. It is initially apparent that these errors drop off rapidly with averaging time, which follows directly from the power-law relationship fundamental to these estimations (Equation 3.8). One can see that it is generally difficult to mitigate errors in u_h and α below $z/h < 0.1$ for both cases without averaging for an impractical amount of time, as UAS battery capacity becomes a limiting factor in the ability to sample the entire SBL in a single flight. This issue can potentially be overcome through pairing UAS operations with other continually-sampling sensors such as eddy-covariance systems or ground-based remote sensors, which can be averaged arbitrarily long to supplement UAS profiles. It is additionally
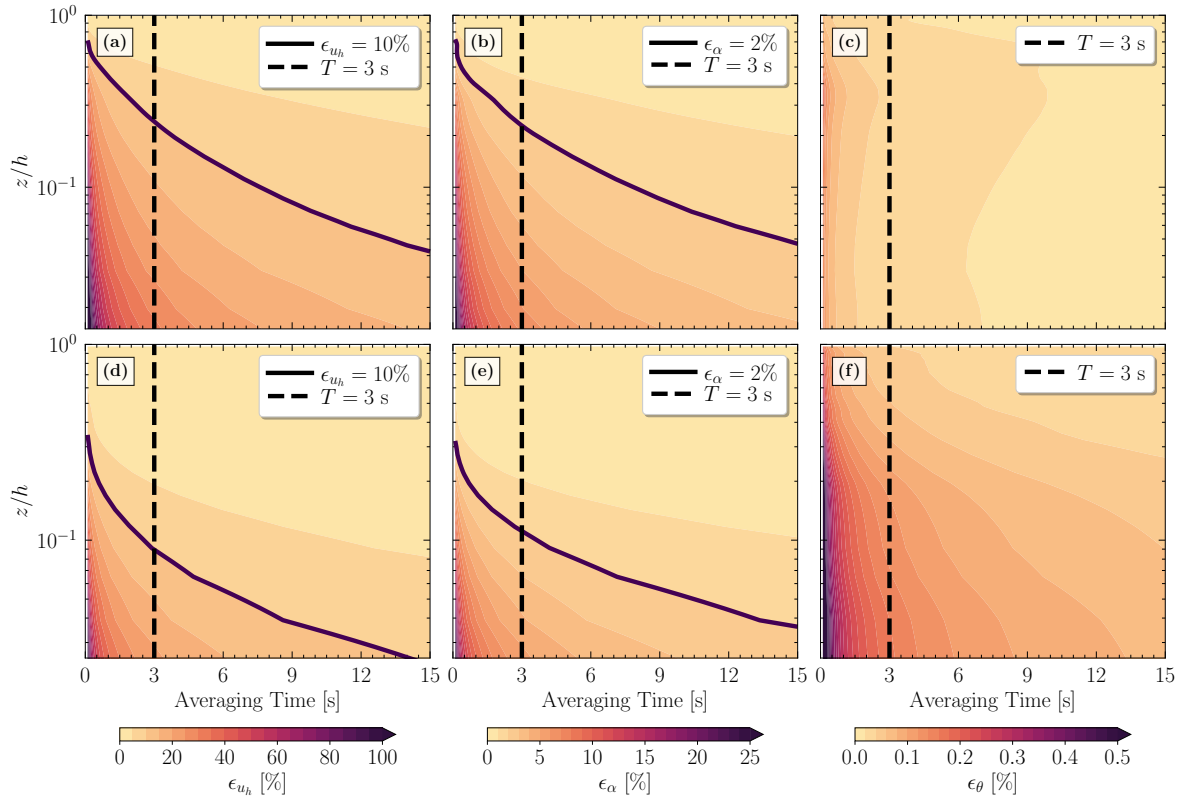
Figure 3.9: Contours of relative random errors in (left) wind speed, (center) wind direction, and (right) potential temperature as functions of height and averaging time during cases A (top) and F (bottom). For reference, the vertical dashed line denotes an averaging time of 3 s, and the solid black contours denote error levels of 10% in (a),(d) and 2% in (b),(e). Note that the y-axis for each panel is logarithmic and the color scale range varies for each parameter.

apparent from Figures 3.9c and f that the errors in potential temperature are small (but not negligible) across the displayed parameter space. In case A there is little dependence on either z/h or averaging time, whereas these dependencies are modestly stronger in case F.

Due to the adaptive abilities of UAS technology, it is possible for a UAS operator to optimize a flight plan that accounts for random error dependencies on stability, height, and averaging time. For example, if an end-user wishes to specify a threshold of random errors they deem acceptable, they would first need to obtain an estimate of atmospheric stability from e.g. an instrumented tower to estimate the local surface cooling rate or Obukhov length, a ground-based remote sensor that can estimate the SBL depth, or the static stability as measured by a previous UAS flight or radiosonde launch to compare with the values in Table 3.1. It is also possible to estimate the dimensionless parameter z/L from multiple levels of tower-based observations utilizing Monin-Obukhov similarity functions (Launiainen and Vihma, 1990). With this information, a UAS could be programmed in a pre-defined mission to ascend at variable rates. This variable ascent rate would enable a constant post-processed vertical resolution and also takes into account the necessary amount of averaging time required at each height to reach the desired threshold. Figure 3.10 highlights this process for u_h and α in cases A and F assuming a constant 3 m altitude bins after averaging. These bins were chosen as a tradeoff between the accuracy of typical UAS autopilot altitude estimations and the desire to achieve the highest reasonable vertical resolution (see Greene et al., 2022). Note that we omitted the analysis ascent rate accounting for θ, as the averaging times necessary to approach $\epsilon = 1\%$ were so short that the ascent rate was effectively not a factor.
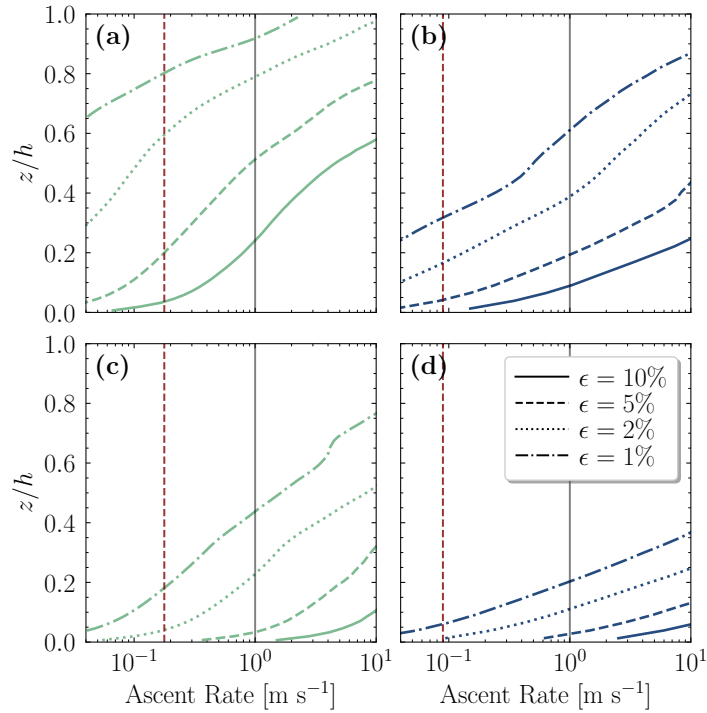
Figure 3.10: Optimal ascent rates for various error levels for observations collected during an emulated UAS vertical profile with constant 3 m altitude bins for the following: (top row) wind speed, (bottom row) wind direction, (left column) case A, (right column) case F. For reference, a vertical solid grey line is included for a 1 m s^{-1} ascent rate, and the vertical dashed red lines denote the minimum constant ascent rate required to reach $z = h$ within 15 min.

From Figure 3.10 it is readily apparent that to achieve $\epsilon_{u_h} \leq 5\%$ for $z/h < 0.2$, a UAS must ascend with a vertical velocity v_z of $\mathcal{O}(0.01\text{–}0.1)$ m s^{-1} across all stabilities. A similar trend is also discernible for ϵ_α, although relative random errors are generally smaller for α and therefore higher ascent rates are warranted. Herein lies a significant challenge when designing a UAS flight strategy: the total battery discharge time for a rotary-wing UAS utilizing lithium-polymer batteries such as the CopterSonde is generally $\approx$15 min (Segales et al., 2020). Ascending at ≤ 0.1 m s^{-1} for $z/h < 0.2$ would therefore not guarantee enough battery charge to ascend the full depth of the SBL. In Figure 3.10 we visually represent this by overlaying the minimum ascent rate required to reach $z = h$ within 15 min. A UAS operator is thus presented with a tradeoff when designing a flight strategy. They could either fly slowly close to the surface to minimize random errors but risk not sampling the entire SBL in one flight, or they could sacrifice the random error uncertainty to prioritize a maximum flight altitude.

In Section 3.5.5 we continue this analysis for second-order moments that may be collected by eddy-covariance systems or fixed-wing UASs with a turbulence-resolving sensor payload.

3.5.5 Implications for Eddy-Covariance Measurements

Determining second-order turbulence moments from observations within the SBL requires substantially longer averaging times than for first-order moments to achieve similar levels of relative random errors (see Figure 3.7; Lenschow et al., 1994; Mann and Lenschow, 1994; Dias et al., 2004). This concept will be especially important as sensors continue to miniaturize and both rotary- and fixed-wing UASs can more reliably collect turbulence-resolving observations. We again employ the virtual tower output
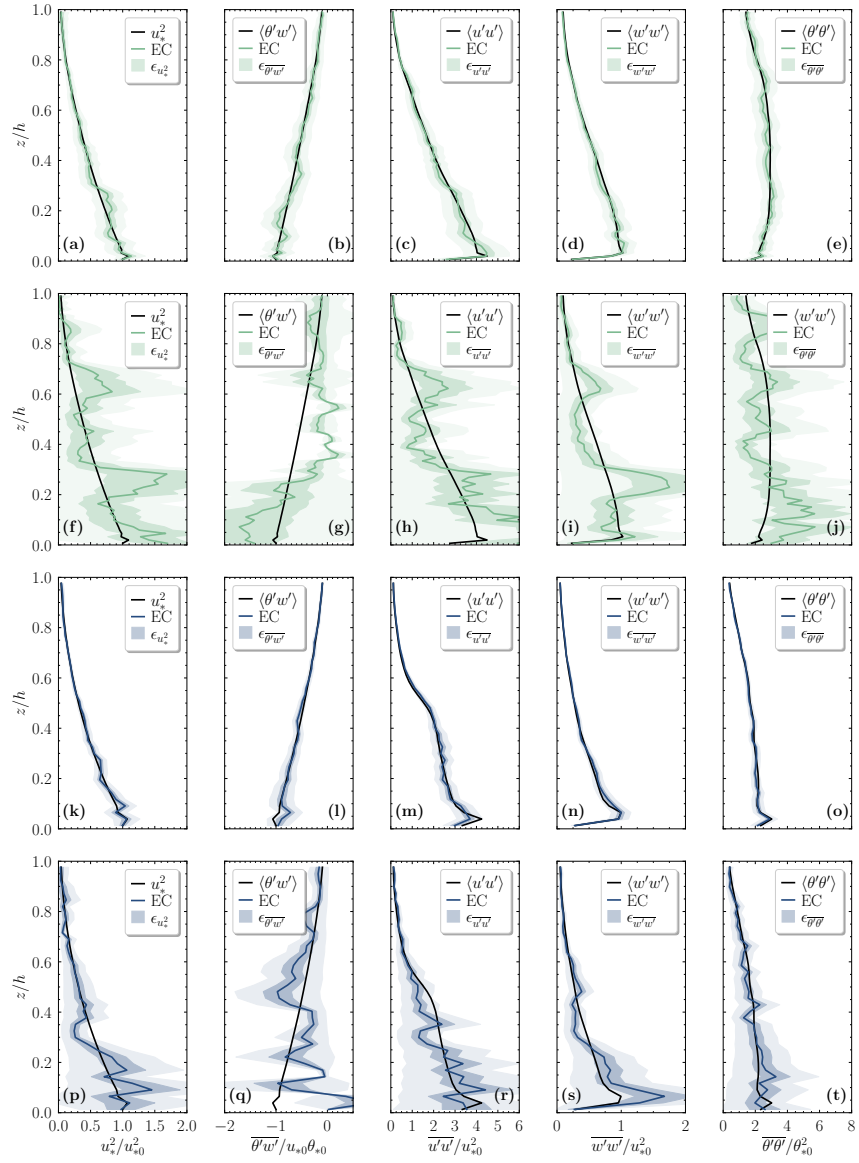
Figure 3.11: Profiles of normalized (a,f,k,p) momentum flux, (b,g,l,q) heat flux, (c,h,m,r) streamwise velocity variance, (d,i,n,s) vertical velocity variance, and (e,j,o,t) potential temperature variance from cases A (rows 1 and 2) and F (rows 3 and 4). The emulated profiles are evaluated for 30 min averaging time in rows 1 and 3, and 1 min in rows 2 and 4. As in Figure 3.8, the solid black lines denote the xyt-averaged LES output whereas the colored lines are emulated virtual eddy-covariance (EC) towers in the center of the domain. Dark (light) shading denotes 1 (3) standard deviation of random errors.

described in Section 3.3.2 to emulate eddy-covariance observations that are sampled simultaneously. This framework could be interpreted as 1) a tall instrumented tower or a collection of either 2) fixed-wing UASs flying at fixed-altitude circling within the horizontal domain or 3) vertically dispersed rotary-wing UASs hovering at a fixed position in space.

The resulting emulated profiles of normalized fluxes and variances are presented in Figure 3.11 for cases A and F. One can see from Figure 3.11 that in general the 30 min eddy-covariance profiles approximate the ensemble means reasonably well across the range of stabilities. The error bounds for each of the four second-order moments also encapsulate the ensemble mean profiles for virtually all heights and stabilities. The mean absolute differences between the emulated and ensemble mean profiles are also generally smaller for case F than case A, which follows the same trends we have observed throughout the chapter.

The emulated eddy-covariance profiles averaged over only 1 min depict a vastly different scenario. These 1-min profiles in case A vary substantially with height, with the only discernible trends being a gradual decrease with z/h (Figure 3.11e–h). The case F 1-min profiles are at least of the same order of magnitude as the ensemble mean, but also demonstrate considerable variability with height (Figure 3.11m–p). The corresponding random error bounds are also substantial, often of the same order of magnitude as the fluxes and variances themselves. While these results are perhaps unsurprising, they are provided as emphasis that many considerations are necessary to properly calculate physically meaningful second-order turbulence moments as it becomes more accessible to obtain the necessary observations with UAS.

To expand upon the two discrete averaging times for the emulated profiles demonstrated previously in Figure 3.11, we consider the parameter space of averaging times as
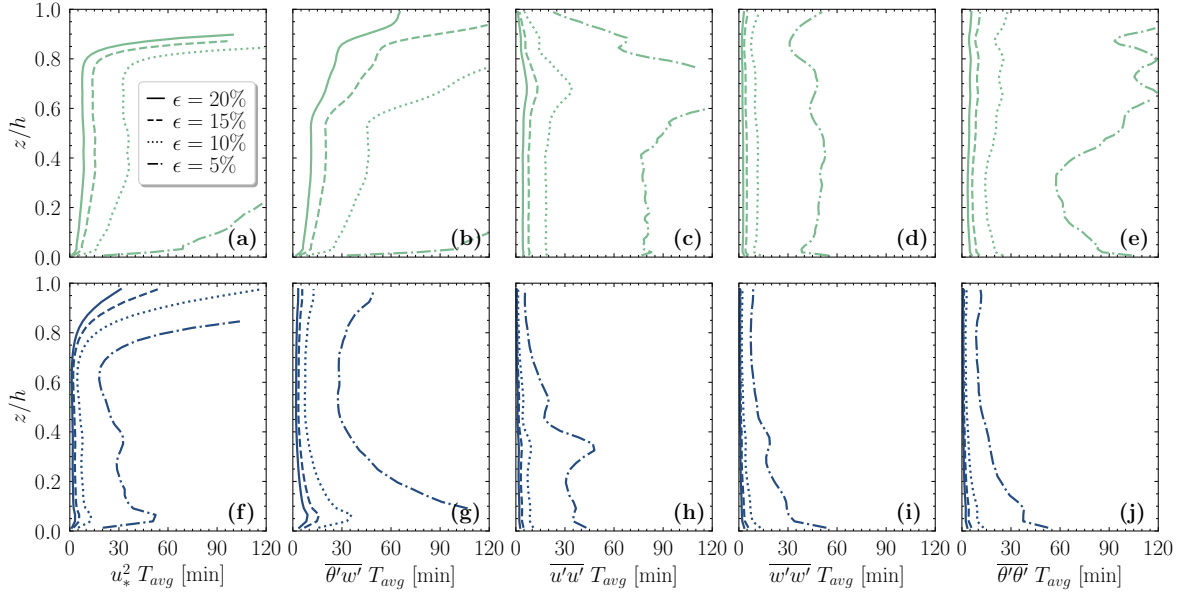
Figure 3.12: Profiles of necessary eddy-covariance averaging times (T_{avg}) to reach specified levels of relative random error for cases A (top row) and F (bottom row). The second order moments include (a,f) momentum flux, (b,g) temperature flux, (c,h) streamwise velocity variance, (d,i) vertical velocity variance, and (e,j) potential temperature variance.

a function of stability, z/h, and desired level of relative random errors. In Figure 3.12, one can draw the comparison to the framework presented in Figure 3.10, except in this case we are concerned only with averaging times at each height. In case A (Figure 3.12a–e) for example, it is difficult to achieve errors less than 5% near the surface, as the necessary averaging times exceed 1 hr, and the ABL cannot always be expected to be quasi-stationary over these long averaging periods. One is again potentially faced with a tradeoff in the application of these results, and may need to compromise on the level of acceptable random errors for observations collected near the surface. On the contrary, achieving even a 10% error level is far more accessible across all stabilities, heights, and parameters, with averaging times ranging between 10–30 min. The velocity variance component error profiles in both cases (Figure 3.12c,d,h,i) as well as potential temperature variance (Figure 3.12e,j) require even shorter averaging times

100

for $\epsilon > 10\%$ at all heights, at 15 min or less. These relatively short averaging times for the velocity variances are again indicative of the weak nature of turbulence intensity in the SBL that correspond to small integral lengthscales. For weak stability it generally requires more averaging time to constrain $\overline{u'u'}$ and $\overline{\theta'\theta'}$ than it does for $\overline{w'w'}$ for a given error level, but they become more comparable at high stability.

3.6 Discussion

Clearly there is no universal means to mitigate random errors for any of the considered first- and second-order turbulence moments. Even with careful experimental consideretions for atmospheric stability, instrumentation heights, and averaging times, without access to an infinitely dense observational network, random errors are unavoidable for observations of real-world geophysical flows. We therefore analyze these results by contextualizing the random errors one might expect for their observations across a realistic parameter space.

Given the magnitude of errors in first-order moments near the surface, it may be difficult for a UAS to adequately sample for long enough and still reach the target maximum altitude on a single battery charge. For this reason we recommend conducting UAS operations in proximity to surface-based observational systems whenever possible. Tower-mounted instruments and ground-based remote sensors (i.e. Dopper wind lidars, microwave radiometers, etc.) have the advantage of continually observing at a fixed location in space (Smith et al., 2019, 2021; Bonin et al., 2020). Therefore, the raw timeseries output from these sensors can be averaged at longer temporal periods than for UAS observations to mitigate random errors close to the surface.

Another possibility for improving the representativeness of UAS observations involves the temporal averaging of multiple vertical profiles as in Greene et al. (2022).

This technique consists of averaging discontinuous subsamples of the overall atmospheric flow at a fixed point, which may have nonlinear impacts on the overall reduction in random errors. Similarly, one could also consider the averaging of multiple simultaneous UAS profiles distributed spatially within a target domain (Balsley et al., 2018; van den Heever et al., 2021). The exact quantification of these methods is beyond the scope of this chapter, but it logically follows that these would be effective methods of reducing random errors in general.

The quantification of random errors for potential temperature variance are of particular interest with regards to recent studies in the SBL using distributed temperature sensors compared with instrumented towers (Peltola et al., 2021), UAS (Higgins et al., 2018), and tethered balloons (Fritz et al., 2021; Lapo et al., 2022). As technology advances and rotary-wing UAS sensors continue to miniaturize, it is possible that potential temperature variance may be easier to observe directly when compared with velocity component variances, which typically rely on complex autopilot-based physical retrievals for estimates.

We acknowledge that this chapter only addresses an idealized parameter space with respect to the SBL. True geophysical flows are rarely characterized by horizontally homogeneous topography or land surface usage, and the diurnal cycle can drastically impact the assumption of stationarity. Regardless, the results from this chapter retain significant utility as a baseline of random errors, especially since the RFM has also been shown to produce larger estimates than through alternative methods (Dias et al., 2018).

It is important to note that random errors are not directly comparable with instrumental errors due to their underlying sources. Random errors are resultant of fundamental stochastic processes, and are to be interpreted as how well a given observation can represent the overall flow in an ensemble sense. This is not necessarily the

same interpretation of instrumental biases or imprecision, which relate the ability of a sensor to describe its ambient environment at any given time. Further studies are necessary to determine how to best combine these sources of error for the purposes of NWP data assimilation of SBL observations.

Finally, as with any study with wall-modeled LES, reasonable uncertainty exists for all results close to the surface. This is largely due to the inability of LES to explicitly resolve turbulent motions in the viscous sublayer and instead relying on a wall model (in our case based on the dimensionless Monin-Obukhov similarity functions). Especially at higher stabilities, this may affect the resulting random error profiles close to the surface, although to what extent remains unknown. A recent pair of studies by Chinita et al. (2022a,b) used LES with a very small domain size and a 10 cm grid resolution to better resolve the surface layer of SBLs, which could potentially be suitable for comparisons with ground-based instrumented meteorological masts. A direct numerical simulation or wall-resolved LES would likewise provide more detailed information close to the wall, but these investigations are beyond the scope of the present chapter.

Chapter 4

Coherent structures in stably stratified wall-bounded turbulent flows

4.1 Research Objectives

While the existence and general features of turbulent coherent structures within SBL flows have recently been explored, at present there is a relative dearth of studies examining their role in modulating turbulence throughout the SBL. This chapter aims to close this knowledge gap by addressing the following key questions:

6. How does stability impact the properties of large-scale motions within the SBL?

7. How does buoyancy affect transport efficiencies of momentum and temperature?

8. How do coherent structures with the SBL contribute to these differences?

The rest of this chapter is organized as follows: we provide an overview of the large-eddy simulation code and cases considered in Section 4.2. We provide justification for the use of LES in studying the SBL along with a discussion on its overall performance in Section 4.3. In Section 4.4 we present our results on mean profiles and instantaneous fields in Section 4.4.1, spectral analysis including spectrograms and linear coherence spectra in Section 4.4.2 and Section 4.4.3, transport efficiencies in Section 4.4.4, amplitude modulation in Section 4.4.5, and conditionally-averaged fields in Section 4.4.6.

We conclude with a general discussion and interpretation of results, along with a future outlook in Section 5.1.3.

4.2   Large-eddy simulation and cases

In this chapter we employ the same LES code summarized in Chapter 3 (see Equations 3.9 and 3.10) as well as Greene and Salesky (2022). The cases presented in this chapter are also identical to those in Chapter 3, with the exception of two additional simulations run at intermediate stabilities to better capture the near-neutral regime. These eight simulations are run with a constant value of surface cooling rate $C_r = -\partial\langle\theta_0\rangle/\partial t$ spanning from values of $0.10 \leq C_r \leq 2.50$ K hr^{-1} (Table 4.1). All other parameters are held constant during the simulations, and are summarized in Table 4.2. For computational efficiency, the simulations were run on a coarse grid of $n = n_x n_y n_z = 96^3$ for six physical hours, after which they were interpolated to a grid of $n = 192^3$ and allowed to run for four more physical hours for a total of ten hours.

As in 3, we use angle brackets $\langle\rangle = \langle\rangle_{xyt}$ to denote ensemble averaging in horizontal planes and over the final hour of simulation, which corresponds to 4.5–7.4 large-eddy turnover times (Table 4.1). Quantities with a prime indicate fluctuations about the mean, e.g. $\widetilde{u}' = \widetilde{u} - \langle\widetilde{u}\rangle$. Additional analysis of these periods indicate they are quasi-stationary (not shown), and to improve statistical robustness we implement linear detrending when calculating second-order turbulent parameters.

We determine the SBL depth h as in Beare et al. (2006), namely h is the normal distance from the wall where the mean stress profile $u_*(z)$ falls to a value equal to 5% of its surface value u_{*0} and then linearly interpolated to zero by dividing by a factor of 0.95. Although many definitions of SBL depth exist in the literature, this one is

Table 4.1: Mean simulation properties for cases A–H averaged over the last physical hour of the simulation, including: the surface cooling rate C_r, SBL height h, low-level jet height z_j, surface friction velocity u_{*0}, surface potential temperature scale θ_{*0}, Obukhov length L, global stability h/L, bulk Richardson number Ri_B, bulk SBL inversion strength $\Delta\langle\theta\rangle/\Delta z$, eddy turnover period T_L, and number of large-eddy turnover times within the last hour nT_L.

Case	C_r	h	z_j	u_{*0}	θ_{*0}	L	h/L	Ri_B	$\Delta\langle\theta\rangle/\Delta z$	$T_L = h/u_{*0}$	nT_L
	(K h^{-1})	(m)	(m)	(m s^{-1})	(K)	(m)	-	-	(K km^{-1})	(s)	-
A	0.10	215	204	0.271	0.0224	220	0.975	0.142	4.64	793	4.5
B	0.25	160	156	0.231	0.0383	93.5	1.71	0.129	10.2	692	5.2
C	0.33	140	141	0.217	0.0463	67.8	2.06	0.134	14.2	646	5.6
D	0.50	135	127	0.211	0.0658	45.1	3.01	0.207	24.1	642	5.6
E	1.00	107	97.4	0.190	0.112	21.1	5.07	0.289	59.7	563	6.4
F	1.50	93.7	86.9	0.180	0.157	13.3	7.05	0.380	101	521	6.9
G	2.00	87.1	80.6	0.172	0.198	9,51	9.16	0.491	147	506	7.1
H	2.50	80.5	74.3	0.166	0.236	7.28	11.1	0.545	198	485	7.4

most consistent with other LES studies of the SBL and still retains the majority of the low-level jet (LLJ) peak.

Here we define the mean stress profile by combining the streamwise and spanwise components as

$$u_*^2 = \left(\langle \widetilde{u}' \widetilde{w}' + \tau_{xz} \rangle + \langle \widetilde{v}' \widetilde{w}' + \tau_{yz} \rangle \right)^{1/2}, \tag{4.1}$$

where τ_{xz} and τ_{yz} are the SGS contributions to momentum flux. Other parameters defined in Table 4.1 include the potential temperature scale $\theta_* = -\langle \widetilde{\theta}' \widetilde{w}' + q_3 \rangle / u_*$ where q_3 is the SGS heat flux, the Obukhov length $L = u_{*0}^2 \langle \theta_0 \rangle / \kappa g \theta_{*0}$ which depends on the von Kármán constant $\kappa = 0.4$, the mean lapse rate between the SBL top and lowest grid point $\Delta \langle \theta \rangle / \Delta z$, and the bulk Richardson number Ri_B defined as

$$Ri_B = \frac{\frac{g}{\langle \theta_0 \rangle} \frac{\Delta \theta}{\Delta z}}{\left(\frac{\Delta \langle u \rangle}{\Delta z} \right)^2 + \left(\frac{\Delta \langle v \rangle}{\Delta z} \right)^2}, \tag{4.2}$$

where the differences are similarly calculated between the SBL top and lowest grid point.

For the results presented in Section 4.4 and unless otherwise stated, we utilize the full volumetric fields for analysis. In Section 4.4.5 we additionally employ output from a virtual tower centered in the domain at $(x, y, z) = (L_x/2, L_y/2, z)$ that emulates measurements from eddy-covariance systems at each domain height z sampling at 50 Hz for timeseries analysis (see Salesky and Anderson, 2018; Greene and Salesky, 2022).

Table 4.2: Values of various simulation parameters. Values in parentheses indicate those for the spinup time period.

Parameter	Description	Units	Value
L_x, L_y, L_z	Domain dimensions	m	800, 800, 400
n_x, n_y, n_z	Number of grid points	-	192, 192, 192
			(96, 96, 96)
Δ_x, Δ_y, Δ_z	Grid resolution	m	4.17, 4.17, 2.08
			(8.33, 8.33, 4.17)
$\Delta_f = (\Delta_x \Delta_y \Delta_z)^{1/3}$	Characteristic filter width	m	3.31 (6.61)
Δ_t	Time step	s	0.02 (0.04)
U_g, V_g	Geostrophic wind components	m s^{-1}	8, 0
f	Coriolis parameter	s^{-1}	1.318×10^{-4}
z_0	Aerodynamic roughness length	m	0.10
z_{0h}	Roughness length for heat	m	0.10
z_{inv}	Height of initial inversion	m	100
Γ_{inv}	Initial inversion lapse rate	K m^{-1}	0.01

4.3 Ability of LES to resolve SBL dynamics

Before reviewing the results for this chapter, it is worth discussing the performance of our LES model with regards to resolving the finescale dynamics for increasing stable stratification. In this context it is interesting to consider the Ozmidov scale L_O (Dougherty, 1961; Ozmidov, 1965), which is defined based on the mean TKE dissipation rate ϵ and the Brunt–Väisälä frequency N as

$$L_O = \sqrt{\frac{\epsilon}{N^3}}. \tag{4.3}$$

The Ozmidov scale has the physical interpretation of being the largest eddy size unaffected by buoyancy, and has been shown to be the characteristic size of momentum transporting eddies within the SBL (Bou-Zeid et al., 2010; Li et al., 2016). Li et al. (2016) found that L_O actually constrains the energy-production end of the inertial subrange under increasing stability. Sullivan et al. (2016) discuss the importance of explicitly resolving this scale when using LES, as typical SGS models are dissipative and are not designed to effectively emulate the small-scale overturnings when $L_O < \Delta_f$. Because they utilize a fine mesh grid of $\Delta_f = 0.39$ m, this is only an issue close to the surface and near the top of the SBL. With coarser resolution, as considered in this chapter (as well as Chapter 3), this is a more significant issue. Huang and Bou-Zeid (2013) address this explicitly, noting that when the LES filter scale lies within the inertial subrange, it is imperative for the SGS model to correctly drain fluxes and TKE from the resolved to SGS scales to produce correct fluxes. They further argue that the LASD SGS model has proven capable of this difficult task, and has superior performance to traditional Smagorinsky-Lily or scale-invariant models (Bou-Zeid et al., 2005). We therefore can maintain reasonable confidence in the ability of our LES model setup to reproduce accurate total fluxes in the SBL. As will be discussed

further, heightened caution will be necessary when considering spectral analysis of only the resolved velocity and temperature fields, as it is not always possible to include the SGS contributions with these analyses.

Profiles of L_O relative to the grid scale Δ_f are presented in Figure 4.1a. For these cases we define TKE dissipation rate for LES as the energy flux across the filter scale (Pope, 2000) based on the subgrid stress tensor τ_{ij} and the filtered strain rate tensor $\widetilde{S}_{ij}$ such that $\epsilon = -\langle \tau_{ij} \widetilde{S}_{ij} \rangle$. It is apparent that L_O is explicitly resolved in at least 80% of the SBL for cases A–D, but this proportion decreases with increasing stability. In case H, $L_O(z) < \Delta_f$ for the entire SBL, decreasing to a value of $L_O/\Delta_f \approx 0.2$ near the top of the SBL.

With such a reliance on the SGS model when simulating the SBL, it is also useful to consider the ratios of the SGS fluxes to the total (resolved + SGS) fluxes. Profiles of these ratios for momentum and heat fluxes are included in Figure 4.1b and c, respectively. As expected, this ratio is large across all cases close to the wall, but in the middle of the SBL the ratios increase monotonically with stability and cluster into two primary groups. The ratios of SGS momentum and heat fluxes for cases A–D remain at or below 20% for $0.1 < z/h < 0.6$, whereas cases E–H are in the 25–60% range within this region. In proximity to the LLJ, these ratios begin to increase with height across all cases for momentum and especially heat fluxes. As in Huang and Bou-Zeid (2013), we believe that although these ratios are large at higher stabilities, the LASD SGS model employed in this chapter should be capable of reproducing accurate flux profiles. Greene and Salesky (2022) (see Section 4.3) performed a grid sensitivity study using these same cases, and concluded that the grid size only had marginal impacts on the total flux profiles, even at the highest stability considered (their case F, which is equivalently case H in this chapter). It was found that the largest sensitivity to grid size
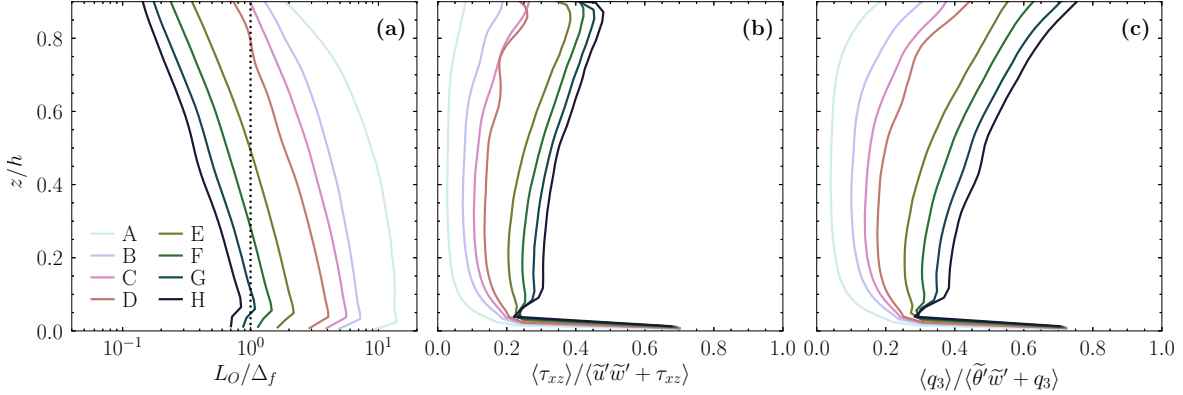
Figure 4.1: Profiles of the (a) ratio of the Ozmidov scale L_O to the LES characteristic filter size Δ_f (in log coordinates), and ratios of subgrid (b) momentum and (c) heat flux to the total (resolved + SGS) fluxes for all simulations A–H.

came from consideration of integral lengthscales, which depend wholly on the resolved fields and do not incorporate SGS contributions. Therefore, for the remainder of this chapter, we will primarily consider cases A–D for analysis when it is not reasonable to include the SGS terms, and references to cases E–F are for reference.

4.4   Results

4.4.1   Mean profiles and instantaneous fields

Profiles of mean quantities from cases A–H over the final hour of simulation are included in Figure 4.2. The mean wind speed profile $U_h = \sqrt{\langle\widetilde{u}\rangle^2 + \langle\widetilde{v}\rangle^2}$ (Figure 4.2a) generally displays a low-level jet (LLJ) for each simulation for $0.8 < z/h < 1$, with the maximum speed increasing with stability. The mean potential temperature profiles $\Theta = \langle\widetilde{\theta}\rangle$ (Figure 4.2b) display a strong sensitivity to the surface cooling rate, as mean lapse rates increase monotonically from cases A–H. The normalized root-mean square velocity $u_{rms} = \sqrt{0.5(\widetilde{u'^2} + \widetilde{v'^2} + \widetilde{w'^2})}$ (Figure 4.2c) generally decreases with stability likely due in part to the buoyant suppression of turbulence kinetic energy (TKE) with increasing

stability. The enhancement of u_{rms} at higher stability may be signatures of intermittent turbulence or could also be related to inertial oscillations due Coriolis forcing (Holton, 2004).

Profiles of the gradient Richardson number (Figure 4.2g),

$$Ri_g = \frac{g}{\Theta_0} \frac{\partial \Theta}{\partial z} \left[\left(\frac{\partial \langle \widetilde{u} \rangle}{\partial z} \right)^2 + \left(\frac{\partial \langle \widetilde{v} \rangle}{\partial z} \right)^2 \right]^{-1}, \tag{4.4}$$

also increase monotonically with surface cooling rate for a given height. The weakly-stable cases are largely within the subcritical regime associated with Kolmogorov turbulence, $Ri_g < 0.2$, as identified by Grachev et al. (2013), whereas simulation H lies entirely above this threshold for $z/h > 0.1$. Finally, the mean profiles of nondimensional total (resolved + SGS) momentum and heat flux (Figure 4.2d,e) generally collapse, although the weakly stable cases A and B are more linear than the rest as they are closer to neutral stratification. The irregularities in the lowest grid points for these profiles can be attributed to the wall model. An analysis comparing these mean profiles with those from longer averaging periods (not shown), namely 1.5 and 2 hr, indicate only marginal differences and provide confidence in the quasi-stationarity of the simulations during this one hour period.

To visually highlight coherent structures within these SBL flows, in Figure 4.3 we present horizontal and vertical cross-sections of the instantaneous fluctuating stream-wise velocity and potential temperature fields from simulations A and E. Inspection of the horizontal (xy) cross-section of $\widetilde{u}'/u_*$ located at $z/h = 0.05$ (Figure 4.3a,b) indicate elongated streaks of high and low momentum that decrease in size and magnitude with stability. In simulation A (Figure 4.3a) these streaks are of O(h) in length and are rotated with respect to the geostrophic wind (Table 4.2). This is analogous to how
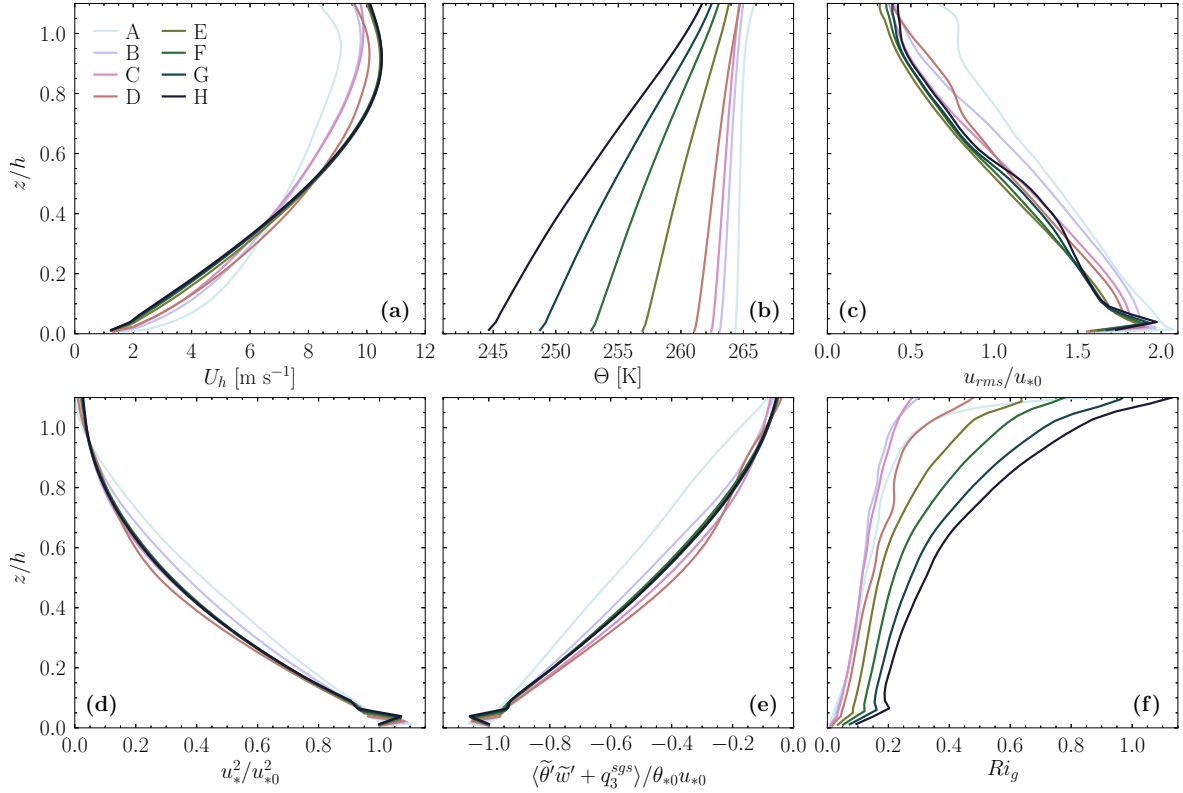
Figure 4.2: Mean profiles from all simulations A–H of (a) wind speed $U_h = \sqrt{\langle\widetilde{u}\rangle^2 + \langle\widetilde{v}\rangle^2}$, (b) potential temperature $\Theta = \langle\widetilde{\theta}\rangle$, (c) root mean square velocity $u_{rms} = \sqrt{0.5(\widetilde{u'^2} + \widetilde{v'^2} + \widetilde{w'^2})}$, (d) total momentum flux u_*^2 (Equation 4.1), (e) total potential temperature flux, and (f) gradient Richardson number Ri_g. Statistics are calculated using the final hour of each simulation.
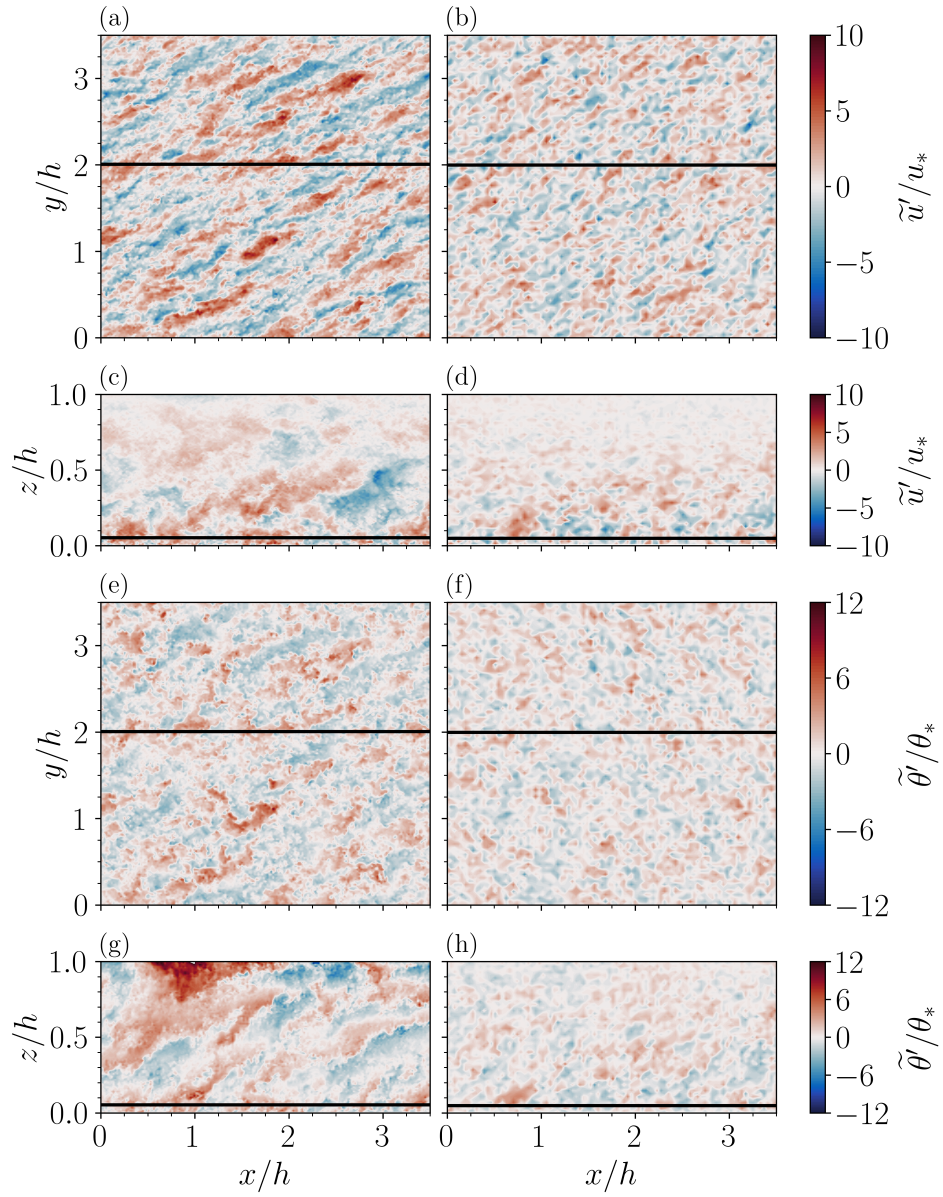
Figure 4.3: Instantaneous cross-sections from simulations A (left column) and E (right column) including: xy plane at $z/h = 0.05$ of (a,b) streamwise velocity perturbations, (e,f) potential temperature perturbations, and xz plane at $y/h = 2$ of (c,d) streamwise velocity perturbations and (g,h) potential temperature perturbations. The spanwise cross-sections in panels (c,d,g,h) are denoted as horizontal black lines in panels (a,b,e,f) for reference, and the line plotted in (c,d,g,h) denotes $z/h = 0.05$.

HCRs in the CBL are typically rotated $\approx$15–20° to the left of the geostrophic wind due to surface drag and momentum flux divergence (e.g., Salesky et al., 2017, and references therein). Ansorge and Mellado (2014) include discussion of these features within stably stratified turbulent flows, but is otherwise beyond the scope of this chapter. With increasing stability, in case E (Figure 4.3b) the velocity field is organized into fine ribbons of weaker fluctuations than in case A, and areas of locally similar magnitudes are less well-defined.

Unlike streamwise velocity, the horizontal cross-sections of potential temperature fluctuations (Figure 4.3e,f) do not demonstrate corresponding elongated streaks. This result is strikingly different than what is found in the convective boundary layer (Salesky et al., 2017), where the velocity and potential temperature fields are visually analogous. Instead, the potential temperature field is comprised of a patchy network of warm and cold pockets whose magnitudes depend on stability. In case A, there are a few locations where seemingly organized patches of temperature overlap with the long streaks in velocity, e.g., around $(x/h \approx 1, y/2 \approx 2)$ (there is actually a similar correspondence at the same coordinates for case E). It is clear, however, that the frequency of these overlapping patterns is lower in case E than for case A.

Finally, it is apparent from the vertical cross sections located at $y/h = 2$ (Figure 4.3c,d) that the elongated velocity streaks extend into the vertical under weak stability. For example, between $0.75 < x/h < 2.5$, a region of $\widetilde{u}'/u_* > 0$ extends from the surface up to $z/h \approx 0.5$. These dimensions ($\Delta x/h \approx 1.75$, $\Delta z/h \approx 0.5$) correspond to an inclination angle of $\gamma = \arctan(0.5/1.75) = 15.9°$ with respect to the surface, which agrees well with the values based on two-point correlation statistics as presented by Gibbs et al. (2022) under weak stable stratification. With increasing stability, however, analogous structures do not appear within the flow (Figure 4.3f). The vertical cross sections of potential temperature fluctuations (Figure 4.3g,h) highlight

similar features as those from the streamwise velocity fluctuations. In case A, there are elongated regions of high and low perturbations with sharp boundaries in between, which is highly reminiscent of the temperature microfronts presented by Sullivan et al. (2016). It is apparent by examining the warm anomaly attached to the surface around $x/h \approx 0.75$ (corresponding to the one discussed in Figure 4.3c) that the temperature structures do not necessarily incline at the same relative angles as for momentum. As will be discussed further, this eludes to differing mechanisms for vertical transport of heat and momentum under stable stratification. The overall spatial correlation between the momentum and temperature fluctuations in this region align with a sweep of relatively warmer, high momentum fluid moving towards the surface.

From an analysis of the instantaneous fields presented in Figure 4.3, it is clear that buoyancy acts to suppress vertical organization more strongly than in the horizontal. This will be important to consider when analyzing the results in the following sections.

4.4.2 Spectrograms

One common method for identifying the presence of coherent structures within turbulent flows is through the analysis of spectrograms (Hutchins and Marusic, 2007a; Mathis et al., 2009a; Anderson, 2016; Baars et al., 2017; Salesky and Anderson, 2018). Spectrograms are premultiplied power spectra presented as functions of both wavelength and height above the surface, and evidence for large-scale motions exists when an outer peak at large scales is present. Included in Figure 4.4 are spectrograms for cases A–E of streamwise and vertical velocities, potential temperature, and cospectra for uw as well as θw.

Inspection of Figure 4.4 reveals distinct inner and outer peaks in case A across all parameters. In case A (Figure 4.4a,f,k,p,u), the outer peak is located approximately
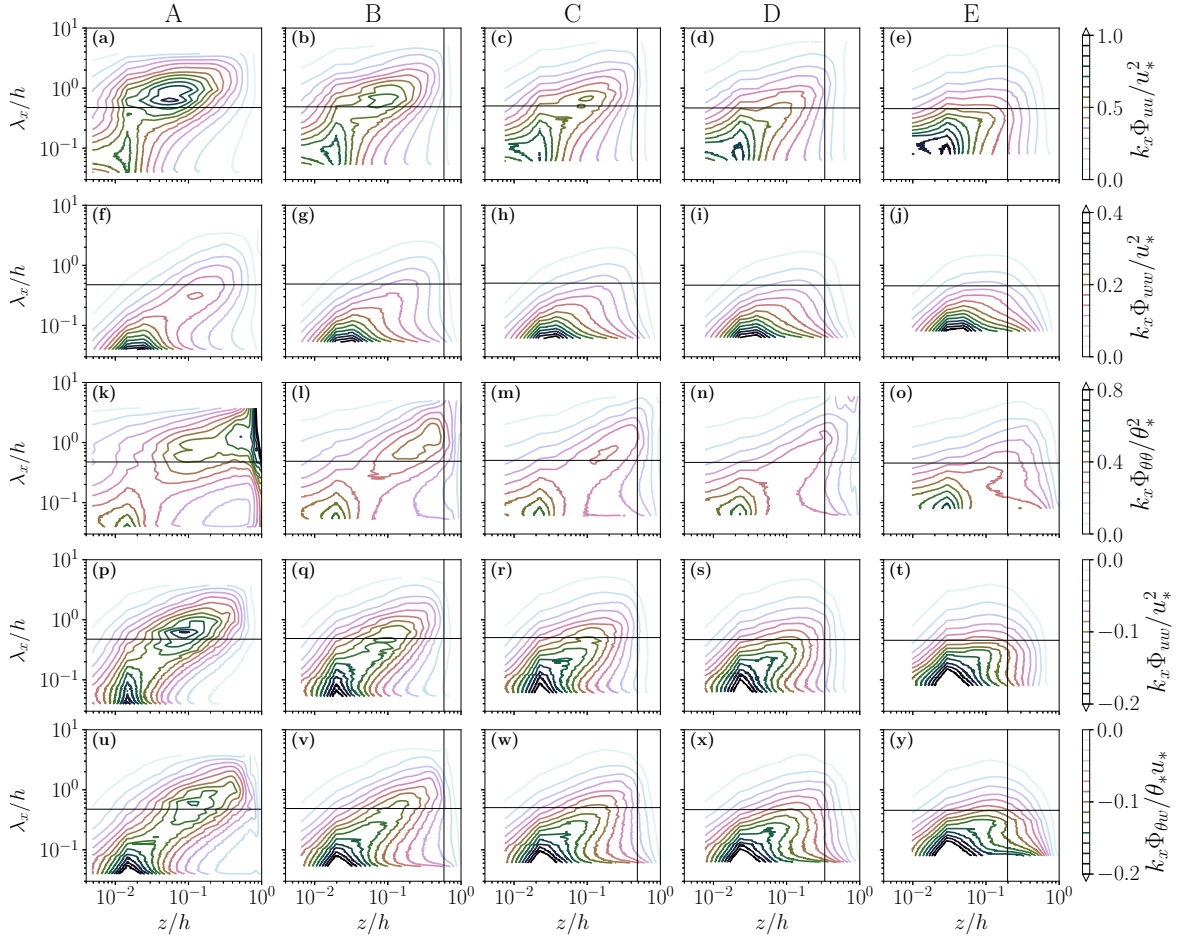
Figure 4.4: Premultiplied spectrograms from simulations A–E (columns) for (a–e) streamwise velocity, (f–j) vertical velocity, (k–o) potential temperature, as well as cospectra for (p–t) uw and (u–y) θw. Each is plotted versus streamwise wavelength λ_x and wall-normal height z normalized by the SBL depth h. Horizontal lines at $\lambda_x = z_j/2$ indicate the cutoff frequency utilized in the decoupling procedure outlined in Section 4.4.5 that roughly separates the inner and outer peaks (where they exist). Vertical lines at plotted for $z = L$ to indicate the Obukhov length from each case.

at $z/h \approx 0.1$ and $\lambda_x/h \approx 0.8$, which is as expected within the logarithmic/outer region of the wall-bounded flow at streamwise wavelengths approximately scaling with the boundary layer depth. These scales are slightly smaller than those reported by, e.g., Baars et al. (2017) for neutrally-stratified channel flow, but roughly an order of magnitude smaller than those in the convective boundary layer reported by Salesky and Anderson (2018). These differences may likely be due to the lack of very large-scale motions in the domain considered, so energy peaks at the scale of individual coherent structures instead of a collective superstructure.

For increasing stability, the outer peaks in all of the spectrograms considered attenuate until they disappear entirely. This behavior, specifically in streamwise velocity (Figure 4.4a–e), is also in contrast with the findings of Salesky and Anderson (2018), who found that within the CBL, the peak distinctly moved toward smaller wavelengths until it merged with the inner peak with increasing instability. This is undoubtedly the signature of buoyant suppression of vertical motions, which has been shown to act at the large scales (García-Villalba and del Álamo, 2011) so that large eddies do not traverse the full depth of the SBL. Recall from the discussion in Section 4.3 and from the results of Li et al. (2016) that the Ozmidov scale is a characteristic eddy size within the SBL that denotes the beginning of the inertial subrange. Since L_O increases with stability, this implies that the inertial subrange shifts towards higher wavenumbers as energy carried by large eddies is damped by buoyancy. This notion is further supported by the lack of outer peak in vertical velocity beyond case A (Figure 4.4f–j), although a noticeable ridge does extend from the surface towards larger scales and heights in cases B–D. The combined effect of these results is evident in the uw cospectra (Figure 4.4p–t), indicating a declining correlation between u and w with stability. The outer peak in the potential temperature spectrogram $k_x \Phi_{\theta\theta}/\theta_*^2$ (Figure 4.4k–o) notably is higher in the SBL and occurs at longer wavelengths than those for u and w for each case. For

example, in case B (Figure 4.4l) this peak is centered on $z/h \approx 0.3, \lambda_x/h \approx 15$. More-over, the ridge in the potential temperature spectrogram persists through at least case D in similar fashion to the u spectrograms. Finally, there appears to be an outer peak in the θw cospectra $k_x \Phi_{\theta w}/\theta_* u_*$ (Figure 4.4u–y) only for case A. These differences in momentum and scalar spectrograms indicate underlying differences in their respective transports, which will be discussed further in Section 4.4.4.

From these spectrograms, it is apparent that buoyancy acts strongly to attenuate vertical motions at large streamwise wavelengths, resulting in turbulence that is increasingly local with increasing stability. There is evidence that velocity and potential temperature organize into coherent structures through at least through case C (recall from Table 4.1 that $C_r = 0.33$ K h^{-1}, $h/L = 2.06$) based on the presence of outer peaks. In Section 4.4.3 we explore further how these fields are affected by stability across scales.

4.4.3 Linear coherence spectra

In addition to spectrograms, another method of diagnosing the relevant scales affected by coherent structures is through computation of the linear coherence spectrum (LCS; Baars et al., 2017). The LCS is a measure of the linear coupling between variables across scales, and is defined as

$$\gamma_{uu}^2(z, z_R; \lambda_x) = \frac{|\langle \hat{u}(z; \lambda_x)\hat{u}^*(z_R; \lambda_x)\rangle|^2}{\langle|\hat{u}(z; \lambda_x)|^2\rangle\langle|\hat{u}(z_R; \lambda_x)|^2\rangle}, \tag{4.5}$$

where $\hat{u}(z; \lambda_x) = \mathcal{F}\{u(x, y, z)\}$ is the Fourier transform of $u(x, y, z)$ along the stream-wise dimension with the asterisk $*$ denoting its complex conjugate, and z_R represents a constant reference height above ground level for comparison against all heights z. The angle brackets $\langle\rangle$ indicate an ensemble average across the spanwise dimension y and

time for the final hour of each simulation, and $||$ refers to the modulus of a complex value. In this context, γ_{uu}^2 falls within the range $0 \le \gamma_{uu}^2 \le 1$, and can be interpreted as the squared value of the correlation coefficient at a specific scale λ_x between fluctuating values of u at two different heights z and z_R. An example of this is included in Figure 4.5, where we calculate γ_{uu}^2, γ_{ww}^2, and $\gamma_{\theta\theta}^2$ using a reference height z_R as the lowest gridpoint in each simulation. The strongest coupling across all simulations and parameters is noticeably found at horizontal wavelengths of O(h), as was found with the outer peaks in the premultiplied spectrograms in the previous section. Moreover, the vertical extent of the LCS peaks diminishes with increasing stability. For example, γ_{uu}^2 for case A extends well beyond $z/h = 0.1$ whereas by case D the contour for $\gamma_{uu}^2 = 0.1$ only extends to $z/h \approx 0.05$. The γ_{uu}^2 and $\gamma_{\theta\theta}^2$ peaks for case A (Figure 4.5a,k) can also be attributed to the coherent features identified in the instantaneous fields that extend from the surface up into the outer region of the flow (Figure 4.3a,e). We note here that due to vertical resolution limitations using a wall-modeled LES, the contours near the surface do not provide significant amounts of information at higher stabilities. Baars et al. (2017) argue that a 1:1 slope of these peaks in log-log coordinates, specifically in streamwise velocity under near-neutral stratification (case A), is consistent with the attached-eddy hypothesis (Townsend, 1976) across a self-similar hierarchy of scales. Analysis of these cases in the framework of the attached-eddy hypothesis is beyond the scope of this chapter, but certainly warrants further investigation, ideally with higher resolutions close to the wall.

It is also possible to define Equation 4.5 for two independent variables at the same height, which provides information on the coupling of two parameters across scales. The LCS between u and w for example would be determined as
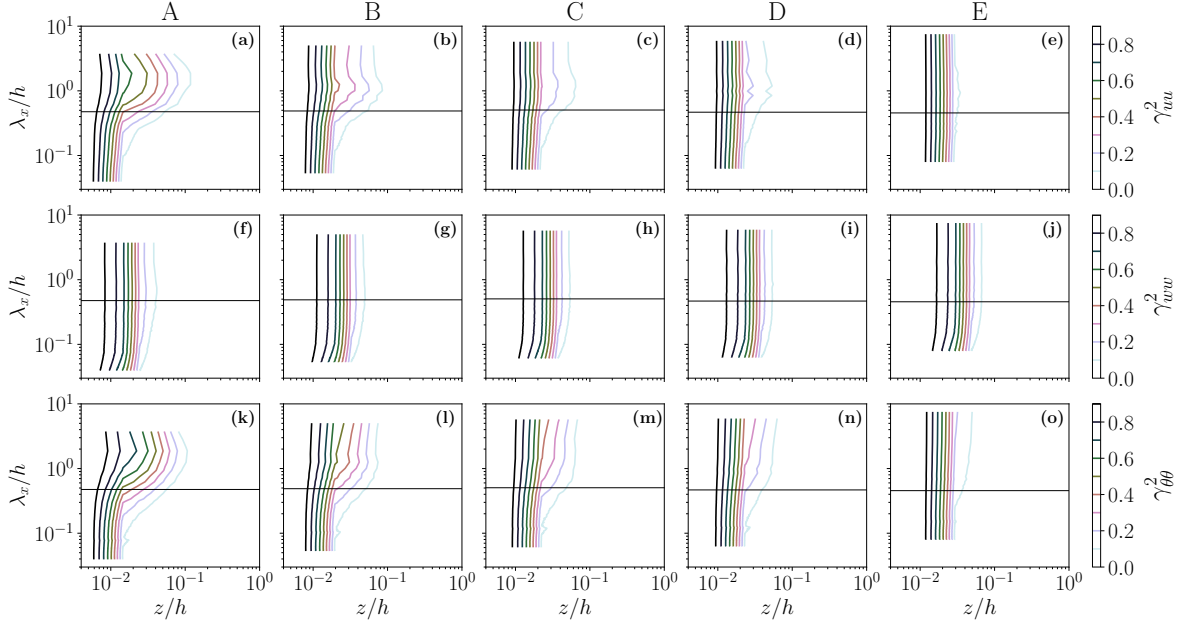
Figure 4.5: Linear coherence spectra for (a–e) u, (f–j) w, and (k–o) θ for cases A–E (columns) calculated with the reference point z_R as the lowest gridpoint and plotted against nondimensional wavelength and wall-normal distance. The horizontal line in each panel is the same as in Figure 4.4.

$$\gamma_{uw}^2(z; \lambda_x) = \frac{|\langle \hat{u}(z; \lambda_x) \hat{w}^*(z; \lambda_x) \rangle|^2}{\langle |\hat{u}(z; \lambda_x)|^2 \rangle \langle |\hat{w}(z; \lambda_x)|^2 \rangle}. \tag{4.6}$$

The resulting values of γ_{uw}^2 and $\gamma_{\theta w}^2$ are included in Figure 4.6 for cross-sections at constant heights z/h within the SBL. Low in the boundary layer ($z/h = 0.2$, Figure 4.6a) it is apparent that the coupling between u and w is strongest for $\lambda_x/h > 0.5$ in cases A–D. This coupling becomes increasingly scale-invariant with stability as indicated by a flattening of the γ_{uw}^2 curves. A different pattern is observed for $\gamma_{\theta w}^2$ at $z/h = 0.2$ (Figure 4.6d), with distinct relative maxima that is generally centered around $\lambda_x/h \approx 0.5$ across all stabilities. For vertical transport of potential temperature at this height, the impacts from buoyancy are noticeable in the attenuation of $\gamma_{\theta w}^2$ with increasing stability at larger scales ($\lambda_x/h > 0.5$).

121

In the middle of the SBL at $z/h = 0.5$ (Figure 4.6b), u and w are again most strongly linked at large wavelengths, with the γ^2_{uw} peak moving towards smaller wavelengths with increasing stability. This transition is noticeable as a peak in case A for $\lambda_x/h \approx 20$ and tailing off for small wavelengths. In cases B–D this peak becomes wider and its center shifts towards smaller scales, and cases E–F have distinct peaks around $\lambda_x/h \approx 0.3$ that tail off towards higher wavelengths. Cases E–F largely differ in magnitude, monotonically decreasing across scales with stability. The coupling between θ and w at this height (Figure 4.6e) follow a similar pattern at large wavelengths, but for $\lambda_x/h < 0.2$ cases E–F actually demonstrate higher values of $\gamma^2_{\theta w}$ than for cases A–D. These results again reflect how buoyancy negatively affects vertical transport of both momentum and heat at large scales, but the differences in γ^2_{uw} and $\gamma^2_{\theta w}$ at fine scales allude to differing transport mechanisms.

Finally, near the top of the SBL (but still below the LLJ) at $z/h = 0.8$, γ^2_{uw} is generally smaller across all scales than it is closer to the wall (Figure 4.6c). There are broad peaks in all cases generally centered around $\lambda_x/h \approx 0.5$ and spanning most of the considered scales, with overall magnitudes generally decreasing with stability. This likely is related to the relative lack of turbulent momentum flux near the top of the SBL (see Figure 4.2d) with strongly increasing local stability as indicated by Ri_g (Figure 4.2f). One can identify that $\gamma^2_{\theta w} > \gamma^2_{uw}$ at this level across all cases and scales (Figure 4.6c,f), although both become increasingly scale-invariant with stability. It appears in general, however, that temperature is more efficiently transported than momentum for greater local and global stabilities. This topic is discussed in further detail in Section 4.4.4.
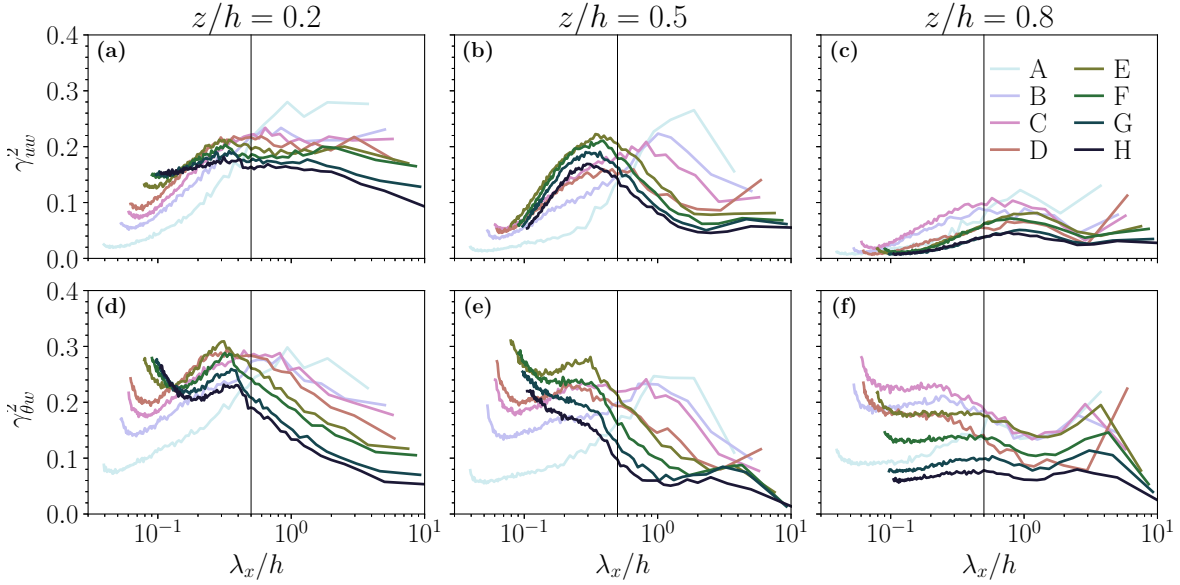
Figure 4.6: Cross-sections of LCS from cases A–H at constant heights: (a,d) $z/h = 0.2$, (b,e) $z/h = 0.5$, and (c,f) $z/h = 0.8$ for (a–c) γ^2_{uw} and (d–f) $\gamma^2_{\theta w}$. Vertical lines at $\lambda_x/h = 0.5$ are included for reference.

4.4.4   Transport efficiency

In Section 4.4.2 we identified the existence of an outer peak in the premultiplied spectrograms in cases A–C, and in Section 4.4.3 found enhanced linear coupling at the scales of these outer peaks. Previous studies of the convective boundary layer have shown that turbulent transports of momentum and scalars become increasingly dissimilar with increasing instability (Li and Bou-Zeid, 2011; Dupont and Patton, 2012; Patton et al., 2016), and Salesky et al. (2017) were able to connect these differences to varying modes of convective organization. However, the relationships between momentum and heat transport in stably-stratified turbulent shear flows remain relatively unexplored. To study these effects, it is useful to consider the partitioning of turbulent fluxes into contributions by individual positive and negative fluctuations in either term. This technique is known as quadrant analysis (also conditional sampling; see Wallace,

2016, and references therein), and is outlined as follows. Using the resolved vertical momentum flux $\langle \widetilde{u}'\widetilde{w}' \rangle$ as an example, we define the four quadrants as

- Quadrant I: $\widetilde{u}' > 0, \widetilde{w}' > 0$

- Quadrant II: $\widetilde{u}' < 0, \widetilde{w}' > 0$

- Quadrant III: $\widetilde{u}' < 0, \widetilde{w}' < 0$

- Quadrant IV: $\widetilde{u}' > 0, \widetilde{w}' < 0$

With this definition, quadrants II and IV are respectively referred to as ejections and sweeps. The quadrants for potential temperature flux are defined likewise by replacing u with θ, and for stable thermal stratification quadrants II and IV also refer to the downgradient direction. The turbulent transport efficiencies based on these quadrants are defined based on the fraction of the total flux occurring in the downgradient direction (Wyngaard and Moeng, 1992; Li and Bou-Zeid, 2011; Salesky et al., 2017). For the SBL where $\partial U_h / \partial z > 0$ and $\partial \Theta / \partial z > 0$, the transport efficiencies for momentum and heat are defined (adopting the notation of the present article) as

$$\eta_{uw} = \frac{\langle \widetilde{u}'\widetilde{w}' \rangle}{\langle \widetilde{u}'\widetilde{w}' \rangle^{\mathrm{II}} + \langle \widetilde{u}'\widetilde{w}' \rangle^{\mathrm{IV}}} \qquad (4.7)$$

and

$$\eta_{\theta w} = \frac{\langle \widetilde{\theta}'\widetilde{w}' \rangle}{\langle \widetilde{\theta}'\widetilde{w}' \rangle^{\mathrm{II}} + \langle \widetilde{\theta}'\widetilde{w}' \rangle^{\mathrm{IV}}}. \qquad (4.8)$$

Here the superscripts II and IV refer to the individual quadrant contributions to the total flux from specifically quadrants II and IV. Note that we intentionally neglect the SGS flux contributions in Equations 4.7 and (4.8) for use with LES output, as the quadrant assignment for, e.g., τ_{xz} is not directly discernible from the signs of $\widetilde{u}'$ and $\widetilde{w}'$.
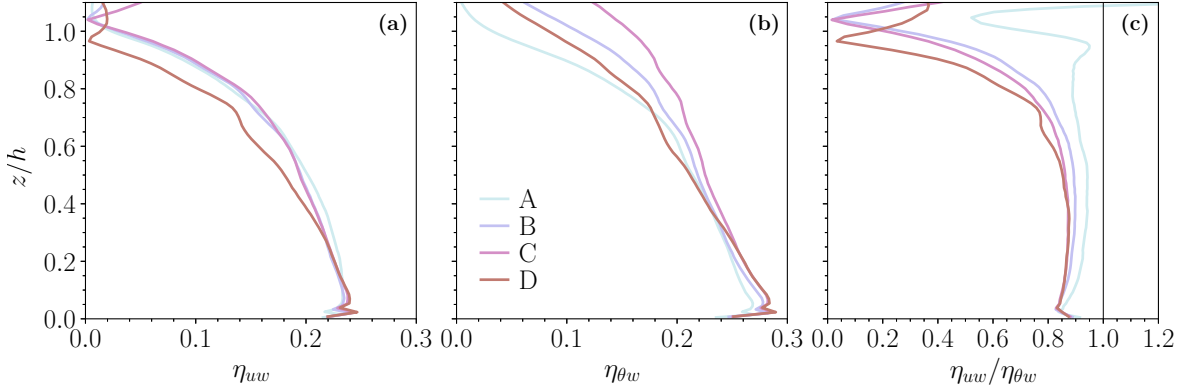
Figure 4.7: Profiles of transport efficiencies (a) η_{uw} (Equation 4.7), (b) $\eta_{\theta w}$ (Equation 4.8), and (c) their ratio $\eta_{uw}/\eta_{\theta w}$ for cases A–D. The vertical line in (c) denotes a ratio of 1.

Profiles of these transport efficiencies along with their ratio are included in Figure 4.7. Here we choose only to consider cases A–D because with increasing stability, the fraction of unresolved fluxes throughout the SBL becomes relevant when comparing the transport efficiencies defined in Equations 4.7 and 4.8 without SGS contributions. Recall from Figure 4.1b,c that the SGS fluxes comprise an appreciable fraction of the total fluxes for cases E–F. There is a noticeable dependence on stability for both η_{uw} and $\eta_{\theta w}$ that is most apparent in the profile of their ratio (Figure 4.7c). The ratio $\eta_{uw}/\eta_{\theta w}$ is close to unity throughout the SBL for case A, and generally decreases with stability. This effect is generally due to the combination of decreasing η_{uw} and increasing $\eta_{\theta w}$ with stability, with case D seemingly affected the strongest for $z/h > 0.5$. The momentum transport efficiencies trend towards zero near the top of the SBL at a height roughly corresponding to the U_h maximum in the LLJ (see Figure 4.2a). Interestingly, the heat transport efficiencies do not follow the same pattern but instead decrease at roughly constant rates throughout the depth of the SBL (except for case A, which decreases more rapidly above $z/h > 0.6$). Overall, the transport efficiencies in both momentum and heat are markedly lower than those reported in both observed and simulated CBLs at weak instability (e.g., Li and Bou-Zeid, 2011; Salesky et al., 2017).

Therefore it is apparent that even weak stratification plays a strong role in inhibiting flow's ability to vertically redistribute momentum or heat.

These differences in transport efficiencies can be traced to changes in turbulent motions from each quadrant I–IV as displayed in Figure 4.8. Plotted are the individual quadrant fractions Q_{uw}^k and $Q_{\theta w}^k$, which we define as

$$Q_{uw}^k = \frac{|\langle \widetilde{u}' \widetilde{w}' \rangle^k|}{\sum |\langle \widetilde{u}' \widetilde{w}' \rangle^k|} \tag{4.9}$$

and

$$Q_{\theta w}^k = \frac{|\langle \widetilde{\theta}' \widetilde{w}' \rangle^k|}{\sum |\langle \widetilde{\theta}' \widetilde{w}' \rangle^k|}, \tag{4.10}$$

where $k \in \{$I, II, III, IV$\}$ represents the individual quadrant contributions to the absolute sum.

Recalling that quadrants II and IV in the momentum flux (Figure 4.8b,d) denote ejections and sweeps, respectively, it is apparent that motions in these quadrants dominate the total flux profile with quadrant fractions Q_{uw}^{II}, $Q_{uw}^{\mathrm{IV}} > 0.25$ for all cases A–D. The fraction of ejections remains roughly constant with height for each case for $0.1 < z/h < 0.8$, whereas the sweeps decrease with height in this range. In upper half of the SBL, the fraction of ejections decreases with stability, and the fluxes are primarily compensated for in the countergradient motions of quadrant I (Figure 4.8a). The differences in quadrants III and IV (Figure 4.8c,d) are comparatively smaller with changes in stability, indicating that changes in transport efficiency largely depend on how positive vertical motions interact with relatively high or low streamwise momentum parcels within the SBL. At the top of the SBL, all four quadrants reach equilibrium with an even distribution of $Q_{uw}^k = 0.25$. The same does not occur for the heat fluxes, however, with quadrants II and IV dominating the contributions at all levels (Figure 4.8f,h).
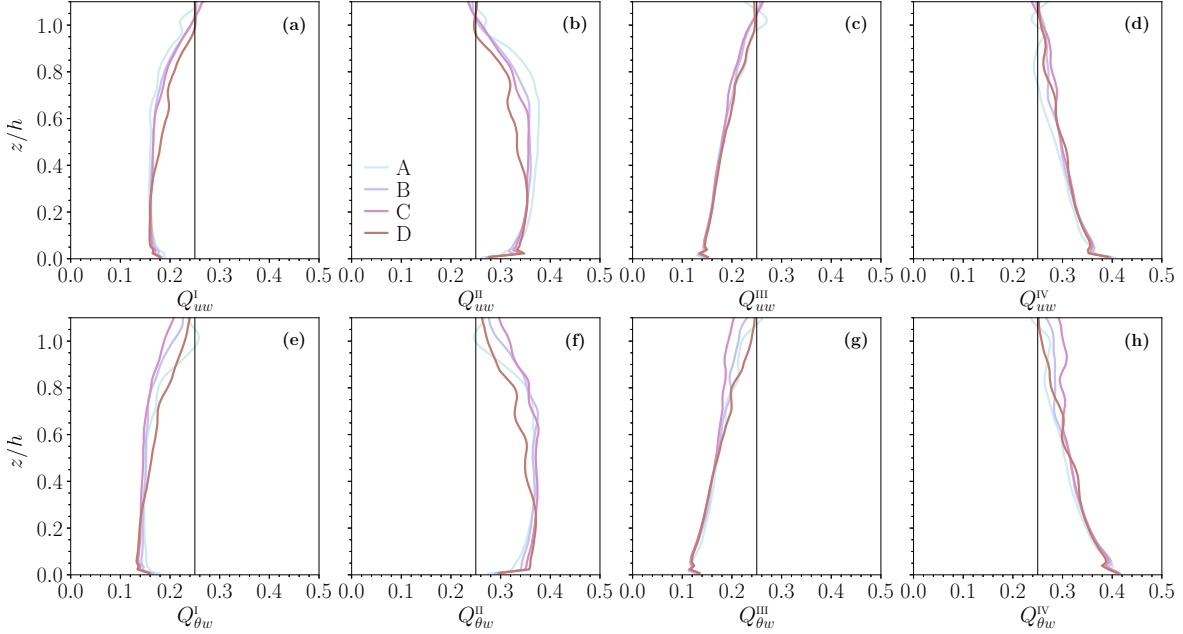
Figure 4.8: Individual quadrant fractions (a–d) Q_{uw}^k (Equation 4.9) and (e–h) $Q_{\theta w}^k$ (Equation 4.10) for cases A–D.

Otherwise the general trends in the heat flux quadrant fractions are largely similar to those of momentum fluxes: ejections (upwelling relatively cold parcels) are relatively constant with height whereas sweeps decrease with height, and the countergradient components (Figure 4.8e,g) primarily depend on stability above $z/h > 0.5$.

It is apparent from the turbulent transfer efficiencies (Figure 4.7) and individual quadrant fractions (Figure 4.8) that momentum and heat are transported differently as stability increases. Under weakly stable stratification (case A), our results generally match those from Li and Bou-Zeid (2011) and Salesky et al. (2017) under weakly unstable conditions. Therefore it is likely that coherent turbulent structures such as hairpin vortices exist in case A (Adrian, 2007), but increasing stratification flattens motions into largely horizontal features. Vertical motions become more localized and contributions from countergradient fluxes reduce the overall efficiencies in turbulent transport of both momentum and heat. This is also consistent with the small-scale

127

circulations around microfronts in the SBL as observed by Sullivan et al. (2016) from their high-resolution LES.

4.4.5   Amplitude modulation

To further examine how large-scale motions affect the smaller scales within the SBL, in this section we perform the decoupling procedure outlined by Mathis et al. (2009a) and more recently by Salesky and Anderson (2018). The decoupling procedure as implemented with single-point correlations is summarized as follows.

First we consider two random variables $a = a(z;t)$ and $b = b(z;t)$. We are interested in computing the extent to which the large scales of signal b at height z modulate the small-scale amplitude of signal a also at height z. To extract the large-scale components of these signals a_l and b_l, we lowpass filter each such that $a_l(z;t) = G * a(z;t)$ where G is the impulse response function of a sharp spectral filter that is convolved with a. For the present chapter we define the filter function to have a cutoff wavelength equal to half the height of the LLJ, $\lambda_c = z_j/2$, which generally is in the range separating the inner and outer peaks in the premultiplied spectrograms (Figure 4.4). We further extract the small-scale component of each signal as $a_s(z;t) = a(z;t) - a_l(z;t)$.

The next step involves a Hilbert transform $\mathcal{H}$, which for the small-scale signal a_s is defined as

$$\mathcal{A}_s(t) = \mathcal{H}\{a_s(t)\} = \frac{1}{\pi}\mathcal{P}\int_{-\infty}^{+\infty}\frac{a_s(\tau)}{t-\tau}\mathrm{d}\tau, \tag{4.11}$$

where $\mathcal{P}$ is the Cauchy principal value of the integral for time shift τ. Mathematically, Equation 4.11 is the convolution integral between $a_s(t)$ and the quantity $1/\pi t$ such that $\mathcal{A}_s(t) = a_s(t) * (1/\pi t)$. From the fundamental properties of the Hilbert transform

(Mathis et al., 2009a; Bendat and Piersol, 2010), $a_s(t)$ and $\mathcal{A}_s(t)$ form a complex analytic signal $Z(t)$ such that

$$Z(t) = a_s(t) + i\mathcal{A}_s(t) = A_s(t)\mathrm{e}^{i\phi_s(t)} \tag{4.12}$$

where $A_s(t)$ and $\phi_s(t)$ are the instantaneous modulus and phase of $Z(t)$ (Sreenivasan, 1985; Tardu, 2008; Mathis et al., 2009a). The modulus $A(t)$ of the analytic signal,

$$A_s(t) = \sqrt{a_s^2(t) + \mathcal{A}_s^2(t)}, \tag{4.13}$$

represents the envelope of the original signal, $E(a_s)$. Next, we lowpass filter the envelope of a_s such that $E_l(a_s) = G * E(a_s)$, which is the final element required to determine the amplitude modulation (AM) coefficients.

The AM coefficient in this example are given as the correlation coefficient between the large-scale component of b and the large-scale component of the envelope of small-scale a, i.e.

$$R_{b_l,a_s}(z) = \frac{\langle b_l'(z;t) E_l'(a_s(z;t)) \rangle}{\sqrt{\langle b_l'^2(z;t) \rangle} \sqrt{\langle E_l'^2(a_s(z;t)) \rangle}}. \tag{4.14}$$

We note that Equation 4.14 differs from that presented by Salesky and Anderson (2018) in generality since they considered both two- and one-point statistics, whereas in this present chapter we consider only one-point AM coefficients (i.e. at the same height). Their results indicate that the one-point statistics provide a stronger signal in terms of correlations when compared with the two-point AM coefficients. Since increasing stability further limits vertical turbulent transport, we would similarly expect two-point AM coefficients in this application to be small.

For the decoupling procedure to be implemented appropriately, there needs to be adequate scale separation between the inner and outer peaks (Mathis et al., 2009a).

Investigation of Figure 4.4 indicates this condition is only met for cases A–C, with case D ($C_r = 0.50$ K h^{-1}, $h/L = 3.01$) on the fringe. For cases E–F, there was no discernable outer peak in any of the premultiplied spectrograms, and as such application of the decoupling procedure would not retain physical significance. Herein, we present results using virtual tower output at 50 Hz frequency from cases A–D with the added caveats of marginal scale separation existing in case D. In Figure 4.9 we include the AM coefficients between large-scale u_l and w_l with small-scale u_s, w_s, θ_s, $(uw)_s$, and $(\theta w)_s$. The AM coefficients are presented for each case as functions of wall-normal distance z/h to identify the role of global stability on coupling between the large and small scales. As one can discern from the amplitude modulation by large-scale u_l (Figure 4.9a–e), the largest correlations are found close to the surface, namely $z/h < 0.1$. In this region, the values of R are also positive and generally decrease with stability for a given height. Using the example of R_{u_l,u_s} (Figure 4.9a), a positive correlation can physically be interpreted as follows: the small-scale velocity u_s increases due to modulation by a high-momentum large-scale motion with $u_l > 0$, or decreases due to modulation by a low-momentum large-scale motion with $u_l < 0$. Conversely, a negative correlation implies that on average, a high-momentum LSM will act to suppress small-scale perturbations, and a low-momentum LSM will excite small-scale perturbations. For the weakly stable case A, R_{u_l,u_s} is positive near the surface, decreases towards negligible values around $z/h \approx 0.2$, and further decreases to $R_{u_l,u_s} < 0$ in the upper half of the SBL. This behavior is consistent with both the weakly convective case presented by Salesky and Anderson (2018) as well as the neutrally-stratified case by Mathis et al. (2009b). This similarity also holds for all the other AM coefficients for u_l. In terms of overall magnitude for modulations by u_l, the largest impact is observed near the top of the SBL for $R_{u_l,(uw)_s}$, which reaches values as low as -0.4 in cases A and B (Figure 4.9d). Negative coupling between large-scale streamwise velocity and

small-scale momentum flux at these heights is most likely associated with turbulence production by the LLJ.

By contrast, the AM coefficients for large-scale vertical velocity w_l (Figure 4.9f–j) are markedly smaller than those for u_l across all cases. The only non-negligible coefficients occur under weak stability (cases A and B) for coupling between w_l and the instantaneous second-order moments $(uw)_s$ and $(\theta w)_s$ (Figure 4.9i,j) in the upper half of the SBL. Even these values are modest, however, and again may likely be associated with turbulent transport within the LLJ.

There are a few core similarities and differences between the AM coefficients displayed in Figure 4.9 versus those presented by Salesky and Anderson (2018) under varying convective stratifications. First, the coupling with small-scale instantaneous momentum flux $(uw)_s$ is the largest observed among all considered combinations of parameters in both the CBL and SBL. However, under unstable conditions, the modulations by large-scale w_l were relatively unaffected by global stability, whereas they are heavily influenced by negative buoyancy in the SBL. With increasing stability, the results from Figure 4.9 indicate that amplitude modulation occurs due to large-scale u_l but not necessarily for w_l, which is also consistent with the notion that buoyancy suppresses large-scale vertical motions. These differences are explored further by considering the height-averaged AM coefficients $\overline{R}_{b_l,a_s}$, which is determined for large-scale parameter b_l and small-scale a_s as

$$\overline{R}_{b_l,a_s} = \frac{1}{h} \int_0^h R_{b_l,a_s} \mathrm{d}z. \tag{4.15}$$

We note here that as R_{b_l,a_s} is bounded on the interval $[-1,1]$, so too is the integrated value $\overline{R}_{b_l,a_s}$. The resulting values for the same combinations of large- and small-scale parameters are included in Figure 4.10. There is a clear dependence on stability for
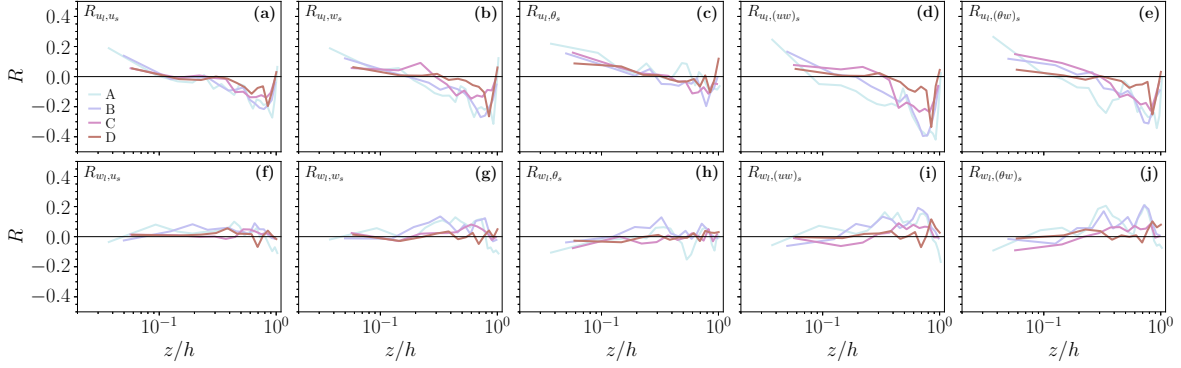
Figure 4.9: AM coefficients R from cases A–D bin-averaged versus z/h for correlations with (a–e) u_l and (f–j) w_l. Small-scale envelopes include (a,f) u_s, (b,g) w_s, (c,h) θ_s, (d,i) $(uw)_s$, and (e,j) $(\theta w)_s$.

the coupling between large-scale u_l (Figure 4.10a), whose values decrease nearly monotonically with stability. This decrease is likely due to the diminishing outer peak with increasing stability observed in Figure 4.4, since large-scale motions in general carry less energy. Moreover, this perspective makes it clear that amplitude modulation is strongest between u_l and $(uw)_s$, especially for weak stability. As observed in Figure 4.9f–j, the averaged AM coefficients of w_l (Figure 4.10b) are far smaller than those for u_l, and each are maximized for case B ($C_r = 0.25$ K h^{-1}, $h/L = 1.71$). This appears to be related to slightly higher AM coefficients in the middle of the SBL ($0.2 < z/h < 0.6$) from case B, which may indicate a region of vertical motions that draw turbulent energy more efficiently from the mean wind profile in case B than case A. Recall from Figure 4.2a that the profile of U_h demonstrates noticably larger vertical shear in the region $0.2 < z/h < 0.6$. Therefore, from the perspective of amplitude modulation, it appears that the conditions in case B offer a compromise in stability and shear production of turbulence that results in larger values of averaged AM coefficients for w_l.

In an attempt to better characterize the effects of local stability on amplitude modulation, included in Figure 4.11 are the AM coefficients plotted against Ri_g. We
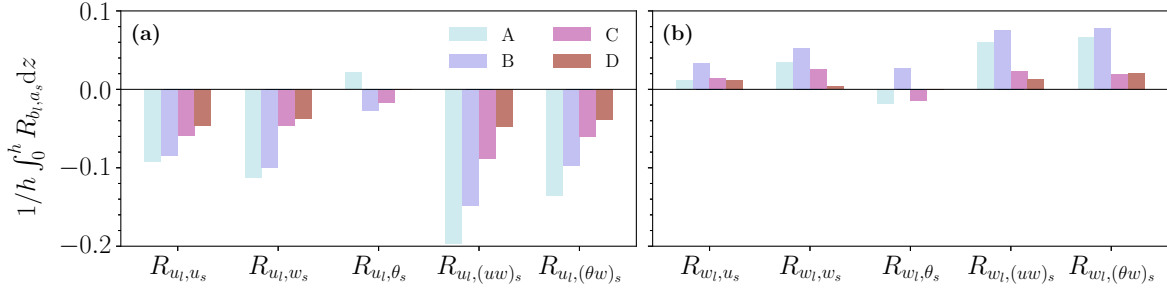
Figure 4.10: Integrated AM coefficients within the SBL for large-scale (a) u_l and (b) w_l from cases A–D.

composited all four simulations A–D and bin-averaged the AM coefficients based on evenly logarithmically spaced bins in Ri_g with vertical error bars denoting the standard deviation of each bin in Figure 4.11. It is apparent that on average, u_l positively correlates with small-scale parameters under weak local stability ($Ri_g < 0.05$, Figure 4.11a–e), and these correlations decrease and eventually become negative under higher stability ($Ri_g > 0.1$). Above the so-called critical Richardson number (Grachev et al., 2013) of around $Ri_g \approx 0.2$–0.25, the AM coefficients trend towards zero. The spread in correlations appears to increase with Ri_g, especially for the small-scale instantaneous second-order moments, although this may be an artifact of fewer points under weak stability. The correlations with large-scale w_l (Figure 4.11f–j) are virtually zero for $Ri_g > 0.03$ across all parameters.

The results following from the decoupling procedure discussed in this section are consistent with those throughout this chapter: negative buoyancy in the SBL suppresses vertical motions at large scales, forcing coherent structures to become increasingly confined to horizontal planes and at increasingly local scales (recall Figure 4.1a).
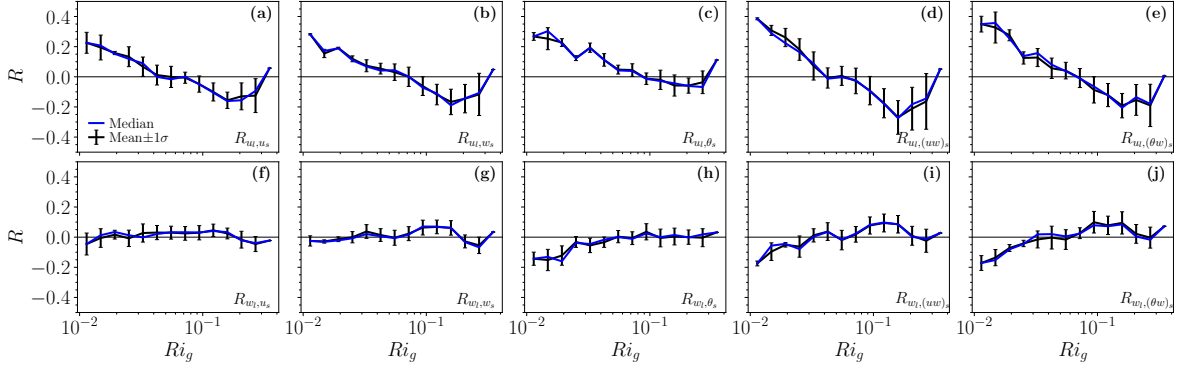
Figure 4.11: As in Figure 4.9, but composited across all cases and plotted against Ri_g. Bin medians are plotted in blue, and means in black with error bars denoting ± 1 standard deviation.

4.4.6 Conditional averaging

Large-scale motions in wall-bounded flows are commonly identified through low- and high-speed streaks in the logarithmic layer (Adrian, 2007), so it is therefore advantageous to composite snapshots of the flow when these conditions are present. This process is known as conditional sampling (Antonia, 1981), which we can define for the streamwise velocity (in notation following Salesky and Anderson, 2020, and with adapted conventions) as

$$
\frac{\widetilde{u}'^{\dagger}(\boldsymbol{x},t)}{u_*} = \left\langle \frac{\widetilde{u}'(\boldsymbol{x},t)}{u_*} \middle| \frac{\widetilde{u}'(\boldsymbol{x}_c,t)}{u_*} < -2\frac{\sigma_{\widetilde{u}'(\boldsymbol{x}_c)}}{u_*} \right\rangle_{N_{\alpha^-}}, \tag{4.16}
$$

where $\widetilde{u}'^{\dagger}(\boldsymbol{x},t)/u_*$ is the streamwise velocity averaged over N_{α^-} instances where the flow is below the threshold $\alpha^- = -2\sigma_{\widetilde{u}'(\boldsymbol{x}_c)}/u_*$ at the coordinate $\boldsymbol{x}_c = (x,y,z = 0.05h)$ and $\sigma_{\widetilde{u}'(\boldsymbol{x}_c)}$ is the standard deviation of velocity fluctuations. Here, $(\cdot)^{\dagger}$ is used to denote a conditionally-averaged variable.

Conditionally averaged streamwise velocity, vertical velocity, and potential temperature fields based on α^- in Equation 4.16 are included in Figure 4.12 for cases A–D. The effects of stability are immediately apparent in all three averaged fields, with the

134
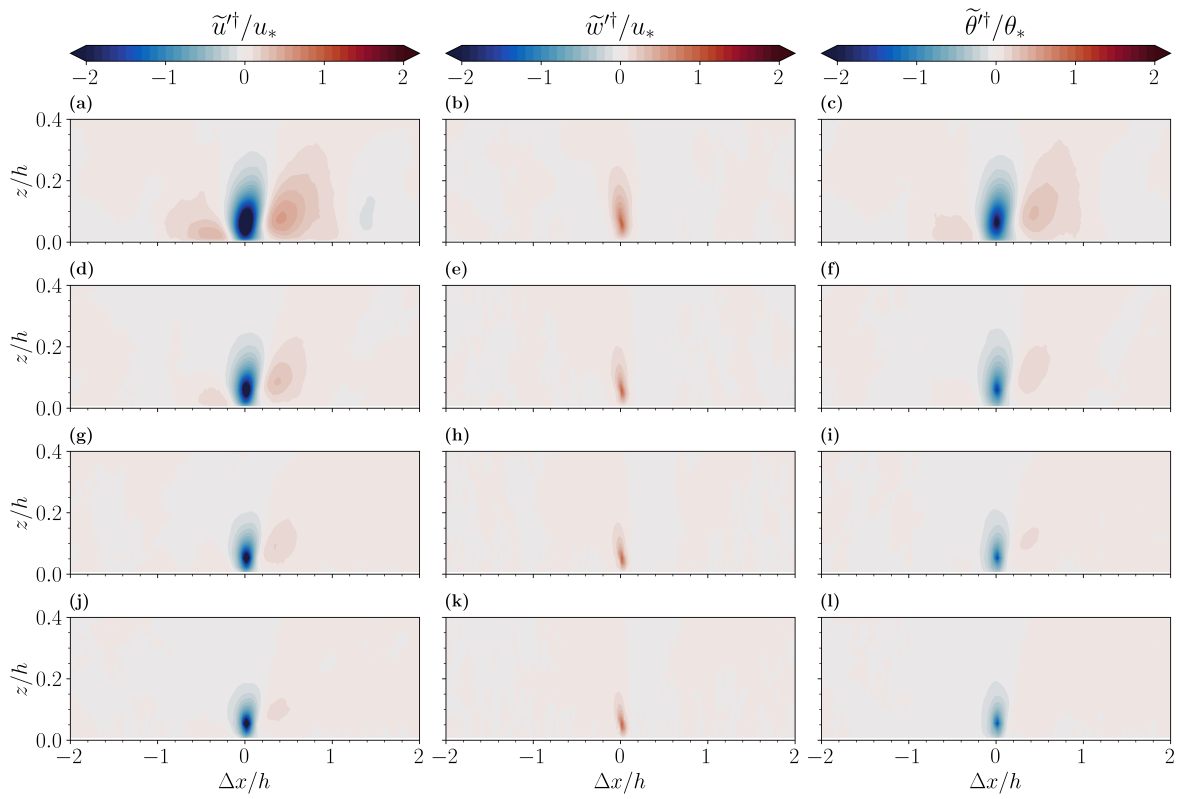
Figure 4.12: Average fields conditioned on $\widetilde{u}'/u_* < \alpha^-$ as in Equation 4.16 from simulations (a–c) A, (d–f) B, (g–i) C, and (j–l) D. Conditional fields include (a,d,g,j) $\widetilde{u}'^\dagger/u_*$, (b,e,h,k) $\widetilde{w}'^\dagger/u_*$, and (c,f,i,l) $\widetilde{\theta}'^\dagger/\theta_*$.

extent of the conditionally-averaged coherent structures diminishing in spatial extent (both horizontally and vertically) with increasing stability. In case A, the streamwise extent of the central $\widetilde{u}'^{\dagger}/u_*$ feature is $\approx 0.4h$, which corresponds well to the wavelength associated with the outer peak in the streamwise velocity spectrogram (Figure 4.4a) of $\lambda_x/h \approx 0.5$–0.6. When conditioning on low-speed streaks near the surface, the $\widetilde{u}'^{\dagger}/u_*$ minimum extends vertically up to $z/h \approx 0.3$ in case A, and is flanked by two conditional high-speed streaks that similarly appear attached to the surface (Figure 4.12a). These conditional high-speed streaks diminish under increasing stratification until the conditional low-speed streak becomes localized in space (follow Figure 4.12a,d,g,j sequentially). Combined with the evidence from the spectrograms, these results largely agree with the conceptual model of LSMs by, e.g., Marusic et al. (2010). Interestingly, the corresponding field of $\widetilde{u}'^{\dagger}/u_*$ in case A (Figure 4.12b) features a nearly vertical plume of vertical velocity directly overlaid with the low-speed streak, which highlights the dynamics of an ejection (recall Section 4.4.4) in both momentum and temperature (Figure 4.12c). The correlation between u and θ throughout the SBL is highlighted by how similarly the $\widetilde{u}'^{\dagger}/u_*$ and $\widetilde{\theta}'^{\dagger}/\theta_*$ fields evolve under increasing stability, as they are nearly identical qualitatively. This again may be related to the presence of temperature microfronts (Sullivan et al., 2016) within the SBL that concentrate gradients in velocity and temperature.

The conditionally averaged fields in Figure 4.12 are a visual representation of the statistical results presented in Sections 4.4.2–4.4.5: buoyancy suppresses large-scale vertical circulations within SBL flows. Even under weak stability, the updrafts associated with ejections do not penetrate far above the surface and are roughly 50% as wide as their corresponding low-speed streaks and cold air parcels.

Chapter 5

Summary and Conclusions

5.1 Summary of Findings

Chapters 2–4 of this dissertation sought to investigate stable boundary layer turbulence by taking advantage of recent technological advancements in observational and simulation capabilities. Specifically, this dissertation sought to answer a series of eight research questions posed in Chapter 1. This chapter summarizes the findings from Chapters 2, 3, and 4 in Sections 5.1.1, 5.1.2, and 5.1.3, respectively. Final remarks and a future outlook are included in Section 5.2.

5.1.1 Gradient-Based Similarity Scaling in the Arctic SBL

To address the gap of high-resolution observations of the SBL, Chapter 2 explores a novel method of estimating vertical profiles of turbulent statistics through a gradient-based similarity theory. We do so by synthesizing data from a surface micrometeorological tower, a ground-based Doppler lidar wind profiler, and a vertically sampling sodar to validate observations by rotary-wing UAS during the ISOBAR18 field campaign. Our primary conclusions from this analysis, as related to questions 1–2 from Chapter 1, are as follows:

1. By scaling turbulent statistics in the SBL based on local gradients of potential temperature and wind speed, we find a strong dependence on Ri that is consistent with the empirical functions defined in Sorbjan (2010, 2017). These results therefore support our hypothesis that the gradient-based similarity theory holds when filtering data to include only onshore flow to promote the likelihood of homogeneity. We also determined the following considerations to be useful in improving our results:

   - filtering observations for outliers by comparing observed Ri values with those predicted by MOST (as in e.g., Grachev et al., 2012),

   - calculating vertical gradients analytically (as opposed to finite differencing) by fitting functions of the form $y = a \ln(z)^2 + b \ln(z) + c$ to the three tower levels at each timestep.

2. To reasonably apply a similarity framework based on temporally averaged statistics to quasi-instantaneous vertical profiles from a UAS, we have identified the following key post-processing procedures (in order):

   (a) low-pass filtering raw thermodynamic sensor data and aircraft attitude angles,

   (b) time-response correction of thermodynamic measurements,

   (c) iteratively calculating new estimates of altitude based on hydrostatic balance,

   (d) regridding resulting observations to a consistently spaced vertical grid for numerical stability in calculating vertical gradients as well as averaging temporally across multiple profiles.

By following these steps, it is possible to obtain physically representative profiles of Ri from only measuring ambient temperature and horizontal winds. From this point, applying the gradient-based similarity scales produced profiles of turbulent statistics that compare reasonably well to eddy-covariance observations and revealed vertical structures of the SBL consistent with sodar observations, thereby yielding reasonable confidence in this approach. While these results from UAS scaling generally support our hypothesis posed earlier, it should be noted that nonstationary features (e.g., internal gravity waves or turbulence bursting events) may be improperly represented through temporal averaging of UAS profiles.

5.1.2 Random Errors in Novel Observations of the SBL

As UAS and eddy-covariance observations continue to demonstrate their utility for studies of the SBL, it is becoming increasingly important to characterize how well these systems can represent the stably stratified flows at larger scales. In Chapter 3 we address this issue through the lens of random error analyses of first- and second-order turbulence moments as estimated with the relaxed filtering method (Dias et al., 2018) applied to LES output. Our main findings from this chapter in the context of questions 3–5 from Chapter 1 are as follows:

3. Random errors decrease with height for all first-order moments. Errors decrease with stability for wind speed and direction, but increase for potential temperature. In general, the errors in second-order moments are smaller than those in wind speed and potential temperature, but are strongly dependent on stability.

4. The emulated UAS and eddy-covariance profiles approximate the ensemble mean reasonably well for the cases shown, and the addition of the random error bounds explicitly demonstrates the representativeness of these profiles. Moreover, the

emulated eddy-covariance profiles highlight the importance of sufficient averaging periods towards producing physically meaningful statistics.

5. Dynamically modifying the ascent rate of a UAS flying a vertical profile can be one method of decreasing the random errors in first-order quantities, especially close to the surface. Whenever possible, it would be advantageous to couple UAS operations with other ground-based sensors such as instrumented masts and remote sensors to better constrain the random errors for $z/h < 0.1$. Tradeoffs between acceptable random errors and UAS ascent rates may also be necessary with considerations for UAS battery life.

5.1.3 Coherent Strucutres in Turbulent SBL Flows

In the past half of a century, investigations of turbulent wall-bounded flows have increasingly focused on the existence and dynamics of coherent structures (e.g., Kovasznay et al., 1970; Brown and Thomas, 1977; Nakagawa and Nezu, 1981; Murlis et al., 1982; Wark and Nagib, 1991; Adrian et al., 2000; Ganapathisubramani et al., 2003; Tomkins and Adrian, 2003; Del Álamo et al., 2004; Hutchins and Marusic, 2007a; Marusic et al., 2010; Salesky and Anderson, 2018). A majority of the investigations into turbulent coherent structures have been focused on flows under neutral and unstable stratification, but recent advances in computational resources and observational techniques have enabled further studies of stably stratified flows (e.g., García-Villalba and del Álamo, 2011; Watanabe et al., 2018, 2019; Atoufi et al., 2021; Gibbs et al., 2022; Lan et al., 2018, 2019, 2022). Chapter 4 builds upon previous research by simulating a suite of eight stable atmospheric boundary layers using large-eddy simulations (Stoll et al., 2020) to examine the existence of turbulent coherent structures along with their

role in governing SBL dynamics. We analyze these SBL simulations through a synergistic combination of mean profiles, instantaneous cross-sections, premultiplied spectrograms, linear coherence spectra, turbulent transport efficiencies, amplitude modulation coefficients, and conditionally averaged fields. Our key findings as related to questions 6–8 from Chapter 1 are as follows:

6. The outer peak in premultiplied spectrograms at weak stability diminishes with increasing stability until only an inner peak remains. This is notably different than under unstable stratification, for which the outer and inner peaks actually merge at intermediate wavelengths for increasing instability (e.g., Salesky and Anderson, 2018).

7. For weak stability, the ratio between turbulent transport efficiencies of momentum and heat $\eta_{uw}/\eta_{\theta w}$ is nearly unity and is constant with height, which is consistent with observed and simulated CBLs under weak instability (e.g., Li and Bou-Zeid, 2011; Salesky et al., 2017). For increasing stability, this ratio decreases owing to a more rapid decrease in momentum transport efficiency versus only a modest decrease in heat transport. The individual transport efficiencies are also appreciably smaller in the SBL than those reported in the CBL.

8. In Section 4.4.1, we observe the existence of low- and high-speed streaks at weak stability, a telltale signature of canonical large-scale motions. These features decrease in coherence with increasing stability in conjunction with the attenuation of outer peaks in the spectrograms (Section 4.4.2). Analysis of linear coupling between flow parameters across scales in Section 4.4.3 indicates that increasing stratification limits the vertical extent of coherent structures in the SBL. Without the added flux contributions by large-scale motions, vertical turbulent transport efficiencies decay for both momentum and heat with increasing stability

(Section 4.4.4). By decomposing the simulated flows into large and small scales in Section 4.4.5, we find that under increasing stability, horizontal motions remain correlated across scales whereas vertical motions are buoyantly suppressed throughout the SBL. Finally, by conditionally averaging on the presence of low-speed streaks near the surface in Section 4.4.6, the resulting vertical cross-sections of u, w, and θ indicate the clear presence of LSMs under weak stability that are largely consistent with the conceptual models proposed in the literature (e.g., Marusic et al., 2010; Baars et al., 2017; Salesky and Anderson, 2018). Under increasing stratification, however, these coherent structures decrease in streamwise and vertical extent, and their intensities are attenuated.

5.2 Discussion and Future Outlook

One key takeaway from Chapter 2 is the potential application of gradient-based similarity scaling as a diagnostic tool in future ABL studies. Rotary-wing UAS technology offer a relatively inexpensive and flexible solution to collecting valuable atmospheric observations, and the success of gradient-based similarity scaling offers great utility from a simple thermodynamic sensor payload. For example, using this method as a diagnostic tool to evaluate the SBL height (estimated from Ri) and the vertical extent of turbulent exchange around the LLJ could be invaluable to the wind energy industry. Additionally, this method could provide a possible validation technique for near-surface mixing in NWP forecasts.

While we presented three case studies for analysis here, further research is needed to better characterize the strengths and limitations of the application of gradient-based similarity theory with UAS data. Some conditions that need to be addressed include the following: flows over heterogeneous and complex terrain, averaging over

contemporaneous UAS vertical profiles instead of or in addition to temporal averaging, an objective method to determine SBL height that can help address the validity of $L_s = \ell = \kappa z/(1 + \frac{\kappa z}{\lambda_0} + \frac{\kappa z}{\lambda_1})$ as a scaling parameter, comparisons with a shear-based scale set (as opposed to the one presented here based largely on thermal stratification), near-surface effects of UAS propeller wash on their ability to sample in stably-stratified flow, comparing observed profiles of turbulent statistics to high-resolution models such as LES or single-column models, and an evaluation of the representativeness of vertical UAS profiles compared with the surrounding SBL flow. Additionally, the effects of coherent structures on the ability of MOST to accurately describe SBL flows is an ongoing area of investigation. The presence of wall-attached eddies (Townsend, 1976) within the SBL transitioning to a z-less scaling regime is important for numerical weather and climate models to properly parameterize. The prediction of turbulent drag and momentum transport in wall-bounded flows additionally has wide applications within the fluid dynamics literature.

With the growing success of UAS-based ABL studies, it is imperative to understand how their fine-scale observations represent the surrounding flow. The results from Chapter 3 offer perspective on this issue through a random error analysis, but it is also important to recall that random errors are independent from errors arising due to instrument biases, imprecision, dynamic response, etc. At present, it is not clear how these error sources compound quantitatively. Since results indicate that random errors can be of the same order of magnitude as the other sources mentioned, they should therefore receive careful considerations in the context of NWP, data assimilation, and other general investigations of the SBL. We additionally acknowledge that only a limited parameter space was considered in this study, which is due in part to

computational expense. Future work would ideally include iterations over model configurations such as flow over complex terrain and heterogeneous surface conditions to broaden this parameter space.

Results from Chapter 4 elucidate how vertical motions are unable to penetrate far beyond their initial levels, resulting in turbulence that is disproportionately horizontal. Further increasing stability acts to suppress turbulence in all directions, with characteristic motions becoming increasingly local in scale and weak in magnitude. While these conclusions are consistent with literature, we acknowledge the imperfect nature of LES as a tool to study stably stratified flows at high Reynolds numbers. Strong stability results in characteristic motions that are often at or below the model resolution, which causes the LES to lean heavily on its subgrid model. Depending on the choice and implementation of one's SGS model, it is important to consider the relative contributions of SGS fluxes to the total flux profile when simulating the SBL. In Appendix 1 we performed a grid resolution experiment and concluded that the first- and second-order turbulent moments converged adequately, thus providing reasonable confidence in the accuracy of the simulated total flux profiles in all cases. That being said, further studies that better capture the spectrum of turbulent motions under moderate to high stability are certainly warranted (see discussion in Maronga and Li, 2021).

This dissertation has highlighted how the synergy between observations and simulations can be greater than the sum of their parts. Results from Chapter 2 highlighted the utility of continual profiling by UAS within the SBL. As demonstrated in Chapter 3, LES can be a powerful tool for informing future observation-based studies utilizing UAS within the SBL. In addition to contextualizing observations with spatial and temporal flow evolutions, simulations can also identify key features within flows that warrant further investigation. For example, Al-Ghussain and Bailey (2022) developed novel flight stragies for a fleet of fixed- and rotary-wing UAS to sample coherent structures

within the ABL. By continuing to leverage these UAS sampling strategies along with other instrumentation techniques, the existence and behavior of LSMs within the SBL can continue to be examined in the context of the results presented in Chapter 4.

Reference List

Adrian, R. J., 2007: Hairpin vortex organization in wall turbulence. *Physics of Fluids*, **19 (4)**, 041 301, https://doi.org/10.1063/1.2717527.

Adrian, R. J., C. D. Meinhart, and C. D. Tomkins, 2000: Vortex organization in the outer region of the turbulent boundary layer. *Journal of Fluid Mechanics*, **422**, 1–54, https://doi.org/10.1017/S0022112000001580.

Al-Ghussain, L., and S. C. C. Bailey, 2022: Uncrewed Aircraft System Measurements of Atmospheric Surface-Layer Structure During Morning Transition. *Boundary-Layer Meteorology*, https://doi.org/10.1007/s10546-022-00729-2.

Alaoui-Sosse, S., P. Durand, P. Medina, P. Pastor, M. Gavart, and S. Pizziol, 2022: BOREAL—A Fixed-Wing Unmanned Aerial System for the Measurement of Wind and Turbulence in the Atmospheric Boundary Layer. *J. Atmos. Oceanic Technol.*, **39 (3)**, 387–402, https://doi.org/10.1175/JTECH-D-21-0126.1.

Albertson, J. D., and M. B. Parlange, 1999: Surface length scales and shear stress: Implications for land-atmosphere interaction over complex terrain. *Water Resources Research*, **35 (7)**, 2121–2132, https://doi.org/10.1029/1999WR900094.

Anderson, W., 2016: Amplitude modulation of streamwise velocity fluctuations in the roughness sublayer: Evidence from large-eddy simulations. *Journal of Fluid Mechanics*, **789**, 567–588, https://doi.org/10.1017/jfm.2015.744.

Ansorge, C., and J. P. Mellado, 2014: Global Intermittency and Collapsing Turbulence in the Stratified Planetary Boundary Layer. *Boundary-Layer Meteorology*, **153 (1)**, 89–116, https://doi.org/10.1007/s10546-014-9941-3.

Antonia, R. A., 1981: Conditional Sampling in Turbulence Measurement. *Annual Review of Fluid Mechanics*, **13 (1)**, 131–156, https://doi.org/10.1146/annurev.fl.13.010181.001023.

Aoyama, Y., and J. Nakano, 1999: *RS/6000 SP: Practical MPI Programming*, Vol. Tech. Rep. IBM Redbook SG24-5380-00. International Business Machines.

Atlaskin, E., and T. Vihma, 2012: Evaluation of nwp results for wintertime nocturnal boundary-layer temperatures over Europe and Finland. *Q J R Meteorol Soc*, **138 (667)**, 1440–1451, https://doi.org/10.1002/qj.1885.

Atoufi, A., K. A. Scott, and M. L. Waite, 2021: Kinetic energy cascade in stably stratified open-channel flows. *Journal of Fluid Mechanics*, **925**, A25, https://doi.org/10.1017/jfm.2021.665.

Baars, W. J., N. Hutchins, and I. Marusic, 2017: Self-similarity of wall-attached turbulence in boundary layers. *Journal of Fluid Mechanics*, **823**, https://doi.org/10.1017/jfm.2017.357.

Baas, P., G. J. Steeneveld, B. J. H. van de Wiel, and A. A. M. Holtslag, 2006: Exploring self-correlation in flux-gradient relationships for stably stratified conditions. *J Atmos Sci*, **63 (11)**, 3045–3054, https://doi.org/10.1175/JAS3778.1.

Balakumar, B., and R. Adrian, 2007: Large- and very-large-scale motions in channel and boundary-layer flows. *Philosophical Transactions of the Royal Society A: Mathematical, Physical and Engineering Sciences*, **365 (1852)**, 665–681, https://doi.org/10.1098/rsta.2006.1940.

Balsley, B. B., D. A. Lawrence, D. C. Fritts, L. Wang, K. Wan, and J. Werne, 2018: Fine Structure, Instabilities, and Turbulence in the Lower Atmosphere: High-Resolution In Situ Slant-Path Measurements with the DataHawk UAV and Comparisons with Numerical Modeling. *J. Atmos. Oceanic Technol.*, **35 (3)**, 619–642, https://doi.org/10.1175/JTECH-D-16-0037.1.

Barbieri, L., and Coauthors, 2019: Intercomparison of Small Unmanned Aircraft System (sUAS) Measurements for Atmospheric Science during the LAPSE-RATE Campaign. *Sensors*, **19 (9)**, 2179, https://doi.org/10.3390/s19092179.

Barskov, K., V. Stepanenko, I. Repina, A. Artamonov, and A. Gavrikov, 2019: Two regimes of turbulent fluxes above a frozen small lake surrounded by forest. *Boundary-Layer Meteorol*, **173 (3)**, 311–320, https://doi.org/10.1007/s10546-019-00469-w.

Basu, S., A. A. M. Holtslag, B. J. H. Van De Wiel, A. F. Moene, and G.-J. Steeneveld, 2008: An inconvenient "truth" about using sensible heat flux as a surface boundary condition in models under stably stratified regimes. *Acta Geophysica*, **56 (1)**, 88–99, https://doi.org/10.2478/s11600-007-0038-y.

Beare, R. J., and Coauthors, 2006: An Intercomparison of Large-Eddy Simulations of the Stable Boundary Layer. *Boundary-Layer Meteorology*, **118 (2)**, 247–272, https://doi.org/10.1007/s10546-004-2820-6.

Beer, E., I. Eisenman, and T. J. W. Wagner, 2020: Polar Amplification Due to Enhanced Heat Flux Across the Halocline. *Geophysical Research Letters*, **47 (4)**, e2019GL086 706, https://doi.org/10.1029/2019GL086706.

Bell, T., 2021: Examining Novel Profiling Systems and Their Synergy for Advancing Boundary-Layer Research. Ph.D. thesis, University of Oklahoma.

Bell, T. M., B. R. Greene, P. M. Klein, M. Carney, and P. B. Chilson, 2020: Confronting the boundary layer data gap: Evaluating new and existing methodologies of probing the lower atmosphere. *Atmos Meas Tech*, **13 (7)**, 3855–3872, https://doi.org/10.5194/amt-13-3855-2020.

Bendat, J., and A. Piersol, 2010: *Random Data Analysis and Measurement Procedures.* Wiley.

Bevington, P., and D. Robinson, 1969: *Data Reduction and Error Analysis for the Physical Sciences.* McGraw-Hill.

Bonin, T. A., P. M. Klein, and P. B. Chilson, 2020: Contrasting Characteristics and Evolution of Southerly Low-Level Jets During Different Boundary-Layer Regimes. *Boundary-Layer Meteorology*, **174 (2)**, 179–202, https://doi.org/10.1007/s10546-019-00481-0.

Boppe, R. S., W. L. Neu, and H. Shuai, 1999: Large-Scale Motions in the Marine Atmospheric Surface Layer. *Boundary-Layer Meteorology*, **92 (2)**, 165–183, https://doi.org/10.1023/A:1001837729368.

Bou-Zeid, E., C. Higgins, H. Huwald, C. Meneveau, and M. B. Parlange, 2010: Field study of the dynamics and modelling of subgrid-scale turbulence in a stable atmospheric surface layer over a glacier. *Journal of Fluid Mechanics*, **665**, 480–515, https://doi.org/10.1017/S0022112010004015.

Bou-Zeid, E., C. Meneveau, and M. Parlange, 2005: A scale-dependent Lagrangian dynamic model for large eddy simulation of complex turbulent flows. *Physics of Fluids*, **17 (2)**, 025 105, https://doi.org/10.1063/1.1839152.

Brown, G. L., and A. S. W. Thomas, 1977: Large structure in a turbulent boundary layer. *The Physics of Fluids*, **20 (10)**, S243–S252, https://doi.org/10.1063/1.861737.

Businger, J. A., J. C. Wyngaard, Y. Izumi, and E. F. Bradley, 1971: Flux-profile relationships in the atmospheric surface layer. *J Atmos Sci*, **28 (2)**, 181–189, https://doi.org/10.1175/1520-0469(1971)028⟨0181:FPRITA⟩2.0.CO;2.

Cantwell, B. J., 1981: Organized Motion in Turbulent Flow. *Annual Review of Fluid Mechanics*, **13 (1)**, 457–515, https://doi.org/10.1146/annurev.fl.13.010181.002325.

Chilson, P. B., and Coauthors, 2019: Moving towards a Network of Autonomous UAS Atmospheric Profiling Stations for Observations in the Earth's Lower Atmosphere: The 3D Mesonet Concept. *Sensors*, **19 (12)**, 2720, https://doi.org/10.3390/s19122720.

Chinita, M. J., G. Matheou, and P. M. A. Miranda, 2022a: Large-eddy simulation of very stable boundary layers. Part I: Modeling methodology. *Quarterly Journal of the Royal Meteorological Society*, **148 (745)**, 1805–1823, https://doi.org/10.1002/qj.4279.

Chinita, M. J., G. Matheou, and P. M. A. Miranda, 2022b: Large-eddy simulation of very stable boundary layers. Part II: Length scales and anisotropy in stratified atmospheric turbulence. *Quarterly Journal of the Royal Meteorological Society*, **148 (745)**, 1824–1839, https://doi.org/10.1002/qj.4280.

Chung, D., and B. J. McKeon, 2010: Large-eddy simulation of large-scale structures in long channel flow. *Journal of Fluid Mechanics*, **661**, 341–364, https://doi.org/10.1017/S0022112010002995.

Corino, E. R., and R. S. Brodkey, 1969: A visual investigation of the wall region in turbulent flow. *Journal of Fluid Mechanics*, **37 (1)**, 1–30, https://doi.org/10.1017/S0022112069000395.

Coulter, R. L., and J. C. Doran, 2002: Spatial and temporal occurrences of intermittent turbulence during CASES-99. *Boundary-Layer Meteorol*, **105 (2)**, 329–349, https://doi.org/10.1023/A:1019993703820.

Curry, J., 1983: On the Formation of Continental Polar Air. *Journal of the Atmospheric Sciences*, **40 (9)**, 2278–2292, https://doi.org/10.1175/1520-0469(1983)040⟨2278:OTFOCP⟩2.0.CO;2.

Cuxart, J., B. Wrenger, B. Matjacic, and L. Mahrt, 2019: Spatial variability of the lower atmospheric boundary layer over hilly terrain as observed with an RPAS. *Atmosphere*, **10 (11)**, 715, https://doi.org/10.3390/atmos10110715.

Dai, Y., S. Basu, B. Maronga, and S. R. de Roode, 2021: Addressing the Grid-Size Sensitivity Issue in Large-Eddy Simulations of Stable Boundary Layers. *Boundary-Layer Meteorology*, **178 (1)**, 63–89, https://doi.org/10.1007/s10546-020-00558-1.

de Boer, G., and Coauthors, 2016: The Pilatus unmanned aircraft system for lower atmospheric research. *Atmos Meas Tech*, **9 (4)**, 1845–1857, https://doi.org/10.5194/amt-9-1845-2016.

de Boer, G., and Coauthors, 2019: Development of Community, Capabilities, and Understanding through Unmanned Aircraft-Based Atmospheric Research: The LAPSE-RATE Campaign. *Bull. Amer. Meteor. Soc.*, **101 (5)**, E684–E699, https://doi.org/10.1175/BAMS-D-19-0050.1.

de Boer, G., and Coauthors, 2020: Data generated during the 2018 LAPSE-RATE campaign: An introduction and overview. *Earth Syst. Sci. Data*, **12 (4)**, 3357–3366, https://doi.org/10.5194/essd-12-3357-2020.

de Boer, G., and Coauthors, 2022: Measurements from the University of Colorado RAAVEN Uncrewed Aircraft System during ATOMIC. *Earth Syst. Sci. Data*, **14 (1)**, 19–31, https://doi.org/10.5194/essd-14-19-2022.

Del Álamo, J. C., J. Jiménez, P. Zandonade, and R. D. Moser, 2004: Scaling of the energy spectra of turbulent channels. *Journal of Fluid Mechanics*, **500**, 135–144, https://doi.org/10.1017/S002211200300733X.

Dias, N. L., W. Brutsaert, and M. L. Wesely, 1995: Z-Less stratification under stable conditions. *Boundary-Layer Meteorology*, **75 (1)**, 175–187, https://doi.org/10.1007/BF00721048.

Dias, N. L., M. Chamecki, A. Kan, and C. M. P. Okawa, 2004: A Study of Spectra, Structure and Correlation Functions and Their Implications for the Stationarity of Surface-Layer Turbulence. *Boundary-Layer Meteorology*, **110 (2)**, 165–189, https://doi.org/10.1023/A:1026067224894.

Dias, N. L., B. L. Crivellaro, and M. Chamecki, 2018: The Hurst Phenomenon in Error Estimates Related to Atmospheric Turbulence. *Boundary-Layer Meteorology*, **168 (3)**, 387–416, https://doi.org/10.1007/s10546-018-0353-7.

Dougherty, J. P., 1961: The anisotropy of turbulence at the meteor level. *Journal of Atmospheric and Terrestrial Physics*, **21 (2)**, 210–213, https://doi.org/10.1016/0021-9169(61)90116-7.

Dupont, S., and E. G. Patton, 2012: Momentum and scalar transport within a vegetation canopy following atmospheric stability and seasonal canopy changes: The CHATS experiment. *Atmospheric Chemistry and Physics*, **12 (13)**, 5913–5935, https://doi.org/10.5194/acp-12-5913-2012.

Finkelstein, P. L., and P. F. Sims, 2001: Sampling error in eddy correlation flux measurements. *Journal of Geophysical Research: Atmospheres*, **106 (D4)**, 3503–3509, https://doi.org/10.1029/2000JD900731.

Finnigan, J., 2000: Turbulence in plant canopies. *Ann. Rev. Fluid Mech*, **32 (1)**, 519–571.

Flagg, D. D., and Coauthors, 2018: On the Impact of Unmanned Aerial System Observations on Numerical Weather Prediction in the Coastal Zone. *Mon. Wea. Rev.*, **146 (2)**, 599–622, https://doi.org/10.1175/MWR-D-17-0028.1.

Foken, T., 2006: 50 years of the Monin–Obukhov similarity theory. *Boundary-Layer Meteorol*, **119 (3)**, 431–447, https://doi.org/10.1007/s10546-006-9048-6.

Foken, T., 2008: *Micrometeorology*. Springer Berlin Heidelberg, https://doi.org/10.1007/978-3-540-74666-9.

Foken, T., F. Wimmer, M. Mauder, C. Thomas, and C. Liebethal, 2006: Some aspects of the energy balance closure problem. *Atmos Chem and Phys*, **6 (2)**, 3381–3402, https://doi.org/10.5194/acpd-6-3381-2006.

Fritz, A. M., K. Lapo, A. Freundorfer, T. Linhardt, and C. K. Thomas, 2021: Revealing the Morning Transition in the Mountain Boundary Layer Using Fiber-Optic Distributed Temperature Sensing. *Geophysical Research Letters*, **48 (9)**, e2020GL092 238, https://doi.org/10.1029/2020GL092238.

Ganapathisubramani, B., N. Hutchins, W. T. Hambleton, E. K. Longmire, and I. Marusic, 2005: Investigation of large-scale coherence in a turbulent boundary layer using two-point correlations. *Journal of Fluid Mechanics*, **524**, 57–80, https://doi.org/10.1017/S0022112004002277.

Ganapathisubramani, B., E. K. Longmire, and I. Marusic, 2003: Characteristics of vortex packets in turbulent boundary layers. *Journal of Fluid Mechanics*, **478**, 35–46, https://doi.org/10.1017/S0022112002003270.

García-Villalba, M., and J. C. del Álamo, 2011: Turbulence modification by stable stratification in channel flow. *Physics of Fluids*, **23 (4)**, 045 104, https://doi.org/10.1063/1.3560359.

Gibbs, J. A., E. Fedorovich, and A. Shapiro, 2015: Revisiting Surface Heat-Flux and Temperature Boundary Conditions in Models of Stably Stratified Boundary-Layer Flows. *Boundary-Layer Meteorology*, **154 (2)**, 171–187, https://doi.org/10.1007/s10546-014-9970-y.

Gibbs, J. A., R. Stoll, and S. T. Salesky, 2022: Inclination Angles of Turbulent Structures in Stably Stratified Boundary Layers. *Boundary-Layer Meteorology*, https://doi.org/10.1007/s10546-022-00740-7.

González-Rocha, J., S. F. J. De Wekker, S. D. Ross, and C. A. Woolsey, 2020: Wind Profiling in the Lower Atmosphere from Wind-Induced Perturbations to Multirotor UAS. *Sensors*, **20 (5)**, 1341, https://doi.org/10.3390/s20051341.

González-Rocha, J., C. A. Woolsey, C. Sultan, and S. F. J. De Wekker, 2019: Sensing Wind from Quadrotor Motion. *Journal of Guidance, Control, and Dynamics*, **42 (4)**, 836–852, https://doi.org/10.2514/1.G003542.

Grachev, A. A., E. L. Andreas, C. W. Fairall, P. S. Guest, and P. O. G. Persson, 2007: SHEBA flux–profile relationships in the stable atmospheric boundary layer. *Boundary-Layer Meteorol*, **124 (3)**, 315–333, https://doi.org/10.1007/s10546-007-9177-6.

Grachev, A. A., E. L. Andreas, C. W. Fairall, P. S. Guest, and P. O. G. Persson, 2008: Turbulent measurements in the stable atmospheric boundary layer during SHEBA: ten years after. *Acta Geophys*, **56 (1)**, 142–166.

Grachev, A. A., E. L. Andreas, C. W. Fairall, P. S. Guest, and P. O. G. Persson, 2012: Outlier problem in evaluating similarity functions in the stable atmospheric boundary layer. *Boundary-Layer Meteorol*, **144 (2)**, 137–155, https://doi.org/10.1007/s10546-012-9714-9.

Grachev, A. A., E. L. Andreas, C. W. Fairall, P. S. Guest, and P. O. G. Persson, 2013: The Critical Richardson Number and Limits of Applicability of Local Similarity

Theory in the Stable Boundary Layer. *Boundary-Layer Meteorology*, **147 (1)**, 51–82, https://doi.org/10.1007/s10546-012-9771-0.

Grachev, A. A., C. W. Fairall, P. O. G. Persson, E. L. Andreas, and P. S. Guest, 2005: Stable boundary-layer scaling regimes: The SHEBA data. *Boundary-Layer Meteorol*, **116 (2)**, 201–235, https://doi.org/10.1007/s10546-004-2729-0.

Greene, B. R., 2018: Boundary layer profiling using rotary-wing unmanned aircraft systems: Filling the atmospheric data gap. M.S. thesis, School of Meteorology, University of Oklahoma, URL https://shareok.org/handle/11244/301374.

Greene, B. R., S. T. Kral, P. B. Chilson, and J. Reuder, 2022: Gradient-Based Turbulence Estimates from Multicopter Profiles in the Arctic Stable Boundary Layer. *Boundary-Layer Meteorology*, **183 (3)**, 321–353, https://doi.org/10.1007/s10546-022-00693-x.

Greene, B. R., and S. T. Salesky, 2022: Random Errors in the Stable Boundary Layer: Implications for Modern Observational Techniques. *Journal of the Atmospheric Sciences*, **-1 (aop)**, https://doi.org/10.1175/JAS-D-22-0096.1.

Greene, B. R., A. R. Segales, T. M. Bell, E. A. Pillar-Little, and P. B. Chilson, 2019: Environmental and Sensor Integration Influences on Temperature Measurements by Rotary-Wing Unmanned Aircraft Systems. *Sensors*, **19 (6)**, 1470, https://doi.org/10.3390/s19061470.

Greene, B. R., A. R. Segales, S. Waugh, S. Duthoit, and P. B. Chilson, 2018: Considerations for temperature sensor placement on rotary-wing unmanned aircraft systems. *Atmospheric Measurement Techniques*, **11 (10)**, 5519–5530, https://doi.org/10.5194/amt-11-5519-2018.

Grossman, R. L., 1984: Bivariate Conditional Sampling of Moisture Flux over a Tropical Ocean. *Journal of the Atmospheric Sciences*, **41 (22)**, 3238–3254, https://doi.org/10.1175/1520-0469(1984)041⟨3238:BCSOMF⟩2.0.CO;2.

Guala, M., S. E. Hommema, and R. J. Adrian, 2006: Large-scale and very-large-scale motions in turbulent pipe flow. *Journal of Fluid Mechanics*, **554**, 521–542, https://doi.org/10.1017/S0022112006008871.

Head, M. R., and P. Bandyopadhyay, 1981: New aspects of turbulent boundary-layer structure. *Journal of Fluid Mechanics*, **107**, 297–338, https://doi.org/10.1017/S0022112081001791.

Higgins, C. W., M. G. Wing, J. Kelley, C. Sayde, J. Burnett, and H. A. Holmes, 2018: A high resolution measurement of the morning ABL transition using distributed temperature sensing and an unmanned aircraft system. *Environmental Fluid Mechanics*, **18 (3)**, 683–693, https://doi.org/10.1007/s10652-017-9569-1.

Hoff, R., and R. Hardesty, 2012: Thermodynamic Profiling Technologies Workshop Report to the National Science Foundation and the National Weather Service. Tech. rep., National Center for Atmospheric Research.

Högström, U., 1988: Non-dimensional wind and temperature profiles in the atmospheric surface layer: A re-evaluation. *Boundary-Layer Meteorol*, **42**, 55–78.

Holland, J. Z., 1973: A Statistical Method for Analyzing Wave Shapes And Phase Relationships of Fluctuating Geophysical Variables. *Journal of Physical Oceanography*, **3 (1)**, 139–155, https://doi.org/10.1175/1520-0485(1973)003⟨0139:ASMFAW⟩2.0.CO;2.

Holton, J. R., 2004: *An Introduction to Dynamic Meteorology.* 4th ed., Elsevier Academic Press.

Holtslag, A. a. M., and Coauthors, 2013: Stable Atmospheric Boundary Layers and Diurnal Cycles: Challenges for Weather and Climate Models. *Bull. Amer. Meteor. Soc.*, **94 (11)**, 1691–1706, https://doi.org/10.1175/BAMS-D-11-00187.1.

Houston, A. L., B. Argrow, J. Elston, J. Lahowetz, E. W. Frew, and P. C. Kennedy, 2012: The collaborative Colorado–Nebraska unmanned aircraft system experiment. *Bull Am Meteorol Soc*, **93 (1)**, 39–54, https://doi.org/10.1175/2011BAMS3073.1.

Houston, A. L., and J. M. Keeler, 2018: The impact of sensor response and airspeed on the representation of the convective boundary layer and airmass boundaries by small unmanned aircraft systems. *J Atmos Ocean Technol*, **35 (8)**, 1687–1699, https://doi.org/10.1175/JTECH-D-18-0019.1.

Houston, A. L., and J. M. Keeler, 2020: Sounding characteristics that yield significant convective inhibition errors due to ascent rate and sensor response of in situ profiling systems. *J Atmos Ocean Technol*, **37 (7)**, 1163–1172, https://doi.org/10.1175/JTECH-D-19-0191.1.

Houston, A. L., L. M. PytlikZillig, and J. C. Walther, 2021: National Weather Service Data Needs for Short-Term Forecasts and the Role of Unmanned Aircraft in Filling the Gap: Results from a Nationwide Survey. *Bull. Amer. Meteor. Soc.*, **102 (11)**, E2106–E2120, https://doi.org/10.1175/BAMS-D-20-0183.1.

Huang, J., and E. Bou-Zeid, 2013: Turbulence and Vertical Fluxes in the Stable Atmospheric Boundary Layer. Part I: A Large-Eddy Simulation Study. *J. Atmos. Sci.*, **70 (6)**, 1513–1527, https://doi.org/10.1175/JAS-D-12-0167.1.

Huang, J., E. Bou-Zeid, and J.-C. Golaz, 2013: Turbulence and Vertical Fluxes in the Stable Atmospheric Boundary Layer. Part II: A Novel Mixing-Length Model. *J. Atmos. Sci.*, **70 (6)**, 1528–1542, https://doi.org/10.1175/JAS-D-12-0168.1.

Hurst, H. E., 1951: Long-Term Storage Capacity of Reservoirs. *Transactions of the American Society of Civil Engineers*, **116 (1)**, 770–799, https://doi.org/10.1061/TACEAT.0006518.

Hutchins, N., K. Chauhan, I. Marusic, J. Monty, and J. Klewicki, 2012: Towards Reconciling the Large-Scale Structure of Turbulent Boundary Layers in the Atmosphere and Laboratory. *Boundary-Layer Meteorology*, **145 (2)**, 273–306, https://doi.org/10.1007/s10546-012-9735-4.

Hutchins, N., and I. Marusic, 2007a: Evidence of very long meandering features in the logarithmic region of turbulent boundary layers. *Journal of Fluid Mechanics*, **579**, 1–28, https://doi.org/10.1017/S0022112006003946.

Hutchins, N., and I. Marusic, 2007b: Large-scale influences in near-wall turbulence. *Philosophical Transactions of the Royal Society A: Mathematical, Physical and Engineering Sciences*, **365 (1852)**, 647–664, https://doi.org/10.1098/rsta.2006.1942.

Islam, A., A. Shankar, A. Houston, and C. Detweiler, 2021: University of Nebraska unmanned aerial system (UAS) profiling during the LAPSE-RATE field campaign. *Earth Syst. Sci. Data*, **13 (6)**, 2457–2470, https://doi.org/10.5194/essd-13-2457-2021.

Jacobs, A. M., T. M. Bell, B. R. Greene, and P. B. Chilson, 2020: The Effect of Climatological Variables on Future UAS-Based Atmospheric Profiling in the Lower Atmosphere. *Remote Sensing*, **12 (18)**, 2947, https://doi.org/10.3390/rs12182947.

Jensen, A. A., and Coauthors, 2021: Assimilation of a Coordinated Fleet of Uncrewed Aircraft System Observations in Complex Terrain: EnKF System Design and Preliminary Assessment. *Mon. Wea. Rev.*, **149 (5)**, 1459–1480, https://doi.org/10.1175/MWR-D-20-0359.1.

Jensen, A. A., and Coauthors, 2022: Assimilation of a coordinated fleet of uncrewed aircraft system observations in complex terrain: Observing System Experiments. *Monthly Weather Review*, **-1 (aop)**, https://doi.org/10.1175/MWR-D-22-0090.1.

Jensen, M. P., 2019: Tracking Aerosol Convection Interactions ExpeRiment (TRACER) Science Plan. Tech. Rep. BNL-212068-2019-INRE, 1561242, Department of Energy, BNL-212068-2019-INRE, 1561242 pp. https://doi.org/10.2172/1561242.

Jiménez, M. A., G. Simó, B. Wrenger, M. Telisman-Prtenjak, J. A. Guijarro, and J. Cuxart, 2016: Morning transition case between the land and the sea breeze regimes. *Atmos Res*, **172-173**, 95–108, https://doi.org/10.1016/j.atmosres.2015.12.019.

Jonassen, M. O., 2008: The Small Unmanned Meteorological Observer (SUMO) : Characterization and test of a new measurement system for atmospheric boundary layer research. Master's Thesis, Geophysical Institute, University of Bergen.

Joyce, K. E., K. Anderson, and R. E. Bartolo, 2021: Of Course We Fly Un-manned—We're Women! *Drones*, **5 (1)**, 21, https://doi.org/10.3390/drones5010021.

Kaimal, J. C., and J. J. Finnigan, 1994: *Atmospheric Boundary Layer Flows: Their Structure and Measurement.* Oxford University Press.

Khani, S., 2018: Mixing efficiency in large-eddy simulations of stratified turbulence. *Journal of Fluid Mechanics*, **849**, 373–394, https://doi.org/10.1017/jfm.2018.417.

Khani, S., and M. L. Waite, 2014: Buoyancy scale effects in large-eddy simulations of stratified turbulence. *Journal of Fluid Mechanics*, **754**, 75–97, https://doi.org/10.1017/jfm.2014.381.

Kim, K. C., and R. J. Adrian, 1999: Very large-scale motion in the outer layer. *Physics of Fluids*, **11 (2)**, 417–422, https://doi.org/10.1063/1.869889.

Klipp, C. L., and L. Mahrt, 2004: Flux–gradient relationship, self-correlation and intermittency in the stable boundary layer. *Q J R Meteorol Soc*, **130 (601)**, 2087–2103, https://doi.org/10.1256/qj.03.161.

Kosović, B., and J. A. Curry, 2000: A Large Eddy Simulation Study of a Quasi-Steady, Stably Stratified Atmospheric Boundary Layer. *J. Atmos. Sci.*, **57 (8)**, 1052–1068, https://doi.org/10.1175/1520-0469(2000)057⟨1052:ALESSO⟩2.0.CO;2.

Kouznetsov, R. D., 2009: The multi-frequency sodar with high temporal resolution. *Meteorol Z*, **18 (2)**, 169–173, https://doi.org/10.1127/0941-2948/2009/0373.

Kovasznay, L. S. G., V. Kibens, and R. F. Blackwelder, 1970: Large-scale motion in the intermittent region of a turbulent boundary layer. *Journal of Fluid Mechanics*, **41 (2)**, 283–325, https://doi.org/10.1017/S0022112070000629.

Kral, S., 2020: Innovative strategies for observations in the arctic atmospheric boundary layer. PhD Dissertation, University of Bergen, https://doi.org/10.13140/RG.2.2.22857.57442.

Kral, S. T., and Coauthors, 2018: Innovative strategies for observations in the arctic atmospheric boundary layer (ISOBAR)—the Hailuoto 2017 campaign. *Atmosphere*, **9 (7)**, 268, https://doi.org/10.3390/atmos9070268.

Kral, S. T., and Coauthors, 2021: The innovative strategies for observations in the arctic atmospheric boundary layer project (ISOBAR): Unique finescale observations under stable and very stable conditions. *Bull Am Meteorol Soc*, **102 (2)**, E218–E243, https://doi.org/10.1175/BAMS-D-19-0212.1.

Krautwurst, S., and Coauthors, 2021: Quantification of CH_4 coal mining emissions in Upper Silesia by passive airborne remote sensing observations with the Methane Airborne MAPper (MAMAP) instrument during the CO_2 and Methane (CoMet) campaign. *Atmospheric Chemistry and Physics*, **21 (23)**, 17 345–17 371, https://doi.org/10.5194/acp-21-17345-2021.

Kumar, V., J. Kleissl, C. Meneveau, and M. B. Parlange, 2006: Large-eddy simulation of a diurnal cycle of the atmospheric boundary layer: Atmospheric stability and scaling issues. *Water Resources Research*, **42 (6)**, https://doi.org/10.1029/2005WR004651.

Kumer, V.-M., J. Reuder, M. Dorninger, R. Zauner, and V. Grubišić, 2016: Turbulent kinetic energy estimates from profiling wind lidar measurements and their potential for wind energy applications. *Renew Energy*, **99**, 898–910, https://doi.org/10.1016/j.renene.2016.07.014.

Kumer, V.-M., J. Reuder, and B. R. Furevik, 2014: A comparison of lidar and radiosonde wind measurements. *Enrgy Proced*, **53**, 214–220, https://doi.org/10.1016/j.egypro.2014.07.230.

Lampert, A., and Coauthors, 2020: Unmanned aerial systems for investigating the polar atmospheric boundary layer—technical challenges and examples of applications. *Atmosphere*, **11 (4)**, 416, https://doi.org/10.3390/atmos11040416.

Lan, C., H. Liu, G. G. Katul, D. Li, and D. Finn, 2019: Large Eddies Regulate Turbulent Flux Gradients in Coupled Stable Boundary Layers. *Geophysical Research Letters*, **46 (11)**, 6090–6100, https://doi.org/10.1029/2019GL082228.

Lan, C., H. Liu, G. G. Katul, D. Li, and D. Finn, 2022: Turbulence Structures in the Very Stable Boundary Layer under the Influence of Wind Profile Distortion. *Journal of Geophysical Research: Atmospheres*, e2022JD036565, https://doi.org/10.1029/2022JD036565.

Lan, C., H. Liu, D. Li, G. G. Katul, and D. Finn, 2018: Distinct Turbulence Structures in Stably Stratified Boundary Layers With Weak and Strong Surface Shear. *Journal of Geophysical Research: Atmospheres*, **123 (15)**, 7839–7854, https://doi.org/10.1029/2018JD028628.

Lapo, K., A. Freundorfer, A. Fritz, J. Schneider, J. Olesch, W. Babel, and C. K. Thomas, 2022: The Large eddy Observatory, Voitsumra Experiment 2019 (LOVE19) with high-resolution, spatially distributed observations of air temperature, wind speed, and wind direction from fiber-optic distributed sensing, towers, and ground-based remote sensing. *Earth System Science Data*, **14 (2)**, 885–906, https://doi.org/10.5194/essd-14-885-2022.

Lappin, F. M., T. M. Bell, E. A. Pillar-Little, and P. B. Chilson, 2022: Low-level buoyancy as a tool to understand boundary layer transitions. *Atmospheric Measurement Techniques*, **15 (5)**, 1185–1200, https://doi.org/10.5194/amt-15-1185-2022.

Launiainen, J., and T. Vihma, 1990: Derivation of turbulent surface fluxes — An iterative flux-profile method allowing arbitrary observing heights. *Environmental Software*, **5 (3)**, 113–124, https://doi.org/10.1016/0266-9838(90)90021-W.

Lee, J. H., and H. J. Sung, 2011: Very-large-scale motions in a turbulent boundary layer. *Journal of Fluid Mechanics*, **673**, 80–120, https://doi.org/10.1017/S002211201000621X.

Lee, X., W. J. Massman, and B. E. Law, 2004: *Handbook of micrometeorology: a guide for surface flux measurement and analysis.* Atmospheric and oceanographic sciences library, Kluwer Academic Publishers, https://doi.org/10.1007/1-4020-2265-4.

Lenschow, D. H., J. Mann, and L. Kristensen, 1994: How Long Is Long Enough When Measuring Fluxes and Other Turbulence Statistics? *J. Atmos. Oceanic Technol.*, **11 (3)**, 661–673, https://doi.org/10.1175/1520-0426(1994)011⟨0661:HLILEW⟩2.0.CO;2.

Li, D., and E. Bou-Zeid, 2011: Coherent Structures and the Dissimilarity of Turbulent Transport of Momentum and Scalars in the Unstable Atmospheric Surface Layer. *Boundary-Layer Meteorology*, **140 (2)**, 243–262, https://doi.org/10.1007/s10546-011-9613-5.

Li, D., S. T. Salesky, and T. Banerjee, 2016: Connections between the Ozmidov scale and mean velocity profile in stably stratified atmospheric surface layers. *Journal of Fluid Mechanics*, **797**, https://doi.org/10.1017/jfm.2016.311.

Li, X., N. Hutchins, X. Zheng, I. Marusic, and W. J. Baars, 2022: Scale-dependent inclination angle of turbulent structures in stratified atmospheric surface layers. *Journal of Fluid Mechanics*, **942**, A38, https://doi.org/10.1017/jfm.2022.403.

Lorenz, T., S. Mayer, S. T. Kral, I. Suomi, G.-J. Steeneveld, and A. a. M. Holtslag, 2022: The stable atmospheric boundary layer over snow-covered sea ice: Model evaluation with fine-scale ISOBAR18 observations. *Quarterly Journal of the Royal Meteorological Society*, **148 (745)**, 2031–2046, https://doi.org/10.1002/qj.4293.

Lumley, J., and H. Panofsky, 1964: *The Structure of Atmospheric Turbulence.* Interscience, New York.

Lüpkes, C., T. Vihma, E. Jakobson, G. König-Langlo, and A. Tetzlaff, 2010: Meteorological observations from ship cruises during summer to the central arctic: A comparison with reanalysis data. *Geophys Res Lett*, **37 (9)**, https://doi.org/10.1029/2010GL042724.

Mahesh, A., V. P. Walden, and S. G. Warren, 1997: Radiosonde temperature measurements in strong inversions: Correction for thermal lag based on an experiment at the south pole. *J Atmos Ocean Technol*, **14 (1)**, 45–53, https://doi.org/10.1175/1520-0426(1997)014⟨0045:RTMISI⟩2.0.CO;2.

Mahrt, L., 1999: Stratified Atmospheric Boundary Layers. *Boundary-Layer Meteorology*, **90 (3)**, 375–396, https://doi.org/10.1023/A:1001765727956.

Mahrt, L., and O. Acevedo, 2022: Types of Vertical Structure of the Nocturnal Boundary Layer. *Boundary-Layer Meteorology*, https://doi.org/10.1007/s10546-022-00716-7.

Mahrt, L., S. Richardson, N. Seaman, and D. Stauffer, 2012: Turbulence in the nocturnal boundary layer with light and variable winds. *Quarterly Journal of the Royal Meteorological Society*, **138 (667)**, 1430–1439, https://doi.org/10.1002/qj.1884.

Mann, J., and D. H. Lenschow, 1994: Errors in airborne flux measurements. *Journal of Geophysical Research: Atmospheres*, **99 (D7)**, 14 519–14 526, https://doi.org/10.1029/94JD00737.

Mann, J., A. Peña, F. Bingöl, R. Wagner, and M. S. Courtney, 2010: Lidar scanning of momentum flux in and above the atmospheric surface layer. *J Atmos Oceanic Technol*, **27 (6)**, 959–976, https://doi.org/10.1175/2010jtecha1389.1.

Markowski, P., and Y. Richardson, 2011: *Mesoscale Meteorology in Midlatitudes*. John Wiley & Sons.

Maronga, B., C. Knigge, and S. Raasch, 2020: An Improved Surface Boundary Condition for Large-Eddy Simulations Based on Monin–Obukhov Similarity Theory: Evaluation and Consequences for Grid Convergence in Neutral and Stable Conditions. *Boundary-Layer Meteorology*, **174 (2)**, 297–325, https://doi.org/10.1007/s10546-019-00485-w.

Maronga, B., and D. Li, 2021: An Investigation of the Grid Sensitivity in Large-Eddy Simulations of the Stable Boundary Layer. *Boundary-Layer Meteorology*, https://doi.org/10.1007/s10546-021-00656-8.

Marusic, I., and W. D. C. Heuer, 2007: Reynolds Number Invariance of the Structure Inclination Angle in Wall Turbulence. *Physical Review Letters*, **99 (11)**, 114 504, https://doi.org/10.1103/PhysRevLett.99.114504.

Marusic, I., and N. Hutchins, 2008: Study of the Log-Layer Structure in Wall Turbulence Over a Very Large Range of Reynolds Number. *Flow, Turbulence and Combustion*, **81 (1)**, 115–130, https://doi.org/10.1007/s10494-007-9116-0.

Marusic, I., R. Mathis, and N. Hutchins, 2010: Predictive Model for Wall-Bounded Turbulent Flow. *Science*, **329 (5988)**, 193–196, https://doi.org/10.1126/science.1188765.

Marusic, I., and J. P. Monty, 2019: Attached Eddy Model of Wall Turbulence. *Annual Review of Fluid Mechanics*, **51 (1)**, 49–74, https://doi.org/10.1146/annurev-fluid-010518-040427.

Mathis, R., N. Hutchins, and I. Marusic, 2009a: Large-scale amplitude modulation of the small-scale structures in turbulent boundary layers. *Journal of Fluid Mechanics*, **628**, 311–337, https://doi.org/10.1017/S0022112009006946.

Mathis, R., J. P. Monty, N. Hutchins, and I. Marusic, 2009b: Comparison of large-scale amplitude modulation in turbulent boundary layers, pipes, and channel flows. *Physics of Fluids*, **21 (11)**, 111 703, https://doi.org/10.1063/1.3267726.

Mauder, M., and T. Foken, 2015: Documentation and instruction manual of the eddy-covariance software package TK3 (update). Tech. rep., University of Bayreuth. https://doi.org/10.5281/zenodo.20349.

McClellan, J., and T. Parks, 1973: A unified approach to the design of optimum fir linear-phase digital filters. *IEEE Trans on Circuit Theory*, **20 (6)**, 697–701.

McFarquhar, G. M., and Coauthors, 2020: Current and Future Uses of UAS for Improved Forecasts/Warnings and Scientific Studies. *Bulletin of the American Meteorological Society*, **101 (8)**, E1322–E1328, https://doi.org/10.1175/BAMS-D-20-0015.1.

Meinhart, C. D., and R. J. Adrian, 1995: On the existence of uniform momentum zones in a turbulent boundary layer. *Physics of Fluids*, **7 (4)**, 694–696, https://doi.org/10.1063/1.868594.

Miller, N. B., D. D. Turner, R. Bennartz, M. D. Shupe, M. S. Kulie, M. P. Cadeddu, and V. P. Walden, 2013: Surface-based inversions above central greenland. *J Geophys Res Atmos*, **118 (2)**, 495–506, https://doi.org/10.1029/2012JD018867.

Monin, A. S., and A. M. Obukhov, 1954: Basic laws of turbulent mixing in the surface layer of the atmosphere. *Contrib. Geophys. Inst. Acad. Sci. USSR*, **151 (163)**, e187.

Moore, A., 2018: Observing system simulation experiment studies on the use of small UAV for boundary-layer sampling. M.S. thesis, School of Meteorology, University of Oklahoma.

Moore, C. J., 1986: Frequency response corrections for eddy correlation systems. *Boundary-Layer Meteorol*, **37 (1)**, 17–35, https://doi.org/10.1007/BF00122754.

Murlis, J., H. M. Tsai, and P. Bradshaw, 1982: The structure of turbulent boundary layers at low Reynolds numbers. *Journal of Fluid Mechanics*, **122**, 13–56, https://doi.org/10.1017/S0022112082002080.

Nakagawa, H., and I. Nezu, 1981: Structure of space-time correlations of bursting phenomena in an open-channel flow. *Journal of Fluid Mechanics*, **104**, 1–43, https://doi.org/10.1017/S0022112081002796.

National Academies of Sciences, Engineering, and Medicine, 2007: *Earth Science and Applications from Space: National Imperatives for the Next Decade and Beyond.* National Academies Press.

National Academies of Sciences, Engineering, and Medicine, 2018a: *The Future of Atmospheric Boundary Layer Observing, Understanding, and Modeling: Proceedings of a Workshop.* The National Academies Press, Washington, DC, https://doi.org/10.17226/25138.

National Academies of Sciences, Engineering, and Medicine, 2018b: *Thriving on Our Changing Planet: A Decadal Strategy for Earth Observation from Space.* The National Academies Press, Washington, DC, https://doi.org/10.17226/24938.

National Research Council, 2009: *Observing Weather and Climate from the Ground Up: A Nationwide Network of Networks.* The National Academies Press, Washington, DC, https://doi.org/10.17226/12540.

Nieuwstadt, F. T. M., 1984: The turbulent structure of the stable, nocturnal boundary layer. *J Atmos Sci*, **41 (14)**, 2202–2216, https://doi.org/10.1175/1520-0469(1984)041⟨2202:TTSOTS⟩2.0.CO;2.

Nieuwstadt, F. T. M., P. J. Mason, C.-H. Moeng, and U. Schumann, 1993: Large-Eddy Simulation of the Convective Boundary Layer: A Comparison of Four Computer Codes. *Turbulent Shear Flows 8*, F. Durst, R. Friedrich, B. E. Launder, F. W. Schmidt, U. Schumann, and J. H. Whitelaw, Eds., Springer, Berlin, Heidelberg, 343–367, https://doi.org/10.1007/978-3-642-77674-8_24.

Obukhov, A., 1946: Turbulence in an atmosphere with a non-uniform temperature. *Trudy Inst. Teoret. Geophys. Akad. Nauk SSSR*, **1**, 95–115, (translation in: Boundary-Layer Meteorol. 1971, 2: 7–29).

O'Connell, P., D. Koutsoyiannis, H. F. Lins, Y. Markonis, A. Montanari, and T. Cohn, 2016: The scientific legacy of Harold Edwin Hurst (1880–1978). *Hydrological Sciences Journal*, **61 (9)**, 1571–1590, https://doi.org/10.1080/02626667.2015.1125998.

Ozmidov, R., 1965: On the turbulent exchange in a stably stratified ocean. *Atmos. Ocean Phys.*, **8**, 853–860.

Patton, E. G., P. P. Sullivan, R. H. Shaw, J. J. Finnigan, and J. C. Weil, 2016: Atmospheric Stability Influences on Coupled Boundary Layer and Canopy Turbulence. *Journal of the Atmospheric Sciences*, **73 (4)**, 1621–1647, https://doi.org/10.1175/JAS-D-15-0068.1.

Peltola, O., K. Lapo, I. Martinkauppi, E. O'Connor, C. K. Thomas, and T. Vesala, 2021: Suitability of fibre-optic distributed temperature sensing for revealing mixing processes and higher-order moments at the forest–air interface. *Atmospheric Measurement Techniques*, **14 (3)**, 2409–2427, https://doi.org/10.5194/amt-14-2409-2021.

Persson, P. O. G., C. W. Fairall, E. L. Andreas, P. S. Guest, and D. K. Perovich, 2002: Measurements near the atmospheric surface flux group tower at SHEBA: Near-surface conditions and surface energy budget. *J Geophys Res Ocean*, **107 (C10)**, SHE 21–1–SHE 21–35, https://doi.org/10.1029/2000JC000705.

Pillar-Little, E. A., and Coauthors, 2021: Observations of the thermodynamic and kinematic state of the atmospheric boundary layer over the San Luis Valley, CO, using the CopterSonde 2 remotely piloted aircraft system in support of the LAPSE-RATE field campaign. *Earth Syst. Sci. Data*, **13 (2)**, 269–280, https://doi.org/10.5194/essd-13-269-2021.

Pinto, J. O., and Coauthors, 2021: The status and future of small uncrewed aircraft systems (UAS) in operational meteorology. *Bull Am Meteorol Soc*, **102 (11)**, E2121–E2136, https://doi.org/10.1175/BAMS-D-20-0138.1.

Pithan, F., and T. Mauritsen, 2014: Arctic amplification dominated by temperature feedbacks in contemporary climate models. *Nature Geoscience*, **7 (3)**, 181–184, https://doi.org/10.1038/ngeo2071.

Pope, S. B., 2000: *Turbulent Flows.* Cambridge University Press.

Prandtl, L., 1925: Bericht über untersuchungen zur ausgebildeten turbulenz. *Z Agnew Math Mech*, **5 (2)**, 136–139, https://doi.org/10.1002/zamm.19250050212.

Rajagopalan, S., and R. A. Antonia, 1979: Some properties of the large structure in a fully developed turbulent duct flow. *The Physics of Fluids*, **22 (4)**, 614–622, https://doi.org/10.1063/1.862643.

Rautenberg, A., and Coauthors, 2019: The Multi-Purpose Airborne Sensor Carrier MASC-3 for Wind and Turbulence Measurements in the Atmospheric Boundary Layer. *Sensors*, **19 (10)**, 2292, https://doi.org/10.3390/s19102292.

Reuder, J., P. Brisset, M. M. Jonassen, and S. Mayer, 2009: The small unmanned meteorological observer SUMO: A new tool for atmospheric boundary layer research. *Meteorol Z*, 141–147, https://doi.org/10.1127/0941-2948/2009/0363.

Reuder, J., M. O. Jonassen, and H. Ólafsson, 2012: The Small Unmanned Meteorological Observer SUMO: Recent developments and applications of a micro-UAS for atmospheric boundary layer research. *Acta Geophys*, **60 (5)**, 1454–1473, https://doi.org/10.2478/s11600-012-0042-8.

Sagaut, P., 2006: *Large Eddy Simulation for Incompressible Flows: An Introduction.* 2nd ed., Springer, Berlin.

Salesky, S. T., and W. Anderson, 2018: Buoyancy effects on large-scale motions in convective atmospheric boundary layers: Implications for modulation of near-wall processes. *Journal of Fluid Mechanics*, **856**, 135–168, https://doi.org/10.1017/jfm.2018.711.

Salesky, S. T., and W. Anderson, 2020: Revisiting inclination of large-scale motions in unstably stratified channel flow. *Journal of Fluid Mechanics*, **884**, https://doi.org/10.1017/jfm.2019.987.

Salesky, S. T., and M. Chamecki, 2012: Random Errors in Turbulence Measurements in the Atmospheric Surface Layer: Implications for Monin–Obukhov Similarity Theory. *J. Atmos. Sci.*, **69 (12)**, 3700–3714, https://doi.org/10.1175/JAS-D-12-096.1.

Salesky, S. T., M. Chamecki, and E. Bou-Zeid, 2017: On the Nature of the Transition Between Roll and Cellular Organization in the Convective Boundary Layer. *Boundary-Layer Meteorology*, **163 (1)**, 41–68, https://doi.org/10.1007/s10546-016-0220-3.

Salesky, S. T., M. Chamecki, and N. L. Dias, 2012: Estimating the Random Error in Eddy-Covariance Based Fluxes and Other Turbulence Statistics: The Filtering Method. *Boundary-Layer Meteorology*, **144 (1)**, 113–135, https://doi.org/10.1007/s10546-012-9710-0.

Salesky, S. T., G. G. Katul, and M. Chamecki, 2013: Buoyancy effects on the integral lengthscales and mean velocity profile in atmospheric surface layer flows. *Physics of Fluids*, **25 (10)**, 105 101, https://doi.org/10.1063/1.4823747.

Sandu, I., A. Beljaars, P. Bechtold, T. Mauritsen, and G. Balsamo, 2013: Why is it so difficult to represent stably stratified conditions in numerical weather prediction (NWP) models? *Journal of Advances in Modeling Earth Systems*, **5 (2)**, 117–133, https://doi.org/10.1002/jame.20013.

Sathe, A., and J. Mann, 2013: A review of turbulence measurements using ground-based wind lidars. *Atmos Meas Tech*, **6 (11)**, 3147–3167, https://doi.org/10.5194/amt-6-3147-2013.

Sathe, A., J. Mann, J. Gottschall, and M. S. Courtney, 2011: Can wind lidars measure turbulence? *J Atmos Ocean Technol*, **28 (7)**, 853–868, https://doi.org/10.1175/jtech-d-10-05004.1.

Sathe, A., J. Mann, N. Vasiljevic, and G. Lea, 2015: A six-beam method to measure turbulence statistics using ground-based wind lidars. *Atmos Meas Tech*, **8 (2)**, 729–740, https://doi.org/10.5194/amt-8-729-2015.

Schotanus, P., F. Nieuwstadt, and H. De Bruin, 1983: Temperature measurement with a sonic anemometer and its application to heat and moisture fluxes. *Boundary-Layer Meteorol*, **26 (1)**, 81–93, https://doi.org/10.1007/BF00164332.

Schuyler, T. J., and M. I. Guzman, 2017: Unmanned Aerial Systems for Monitoring Trace Tropospheric Gases. *Atmosphere*, **8 (10)**, 206, https://doi.org/10.3390/atmos8100206.

Segales, A. R., P. B. Chilson, and J. L. Salazar-Cerreño, 2021: A Framework for Improving Data Quality of Thermo-Hygrometer Sensors aboard Unmanned Aerial Systems for Planetary Boundary Layer Research. *Atmospheric Measurement Techniques Discussions*, 1–23, https://doi.org/10.5194/amt-2021-316.

Segales, A. R., B. R. Greene, T. M. Bell, W. Doyle, J. J. Martin, E. A. Pillar-Little, and P. B. Chilson, 2020: The CopterSonde: An insight into the development of a smart unmanned aircraft system for atmospheric boundary layer research. *Atmospheric Measurement Techniques*, **13 (5)**, 2833–2848, https://doi.org/10.5194/amt-13-2833-2020.

Shenoy, V., 2021: Observing System Simulation Experiments Using Small Unmanned Aerial Vehicles in Various Configurations to Improve High-Resolution Forecasts of Convection. M.S. thesis, School of Meteorology, University of Oklahoma.

Shupe, M., and Coauthors, 2018: The multidisciplinary drifting observatory for the study of arctic climate (MOSAIC) atmosphere science plan. Tech. Rep. DOE/SC-ARM-18-005, ARM Climate Research Facility, Pacific Northwest National Laboratory, Richland, WA.

Simó, G., D. Martínez-Villagrasa, M. A. Jiménez, V. Caselles, and J. Cuxart, 2019: Impact of the surface–atmosphere variables on the relation between air and land surface temperatures. *Meteorology and Climatology of the Mediterranean and Black Seas*, I. Vilibić, K. Horvath, and J. L. Palau, Eds., Springer International Publishing, 219–233, https://doi.org/10.1007/978-3-030-11958-4.

Smith, E. N., J. G. Gebauer, P. M. Klein, E. Fedorovich, and J. A. Gibbs, 2019: The Great Plains Low-Level Jet during PECAN: Observed and Simulated Characteristics. *Mon. Wea. Rev.*, **147 (6)**, 1845–1869, https://doi.org/10.1175/MWR-D-18-0293.1.

Smith, E. N., and Coauthors, 2021: Evaluation and Applications of Multi-Instrument Boundary-Layer Thermodynamic Retrievals. *Boundary-Layer Meteorology*, https://doi.org/10.1007/s10546-021-00640-2.

Sorbjan, Z., 1986: On similarity in the atmospheric boundary layer. *Boundary-Layer Meteorol*, **34 (4)**, 377–397, https://doi.org/10.1007/BF00120989.

Sorbjan, Z., 1988: Structure of the stably-stratified boundary layer during the SESAME-1979 experiment. *Boundary-Layer Meteorol*, **44 (3)**, 255–266, https://doi.org/10.1007/BF00116065.

Sorbjan, Z., 2010: Gradient-based scales and similarity laws in the stable boundary layer. *Q J R Meteorol Soc*, **136 (650)**, 1243–1254, https://doi.org/10.1002/qj.638.

Sorbjan, Z., 2017: Assessment of gradient-based similarity functions in the stable boundary layer derived from a large-eddy simulation. *Boundary-Layer Meteorol*, **163 (3)**, 375–392, https://doi.org/10.1007/s10546-017-0234-5.

Sorbjan, Z., and B. B. Balsley, 2008: Microstructure of turbulence in the stably stratified boundary layer. *Boundary-Layer Meteorol*, **129 (2)**, 191–210, https://doi.org/10.1007/s10546-008-9310-1.

Sorbjan, Z., and A. A. Grachev, 2010: An evaluation of the flux–gradient relationship in the stable boundary layer. *Boundary-Layer Meteorol*, **135 (3)**, 385–405, https://doi.org/10.1007/s10546-010-9482-3.

Sreenivasan, K. R., 1985: On the fine-scale intermittency of turbulence. *Journal of Fluid Mechanics*, **151**, 81–103, https://doi.org/10.1017/S0022112085000878.

Sreenivasan, K. R., A. J. Chambers, and R. A. Antonia, 1978: Accuracy of moments of velocity and scalar fluctuations in the atmospheric surface layer. *Boundary-Layer Meteorology*, **14 (3)**, 341–359, https://doi.org/10.1007/BF00121044.

Steeneveld, G.-J., 2014: Current challenges in understanding and forecasting stable boundary layers over land and ice. *Frontiers in Environmental Science*, **2**, https://doi.org/10.3389/fenvs.2014.00041.

Steeneveld, G. J., T. Mauritsen, E. I. F. de Bruijn, J. Vilà-Guerau de Arellano, G. Svensson, and A. a. M. Holtslag, 2008: Evaluation of Limited-Area Models for the Representation of the Diurnal Cycle and Contrasting Nights in CASES-99. *J. Appl. Meteor. Climatol.*, **47 (3)**, 869–887, https://doi.org/10.1175/2007JAMC1702.1.

Stoll, R., J. A. Gibbs, S. T. Salesky, W. Anderson, and M. Calaf, 2020: Large-Eddy Simulation of the Atmospheric Boundary Layer. *Boundary-Layer Meteorology*, https://doi.org/10.1007/s10546-020-00556-3.

Stull, R. B., 1988: *An Introduction to Boundary Layer Meteorology*, Vol. 13. Kluwer Academic Publishers, Dordrecht, The Netherlands.

Sullivan, P. P., T. W. Horst, D. H. Lenschow, C.-H. Moeng, and J. C. Weil, 2003: Structure of subfilter-scale fluxes in the atmospheric surface layer with application to large-eddy simulation modelling. *Journal of Fluid Mechanics*, **482**, 101–139, https://doi.org/10.1017/S0022112003004099.

Sullivan, P. P., J. C. Weil, E. G. Patton, H. J. J. Jonker, and D. V. Mironov, 2016: Turbulent Winds and Temperature Fronts in Large-Eddy Simulations of the Stable Atmospheric Boundary Layer. *J. Atmos. Sci.*, **73 (4)**, 1815–1840, https://doi.org/10.1175/JAS-D-15-0339.1.

Tardu, S. F., 2008: Stochastic synchronization of the near wall turbulence. *Physics of Fluids*, **20 (4)**, 045 105, https://doi.org/10.1063/1.2907217.

Taylor, P. C., M. Cai, A. Hu, J. Meehl, W. Washington, and G. J. Zhang, 2013: A Decomposition of Feedback Contributions to Polar Warming Amplification. *Journal of Climate*, **26 (18)**, 7023–7043, https://doi.org/10.1175/JCLI-D-12-00696.1.

Theunissen, R., A. Di Sante, M. L. Riethmuller, and R. A. Van den Braembussche, 2008: Confidence estimation using dependent circular block bootstrapping: Application to the statistical analysis of PIV measurements. *Experiments in Fluids*, **44 (4)**, 591–596, https://doi.org/10.1007/s00348-007-0418-8.

Tomkins, C. D., and R. J. Adrian, 2003: Spanwise structure and scale growth in turbulent boundary layers. *Journal of Fluid Mechanics*, **490**, 37–74, https://doi.org/10.1017/S0022112003005251.

Townsend, A., 1976: *The Structure of Turbulent Shear Flow*. Cambridge University Press.

Tritton, D., 1988: *Physical Fluid Dynamics*. 2nd ed., Oxford University Press, New York.

van de Wiel, B. J. H., A. F. Moene, W. H. De Ronde, and H. J. J. Jonker, 2008: Local Similarity in the Stable Boundary Layer and Mixing-Length Approaches: Consistency of Concepts. *Boundary-Layer Meteorology*, **128 (1)**, 103–116, https://doi.org/10.1007/s10546-008-9277-y.

van de Wiel, B. J. H., A. F. Moene, O. K. Hartogensis, H. A. R. D. Bruin, and A. a. M. Holtslag, 2003: Intermittent turbulence in the stable boundary layer over land. Part III: A classification for observations during CASES-99. *J Atmos Sci*, **60 (20)**, 2509–2522, https://doi.org/10.1175/1520-0469(2003)060⟨2509:ITITSB⟩2.0.CO;2.

van den Heever, S. C., and Coauthors, 2021: The Colorado State University Convective CLoud Outflows and UpDrafts Experiment (C3LOUD-Ex). *Bull. Amer. Meteor. Soc.*, **102 (7)**, E1283–E1305, https://doi.org/10.1175/BAMS-D-19-0013.1.

van der Linden, S. J. A., and Coauthors, 2019: Large-Eddy Simulations of the Steady Wintertime Antarctic Boundary Layer. *Boundary-Layer Meteorology*, **173 (2)**, 165–192, https://doi.org/10.1007/s10546-019-00461-4.

Vignon, E., F. Hourdin, C. Genthon, B. J. H. van de Wiel, H. Gallée, J.-B. Madeleine, and J. Beaumet, 2018: Modeling the dynamics of the atmospheric boundary layer over the antarctic plateau with a general circulation model. *J Adv Model Earth Syst*, **10 (1)**, 98–125, https://doi.org/10.1002/2017MS001184.

Virtanen, P., and Coauthors, 2020: SciPy 1.0: Fundamental algorithms for scientific computing in python. *Nat Methods*, **17**, 261–272, https://doi.org/https://doi.org/10.1038/s41592-019-0686-2.

Wake, B., 2019: A drift in the arctic. *Nat Clim Change*, **9 (10)**, 733–733, https://doi.org/10.1038/s41558-019-0597-3.

Wallace, J. M., 2016: Quadrant Analysis in Turbulence Research: History and Evolution. *Annual Review of Fluid Mechanics*, **48 (1)**, 131–158, https://doi.org/10.1146/annurev-fluid-122414-034550.

Wallace, J. M., H. Eckelmann, and R. S. Brodkey, 1972: The wall region in turbulent shear flow. *Journal of Fluid Mechanics*, **54 (1)**, 39–48, https://doi.org/10.1017/S0022112072000515.

Wark, C. E., and H. M. Nagib, 1991: Experimental investigation of coherent structures in turbulent boundary layers. *Journal of Fluid Mechanics*, **230**, 183–208, https://doi.org/10.1017/S0022112091000757.

Watanabe, T., J. J. Riley, K. Nagata, K. Matsuda, and R. Onishi, 2019: Hairpin vortices and highly elongated flow structures in a stably stratified shear layer. *Journal of Fluid Mechanics*, **878**, 37–61, https://doi.org/10.1017/jfm.2019.577.

Watanabe, T., J. J. Riley, K. Nagata, R. Onishi, and K. Matsuda, 2018: A localized turbulent mixing layer in a uniformly stratified environment. *Journal of Fluid Mechanics*, **849**, 245–276, https://doi.org/10.1017/jfm.2018.400.

Webb, E. K., G. I. Pearman, and R. Leuning, 1980: Correction of flux measurements for density effects due to heat and water vapour transfer. *Q J R Meteorol Soc*, **106 (447)**, 85–100, https://doi.org/10.1002/qj.49710644707.

Weckwerth, T. M., T. W. Horst, and J. W. Wilson, 1999: An Observational Study of the Evolution of Horizontal Convective Rolls. *Monthly Weather Review*, **127 (9)**, 2160–2179, https://doi.org/10.1175/1520-0493(1999)127⟨2160:AOSOTE⟩2.0.CO;2.

Weckwerth, T. M., J. W. Wilson, and R. M. Wakimoto, 1996: Thermodynamic Variability within the Convective Boundary Layer Due to Horizontal Convective Rolls. *Monthly Weather Review*, **124 (5)**, 769–784, https://doi.org/10.1175/1520-0493(1996)124⟨0769:TVWTCB⟩2.0.CO;2.

Weckwerth, T. M., J. W. Wilson, R. M. Wakimoto, and N. A. Crook, 1997: Horizontal Convective Rolls: Determining the Environmental Conditions Supporting their Existence and Characteristics. *Monthly Weather Review*, **125 (4)**, 505–526, https://doi.org/10.1175/1520-0493(1997)125⟨0505:HCRDTE⟩2.0.CO;2.

Wildmann, N., M. Hofsäß, F. Weimer, A. Joos, and J. Bange, 2014: MASC – a small Remotely Piloted Aircraft (RPA) for wind energy research. *Advances in Science and Research*, **11 (1)**, 55–61, https://doi.org/10.5194/asr-11-55-2014.

Willmarth, W. W., and S. S. Lu, 1972: Structure of the Reynolds stress near the wall. *Journal of Fluid Mechanics*, **55 (1)**, 65–92, https://doi.org/10.1017/S002211207200165X.

Woodcock, J. D., and I. Marusic, 2015: The statistical behaviour of attached eddies. *Physics of Fluids*, **27 (1)**, 015 104, https://doi.org/10.1063/1.4905301.

Wrenger, B., and J. Cuxart, 2017: Evening transition by a river sampled using a remotely-piloted multicopter. *Boundary-Layer Meteorol*, **165 (3)**, 535–543, https://doi.org/10.1007/s10546-017-0291-9.

Wyngaard, J. C., and O. R. Coté, 1971: The budgets of turbulent kinetic energy and temperature variance in the atmospheric surface layer. *J Atmos Sci*, **28 (2)**, 190–201, https://doi.org/10.1175/1520-0469(1971)028⟨0190:TBOTKE⟩2.0.CO;2.

Wyngaard, J. C., and O. R. Coté, 1972: Cospectral similarity in the atmospheric surface layer. *Quarterly Journal of the Royal Meteorological Society*, **98 (417)**, 590–603, https://doi.org/10.1002/qj.49709841708.

Wyngaard, J. C., and C.-H. Moeng, 1992: Parameterizing turbulent diffusion through the joint probability density. *Boundary-Layer Meteorology*, **60 (1)**, 1–13, https://doi.org/10.1007/BF00122059.

Yano, J., and M. Wacławczyk, 2021: Nondimensionalization of the atmospheric boundary-layer system: Obukhov length and Monin–Obukhov similarity theory. *Boundary-Layer Meteorol*, https://doi.org/10.1007/s10546-021-00657-7.

Zilitinkevich, S. S., 1989: Velocity profiles, the resistance law and the dissipation rate of mean flow kinetic energy in a neutrally and stably stratified planetary boundary layer. *Boundary-Layer Meteorology*, **46 (4)**, 367–387, https://doi.org/10.1007/BF00172242.

1 Appendix: Grid Convergence Tests

To investigate the effects of model grid spacing on our LES results, here we present the results from a series of grid convergence tests. The cases presented in this chapter were simulated in an $800 \times 800 \times 400$ m^3 domain with a numerical grid consisting of 192^3 total points. This was decided upon after first simulating cases A and F at additional resolutions of $96^3, 128^3, 160^3$, and 192^3 (see Table A.1). The $128^3, 160^3$, and 192^3 simulations were first run at a resolution of 96^3 for 6 physical hours before being interpolated to their final resolution and continued for another 4 physical hours. The 96^3 simulation was run for 10 total hours without interpolation.

Mean profiles of relevant quantities are plotted in Figure A.1 for case A and Figure A.2 for case F, and simulation parameters are outlined in Table A.1. The mean first-order profiles for case A (Figure A.1a–c) show clear convergence for resolutions of 128^3 and higher, whereas the second-order profiles (Figure A.1d–f) show stronger convergence at the 160^3 and higher resolutions. The 192^3 profile of normalized heat flux resides in between those from the 96^3 and the $128^3, 160^3$ resolutions, which is most pronounced for $0.4 < z/h < 0.8$, however this spread is ultimately not that large. The largest spread between resolutions for case A occurs in the normalized streamwise velocity variance profiles (Figure A.1f), with the largest difference occurring for $z/h < 0.3$. Of note for these profiles is that the dynamic Smagorinsky SGS model is only written for the deviatoric part of the SGS stress tensor, so the velocity variance components are determined as $\langle u'^2 \rangle = \langle \widetilde{u}' \widetilde{u}' \rangle$. Therefore it is not entirely surprising that the convergence of the variance profiles will depend somewhat on model resolution as increasing energy can be resolved for increasing resolutions.

Similarly, in case F there is reasonable convergence among all profiles at resolutions of 160^3 and above. The maximum wind speed within the LLJ is slightly decreased

Table A.1: Mean simulation properties for cases A and F for grid convergence. Here we include the x and z filter widths Δ_x, Δ_z, characteristic filter width $\Delta_f = (\Delta_x \Delta_y \Delta_x)^{1/3}$, timestep Δ_t, and other parameters as in Table 3.1.

Case	Resolution	Δ_x	Δ_z	Δ_f	Δ_t	h	L	h/L	u_{*0}	z_j/h
	-	(m)	(m)	(m)	(s)	(m)	(m)	-	(m s^{-1})	-
A	96^3	8.33	4.17	6.61	0.04	175	93.0	1.88	0.239	0.926
	128^3	6.25	3.12	4.96	0.02	167	91.2	1.84	0.232	0.950
	160^3	5.00	2.50	3.97	0.02	166	93.0	1.78	0.233	0.950
	192^3	4.17	2.08	3.31	0.02	160	93.5	1.71	0.231	0.976
F	96^3	8.33	4.17	6.61	0.04	99.7	7.64	13.1	0.177	0.908
	128^3	6.25	3.12	4.96	0.02	91.2	7.61	12.0	0.174	0.915
	160^3	5.00	2.50	3.97	0.02	83.4	7.47	11.2	0.170	0.950
	192^3	4.17	2.08	3.31	0.02	80.5	7.28	11.1	0.166	0.924

at the 96^3 resolution, but this appears to converge on a similar value for increasing resolutions. The 96^3 potential temperature profile in Figure A.2c appears warmer than the others, possibly due to the the limitations of the LES wall model at this relatively coarse resolution and low-level temperature gradients. The momentum and heat flux profiles demonstrate little to no dependence on resolution, which is a testament to the ability of the LASD SGS model to simulate the subgrid contributions of these terms (Bou-Zeid et al., 2005). Finally, the streamwise velocity variance profiles vary the most out of the parameters presented here, although the relatively small differences between the 160^3 and 192^3 resolutions imply a reasonable convergence.

Due to the relevance of the integral lengthscale to this chapter, in Figure A.3 are the resulting profiles of integral scales evaluated at each grid resolution for simulations A and F. For case A, in the lower half of the SBL all of the integral scales converge reasonably well at all resolutions. In the upper half of the SBL, there is some divergence

in particular for $\mathcal{L}_u$ and $\mathcal{L}_\theta$, where it is observed that higher resolutions lead to larger integral lengthscales. This can perhaps be explained by the ability of the LES to resolve turbulence produced below the LLJ at finer and finer scales, which will lead to an enhancement in coherence. In case F it is notable that the integral scales grow slowly with increasing resolution for all parameters at all heights, and especially for $\mathcal{L}_w$ (Figure A.3e) which follows fairly closely with the LES filter width for each resolution considered. This is evidence that the LES filter extends towards the peak in resolved spectral energy density, and the SGS model is heavily relied upon to model vertical transport at high stabilities. It therefore makes sense that the integral scales for case F tend to depend on LES grid resolution, as a finer grid will be able to explicitly resolve additional energy in the flow.

Overall it is apparent that the 192^3 simulations provide a sufficient level of resolution for this study of random errors within the SBL. Although studies simulating the SBL with LES have been conducted at resolutions on the order of 1024^3 (e.g., Sullivan et al., 2016; Maronga and Li, 2021), this type of model configuration is unobtainable with our current computational resources. Moreover, recent literature still reports a sensitivity to grid spacing even down to a spacing of 0.39 m wherein SBL heights continually decrease without a proper convergence (Sullivan et al., 2016; Maronga et al., 2020; Dai et al., 2021; Maronga and Li, 2021). Although Maronga and Li (2021) recently recommend simulating closer to 40 physical hours instead of 10 as in studies based off the GABLS project (Beare et al., 2006; Huang and Bou-Zeid, 2013), this is also computationally prohibitive. Regardless, for our study we believe the 192^3 resolution with $\Delta_f = 3.31$ m, when coupled with the LASD SGS model, is sufficient.
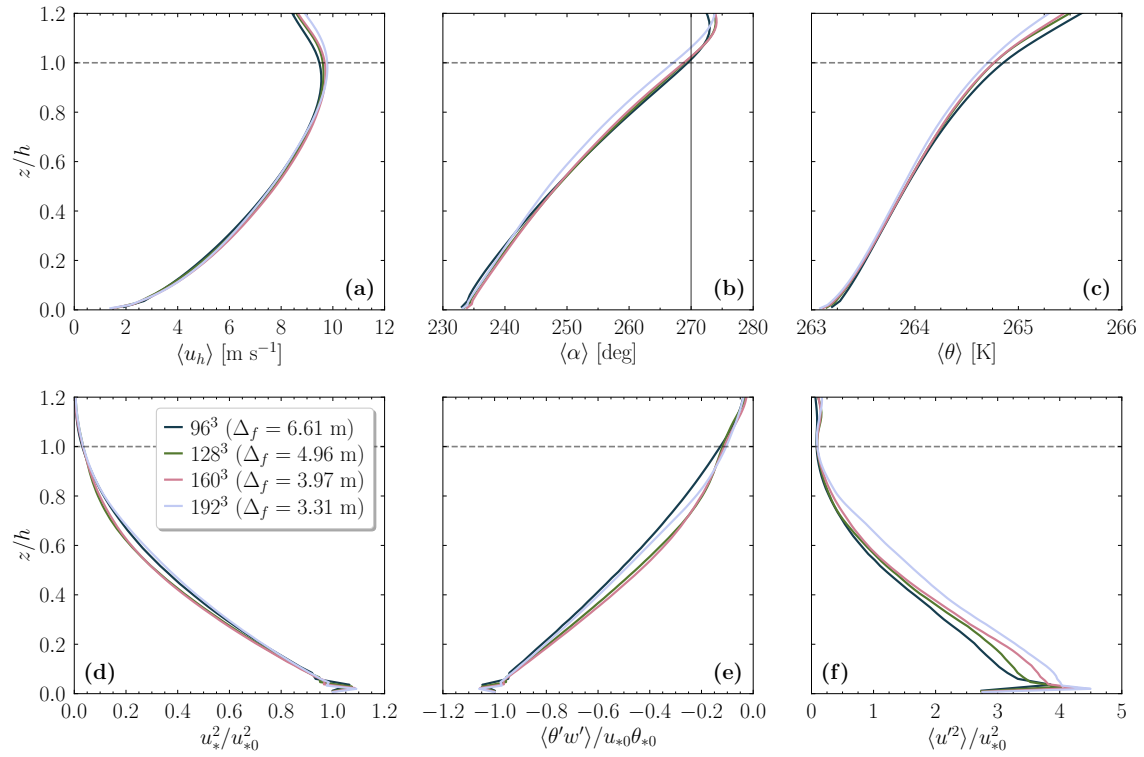
Figure A.1: Grid sensitivity for case A run at four different resolutions. Parameters are averaged in the xy plane over the last physical hour of simulation. (a) wind speed, (b) wind direction, (c) potential temperature, (d) normalized momentum flux, (e) normalized heat flux, and (f) normalized streamwise velocity variance.
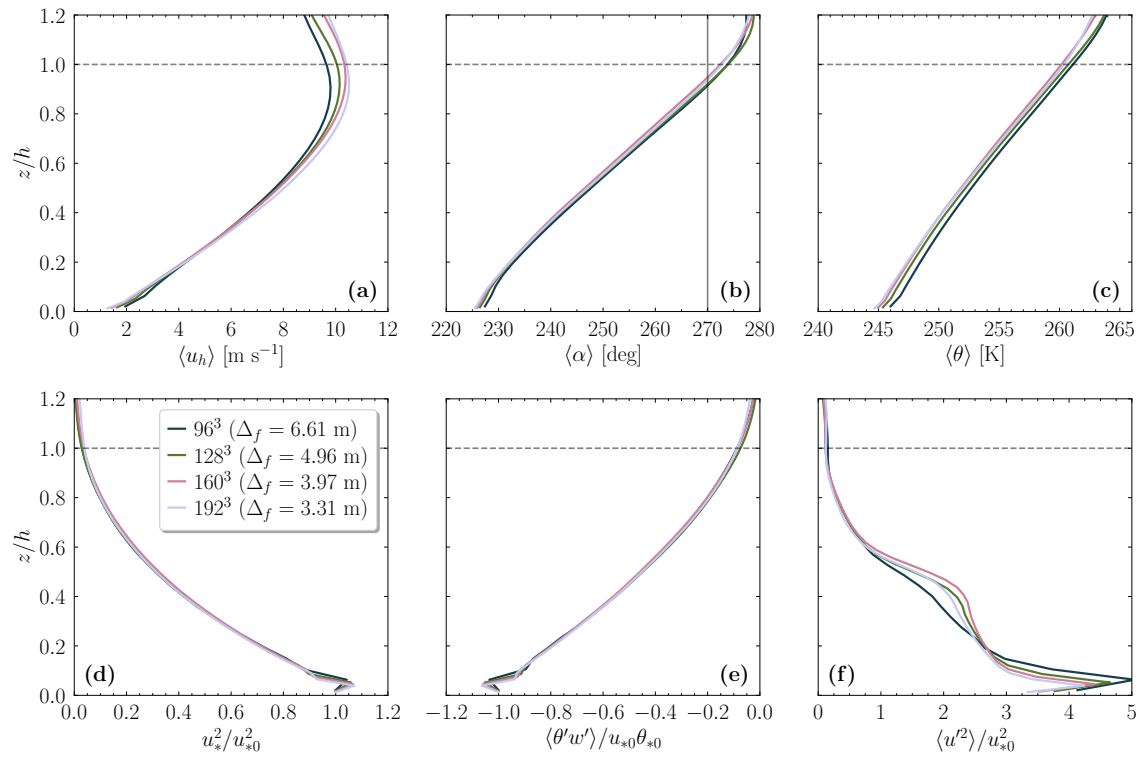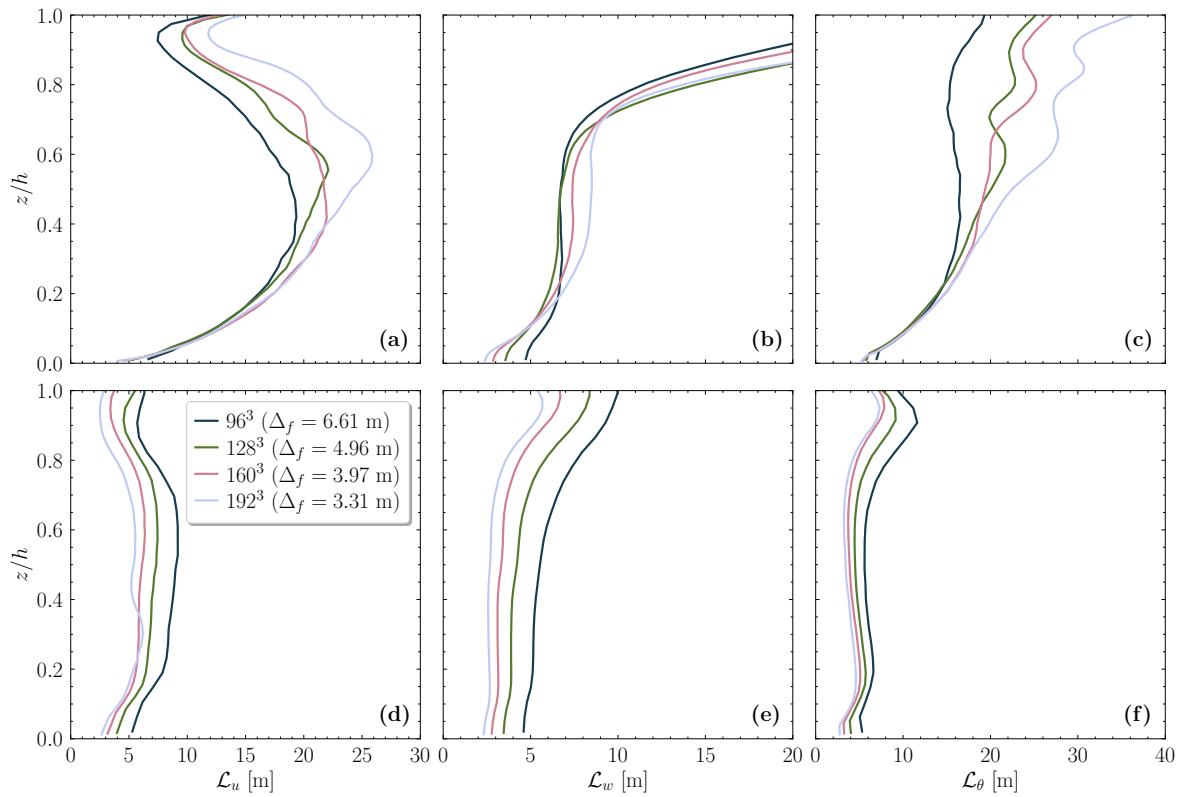
Figure A.2: Same as in Figure A.1 but for case F.

Figure A.3: Grid sensitivity for cases A (top row) and F (bottom row). Plotted are integral lengthscales of (a,d) streamwise velocity, (b,e) vertical velocity, and (c,f) potential temperature.